Spatiotemporal Dynamics of Collective Antibiotic Resistance in an Opportunistic Pathogen

by

Kelsey Hallinen

A dissertation submitted in partial fulfillment
of the requirements for the degree of
Doctor of Philosophy
(Biophysics)
in The University of Michigan
2019

Doctoral Committee:

Assistant Professor Kevin Wood, Chair
Professor Charlie Doering
Assistant Professor Qiong Yang
Professor Michal Zochowski

Kelsey Hallinen

khalline@umich.edu

ORCID iD: 0000-0003-4081-6699

To my family, who have believed in me from the beginning

Mom, thank you for showing me that I can do anything I put my mind to and for teaching me from a young age to be curious.

Dad, thank you for never letting me give up and listening to me when I needed to talk through a problem.

Nicole, you are my role model. Thank you for being my cheerleader, proof reader, and best friend.

Ross, thank you for your support and being there for all of us when we need it.

Hannah, while you probably won't be reading this for a few years, I hope you grow up and know that you can be anything you dream of, and science is a pretty cool option.

ACKNOWLEDGEMENTS

During my years at the University of Michigan, I have been incredibly lucky to have the support of many people. None of this work would have been possible without the guidance and intellectual contribution of my advisor, Kevin Wood. Kevin's mentoring constantly challenged me to think creatively and critically about the different problems facing my work and his willingness to meet and discuss my newest finding advanced my growth as a scientist. I am also grateful to Charlie Doering, Michal Zochowski, and Qiong Yang for providing insightful discussions and motivating me to connect my ideas to larger topics in the scientific community.

We cannot work alone as scientists, and I owe a huge debt to the other members of the Wood Lab. I worked with Wen Yu extensively on the sub-inhibitory biofilm project, learning from her many different methods and constantly striving for smaller error bars. Jason Karslake taught me the ins and outs of the chemostat and I couldn't have asked for a better collaborator for the planktonic work. Keanu Guardiola has helped tremendously with confocal imaging and keeping me sane as I finish up, and I'm confident his biofilm projects will continue to find interesting collective behaviors. To the other Wood Lab members, past and present, I thank you for your support, constructive criticism, and different perspectives. To Bailey, Ben, Shea, Christian, Alesha, and Tiffany: thank you for being with me every step of the way and helping me develop as a mentor. I can't wait to see what amazing things you will all accomplish.

TABLE OF CONTENTS

LIST OF FIGURES

Figure

LIST OF TABLES

ABSTRACT

Antibiotic resistance is a critical obstacle that threatens our ability to successfully treat bacterial infections. While a great deal is known about the molecular mechanisms that underlie resistance, much less is known about how these localized molecular events contribute to dynamics and evolution at the scale of the microbial community. In this work, I combine quantitative laboratory experiments on bacterial communities with mathematical modeling to investigate the effects of antibiotic exposure on populations of *E. faecalis*, an opportunistic human pathogen, across multiple length scales. In spatially-extended, surface associated communities (biofilms), I find that subinhibitory concentrations of lysis-inducing antibiotics can promote biofilm formation, a counterintuitive phenomenon driven by an interplay between inhibitory effects of antibiotics and drug-induced cell lysis, which enhances biofilm formation through the release of extracellular DNA (eDNA). As drug concentration is increased to inhibitory levels, biofilms are characterized by micron-scale spatial organization, with drug-sensitive ancestral cells surrounded by protective sub-populations of enzyme-producing resistant cells. This cooperative resistance where genetically resistant cells promote survival of neighboring drug-sensitive cells leads to rich dynamical behavior on longer length scales. Specifically, in planktonic populations of sensitive and resistant cells, we observe bistability between population survival and extinction, quasi-stable co-existence at otherwise inhibitory drug concentrations, and damped oscillations due to ecological feedback between the population and the environment. Furthermore, I show that temporally varying dosing regimens can be used to minimize population size without requiring more total drug. My results highlight the

important roles of intercellular cooperation, spatial heterogeneity, and environmental dynamics in shaping the growth and evolution of microbial communities exposed to antibiotics.

CHAPTER I

Introduction

With the rise of antibiotic resistant bacteria and the need to understand bacterial behavior, the question of collective cell behavior has risen in the scientific consciousness [1, 2, 3]. It is now better understood not only how a susceptible cell interacts with an antibiotic environment [4], but further how one cell can adapt to an antibiotic environment with different molecular mechanisms, such as a enzyme to degrade drug or a mutated drug binding site [5, 6, 7]. This molecular work is critical to our understanding of antibiotic resistance, but has yet to address community level resistance. Moving beyond a single cell to a community, there are questions of how one cell with one type of resistance mechanism interacts when in a larger population. What role does the population composition, drug concentration, or growth conditions have on the survival of a bacterial community? How can we best study these factors to further our understanding of infection population dynamics and hypothetical treatment outcomes? When thinking of collective behavior and what tools we can use to study them, examples and approaches spanning different disciplines help to guide our understanding of population level dynamics, regardless of if the population is living animals, cells, or atoms. Mathematical tools first developed for use with statistical physics, to study phenomenon like ferromagnetisim, can have parallels to describing the interactions seen in cell populations. The emergent, often counter intuitive prop-

erties present in these rich, complex systems lend themselves well to further study with bacterial communities.

From these different mechanisms, behaviors like emergent cooperation can arise in a population [8]. Cooperation is a not a new phenomenon to be observed in cellular communities [9, 10], where one subset of the population does some sort of behavior or produces a public good that will often benefit the entire population, though further understanding beyond survival of the population remains to be studied. Some examples of cooperation could be a subset of resistant cells in a mixed resistant and sensitive population that break down an antibiotic, which would benefit the whole population, or cells that commit altruistic suicide in a biofilm, releasing critical components the remaining population can use for growth. Previous research has shown communities can cooperate in both liquid, planktonic bacterial cultures [11, 12] and bacterial biofilm communities [13], though in depth studies into the community spatial and temporal dynamics and how perturbations to these communities effect the cooperative outcomes remain open questions.

With these statistical physics approaches, possible behaviors like cooperation, and open questions in mind, my research has focused on population level interactions and dynamics of bacteria across multiple length scales, focusing on spatial and temporal dynamics in bacterial communities in different growth conditions. The molecular mechanisms present (ex. Figure 1.1) are on a much smaller length scale than the population behavior, and I aim to study how the presence of a specific mechanism can drastically change the population outcome.

All experimental work in this dissertation was completed using the bacteria *Enterococcus faecalis*, a gram-positive bacteria. *E. faecalis* has been implicated in many

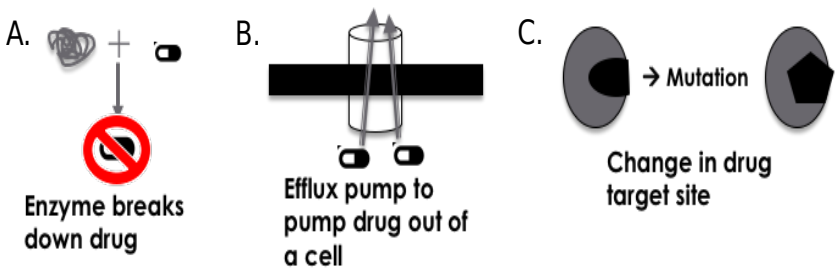

Figure 1.1: **Cartoon representation of different resistance mechanisms.** A. Enzyme deactivates the antibiotic. B. Efflux pumps in the cell walls pump antibiotic out of the cells. C. Antibiotic binding sites within the cells are mutated, decreasing drug binding.

different nosocomial infections such as bacteremia, native and prosthetic valve endocarditis, and wound infections [14]. Part of our gut microbiome [15], the species can become pathogenic and has been seen to develop antibiotic resistance [4, 5, 14, 16]. Understanding the behavior of these complex bacterial communities is the first step to understanding the different infections.

Wanting to study *E. faecalis* beyond the molecular mechanism level, planktonic cultures and biofilms were studied concurrently with mathematical models. Planktonic cultures are well stirred liquid cultures, while biofilms are dense, surface associated communities that play an important role in infectious diseases [17, 18, 19]. Biofilms show long range community behavior, such as electrical signaling [20, 21, 22], phenotypic phase variation [23], as well as multiple types of cooperative behavior, giving rise to collective resistance to antimicrobial therapies[24, 25, 26, 27]. Biofilms introduce a spatial component [28] into the population absent in planktonic cultures, leading to possible different behaviors between the two types of communities. In both, we expect the population composition to matter to overall survival, though different effects, density effects for planktonic cultures and spatial effects for biofilms, will contribute to the population dynamics and behavior. The figure below shows a confocal image of *E. faecalis*, as well as an example of a planktonic culture and a confocal fluorescent

biofilm image.

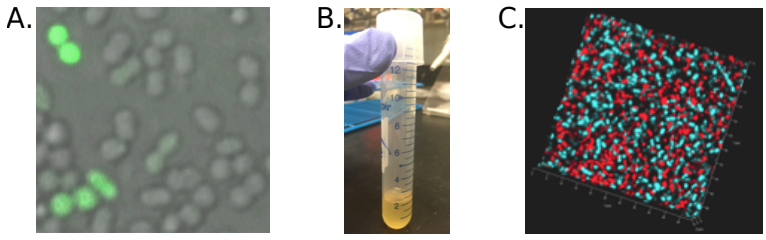

Figure 1.2: ***E.faecalis* and different types of population experiments.** A. Confocal Microscopy image of *E. faecalis* cells, some fluorescing GFP. B. Planktonic, well stirred *E. faecalis* culture. C. Confocal Microscopy image of an *E. faecalis* biofilm, where the population is labeled 50:50 with an RFP and BFP.

In what follows, we will study the cooperative, population level behavior seen in *E. faecalis* as well as the different molecular mechanisms responsible for these behaviors. Specifically, in chapter 2, we examine sensitive *E. faecalis* biofilms at low, sub-inhibitory concentrations of antibiotic, seeing a peak in biofilm mass driven by a specific class of antibiotic responsible for increasing the extracellular DNA present. Extending these studies to mixed populations of resistant and sensitive biofilms at super-inhibitory drug concentrations in chapter 3, we find the population to be cooperative and study the single cell level spatial organization that arises. Using the same mixed populations but moving to planktonic, well stirred cultures, chapter 4 studies the different cooperative, bistable outcomes arising from feedback between two distinct density effects and how the starting population composition and drug concentration can drastically alter the temporal dynamics of the population. Chapter 5 is methods based, focusing on the development of a fluorescent reporter library for *E. faecalis* that was a necessity for studying the spatial organization through confocal studies and population composition with FACS experiments.

1.1 Bibliography

[1] R. Erban and H. Othmer. From individual to collective behavior in bacterial chemotaxis. *SIAM Journal on Applied Mathematics*, 65(2):361–391, 2004.

[2] M. Wu, J. W. Roberts, S. Kim, D. L. Koch, and M. P. DeLisa. Collective bacterial dynamics revealed using a three-dimensional population-scale defocused particle tracking technique. *Applied and Environmental Microbiology*, 72(7):4987–4994, Jul 2006.

[3] Charles W. Wolgemuth. Collective swimming and the dynamics of bacterial turbulence. *Biophysical Journal*, 95(4):1564 – 1574, 2008.

[4] Richard R. Facklam, Maria da Gloria S. Carvalho, and Lucia M. Teixeira. History, taxonomy, biochemical characteristics, and antibiotic susceptibility testing of enterococci. *The Enterococci*, pages 1–54.

[5] Vivek Kak and Joseph W. Chow. Acquired antibiotic resistances in enterococci. *The Enterococci*, pages 355–383.

[6] Fred C. Tenover. Mechanisms of antimicrobial resistance in bacteria. *American Journal of Infection Control*, 34(5, Supplement):S3 – S10, 2006.

[7] Franklin H. Epstein, George A. Jacoby, and Gordon L. Archer. New mechanisms of bacterial resistance to antimicrobial agents. *New England Journal of Medicine*, 324(9):601–612, Feb 1991.

[8] R Axelrod and W. Hamilton. The evolution of cooperation. *Science*, 211(4489):1390–1396, Mar 1981.

[9] Paul B. Rainey and Katrina Rainey. Evolution of cooperation and conflict in experimental bacterial populations. *Nature*, 425(6953):72–74, Sep 2003.

[10] Regis Ferriere and Richard E. Michod. The evolution of cooperation in spatially heterogeneous populations. *The American Naturalist*, 147(5):692–717, May 1996.

[11] Eugene A Yurtsev, Hui Xiao Chao, Manoshi S Datta, Tatiana Artemova, and Jeff Gore. Bacterial cheating drives the population dynamics of cooperative antibiotic resistance plasmids. *Molecular Systems Biology*, 2013.

[12] Robin A. Sorg, Leo Lin, G. Sander van Doorn, Moritz Sorg, Joshua Olson, Victor Nizet, and Jan-Willem Veening. Collective resistance in microbial communities by intracellular antibiotic deactivation. *PLOS Biology*, 14(12):e2000631, Dec 2016.

[13] Isabel Frost, William P.J Smith, Sara Mitri, Alvaro San Millan, Yohan Davit, James M. Osborne, Joe M. Pitt-Francis, R. Craig MacLean, and Kevin R Foster. Cooperation, competition and antibiotic resistance in bacterial colonies. *ISME*, 12:1582–1593, 2018.

[14] Preeti . Malani, Carol A. Kauffman, and Marcus J. Zervos. Enterococcal disease, epidemiology, and treatment. *The Enterococci*, pages 385–408.

[15] Gerald W. Tannock and Greg Cook. Enterococci as members of the intestinal microflora of humans. *The Enterococci*, pages 101–132.

[16] Rob J.L. Willems, William P. Hanage, Debra E. Bessen, and Edward J. Feil. Population biology of gram-positive pathogens: high-risk clones for dissemination of antibiotic resistance. *FEMS Microbiology Reviews*, 35(5):872–900, Sep 2011.

[17] Rodney M Donlan. Biofilms and device-associated infections. *Emerging infectious diseases*, 7(2):277, 2001.

[18] Rodney M Donlan. Biofilms: microbial life on surfaces. *Emerg Infect Dis*, 8(9), 2002.

[19] Luanne Hall-Stoodley, J. William Costerton, and Paul Stoodley. Bacterial biofilms: from the natural environment to infectious diseases. *Nature Reviews Microbiology*, 2(2):95–108, Feb 2004.

[20] Arthur Prindle, Jintao Liu, Munehiro Asally, San Ly, Jordi Garcia-Ojalvo, and Gürol M Süel. Ion channels enable electrical communication within bacterial communities. *Nature*, 527(7576):59, 2015.

[21] Jintao Liu, Rosa Martinez-Corral, Arthur Prindle, D Lee Dong-yeon, Joseph Larkin, Marçal Gabalda-Sagarra, Jordi Garcia-Ojalvo, and Gürol M Süel. Coupling between distant biofilms and emergence of nutrient time-sharing. *Science*, 356(6338):638–642, 2017.

[22] Jacqueline Humphries, Liyang Xiong, Jintao Liu, Arthur Prindle, Fang Yuan, Heidi A Arjes, Lev Tsimring, and Gürol M Süel. Species-independent attraction to biofilms through electrical signaling. *Cell*, 168(1):200–209, 2017.

[23] Nicholas Chia, Carl R Woese, and Nigel Goldenfeld. A collective mechanism for phase variation in biofilms. *Proceedings of the National Academy of Sciences*, 105(38):14597–14602, 2008.

[24] Nicole M Vega and Jeff Gore. Collective antibiotic resistance: mechanisms and implications. *Current opinion in microbiology*, 21:28–34, 2014.

[25] Hannah R Meredith, Jaydeep K Srimani, Anna J Lee, Allison J Lopatkin, and Lingchong You. Collective antibiotic tolerance: Mechanisms, dynamics, and intervention. *Nature chemical biology*, 11(3):182, 2015.

[26] Thien-Fah C Mah and George A O'Toole. Mechanisms of biofilm resistance to antimicrobial agents. *Trends in microbiology*, 9(1):34–39, 2001.

[27] Philip S Stewart and J William Costerton. Antibiotic resistance of bacteria in biofilms. *The Lancet*, 358(9276):135–138, Jul 2001.

[28] Philip S Stewart and Michael J Franklin. Physiological heterogeneity in biofilms. *Nature reviews. Microbiology*, 6(3):199, 2008.

CHAPTER II

Interplay Between Antibiotic Efficacy and Drug-Induced Lysis Underlies Enhanced Biofilm Formation at Subinhibitory Drug Concentrations

This chapter was amended from: Wen Yu, Kelsey M. Hallinen, and Kevin B. Wood. 'Interplay between antibiotic efficacy and drug-induced lysis underlies enhanced biofilm formation at subinhibitory drug concentrations.' Antimicrobial Agents and Chemotherapy, 62(1),Oct 2017

2.1 Introduction

Biofilms- surface associated, spatially fixed bacterial communities- are complex, medically relevant, and prone to collective behavior [1]. Biofilms of a single Wild-Type (WT) strain can provide interesting insights and understanding the molecular mechanisms still leaves open questions to the collective biofilm behaviors. The biofilm response to antibiotics has been a topic of particular interest, with biofilms across species showing dramatically increased resistance to antibiotics relative to planktonic cells. On the other hand, a number of studies have shown–somewhat counterintuitively–that exposure to sub-lethal doses of antibiotics may *enhance* biofilm formation in a wide range of species [2, 3, 4]. While antibiotic-mediated biofilm induction has been associated with modulated expression of biofilm-related genes,

particularly those affiliated with bacterial and cell surface adhesion, cell motility, or metabolic stress, the mechanisms vary across species and drug classes and remain a focus of ongoing research efforts [3, 4].

In this work, we investigate the effects of sublethal antibiotic concentrations on biofilm formation in *E. faecalis*. While our understanding of the molecular basis of both biofilm development and drug resistance in *E. faecalis* continues to rapidly mature [5, 6], surprisingly little attention has been paid to the impact of subinhibitory antibiotic treatments on *E. faecalis* communities. However, a recent series of intriguing studies has shown that *E. faecalis* biofilm formation (without antibiotic) hinges on an interplay between fratricide-associated cell lysis and the release of extracellular DNA (eDNA) [7, 8, 9, 10, 11]. More generally, eDNA is widely recognized as a critical component of biofilm structure in many species [12, 13, 14]. Additionally, a recent study in *S. aureus* showed that β-lactams administered at subinhibitory concentrations promoted biofilm formation and induced eDNA release in an autolysin-dependent manner [15]. Taken together, these results suggest that, for some drugs, biofilm induction hinges on a balance between the inhibitory effects of antibiotics–which reduce biofilm formation at sufficiently high concentrations–and the potential of antibiotic-induced cell lysis to promote biofilm formation, presumably through release of eDNA. Here we investigate this trade-off in *E. faecalis* biofilms exposed to multiple classes of antibiotics. We find that subinhibitory concentrations of cell wall synthesis inhibitors, but not other classes of drug, promote biofilm formation associated with increased cell lysis and increased eDNA and eRNA. Using a simple mathematical model, we quantify the trade-offs between drug efficacy and "beneficial" cell lysis and use the model to predict the effect of environmental perturbations, including the addition of DNase or chemical inhibitors of lysis, on the location and height of optimal biofilm production. Our results suggest that inhibitors of cell wall synthesis

promote biofilm formation via increased cell lysis and offer a quantitative, predictive framework for understanding the trade-offs between drug toxicity and lysis-induced biofilm induction.

2.2 Results

2.2.1 Sub-MICs of Cell Wall Synthesis Inhibitors lead to a peak in Biofilm Formation

To investigate antibiotic induced biofilm formation, we exposed cultures of *E. faecalis* V583, a fully sequenced clinical isolate, to ampicillin during the first 24 hours of biofilm development. Using a bulk crystal violet staining assay (Methods), we observed a statistically significant enhancement of biofilm formation after 24 hours in the presence of low concentrations of ampicillin (Figure 2.1A). Ampicillin at these concentrations has almost no effect on growth of planktonic cultures, leading only to a slight decrease in the steady state cell density (Figure S1A). Similar enhancement of biofilm formation was observed for cells grown in different types of media (BHI, TSB) as well as for strain OG1RF, a common laboratory strain (Figure 2.1B), with the magnitude of the enhancement ranging from $\approx 10 - 30\%$.

To determine whether the biofilm enhancement was specific to ampicillin, we performed similar experiments for antibiotics from multiple drug classes. Interestingly, we observed a similar increase of biofilm mass for other drugs inhibiting cell wall synthesis, including ceftriaxone, oxacillin, and fosfomycin (Figure 2.1C-E), whose mechanism of action is tightly linked to cell lysis. By contrast, drugs targeting protein synthesis, DNA synthesis, RNA synthesis, and folic acid synthesis did not appear to promote biofilm formation over the range of subinhibitory concentrations tested (Figure 2.2).

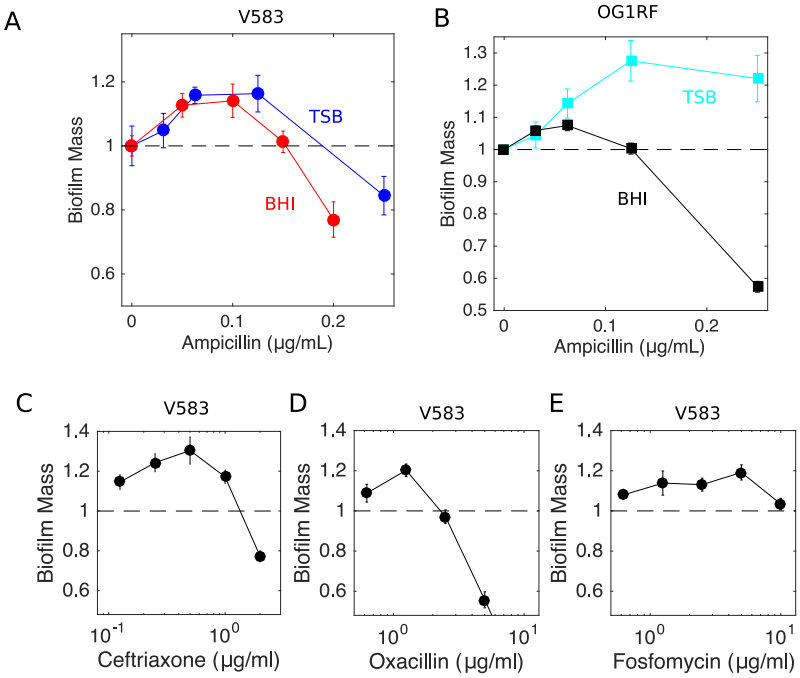

Figure 2.1: **Inhibitors of cell wall synthesis enhance biofilm formation at low concentrations.** A. Biofilm mass (normalized to 1 in the absence of drug) as a function of ampicillin concentration for E. faecalis strain V583 in TSB (blue) and BHI (red). B. Similar to panel A, with E. faecalis strain OG1RF in TSB (light blue) and BHI (black). Similar curves are also shown for V583 in BHI exposed to three additional cell wall synthesis inhibitors: ceftriaxone (C), oxacillin (D), and fosftomycin (E). In all panels, biofilm mass is measured by crystal violet assay (see Methods). Error bars are ± standard error of the mean from 6-12 replicates.

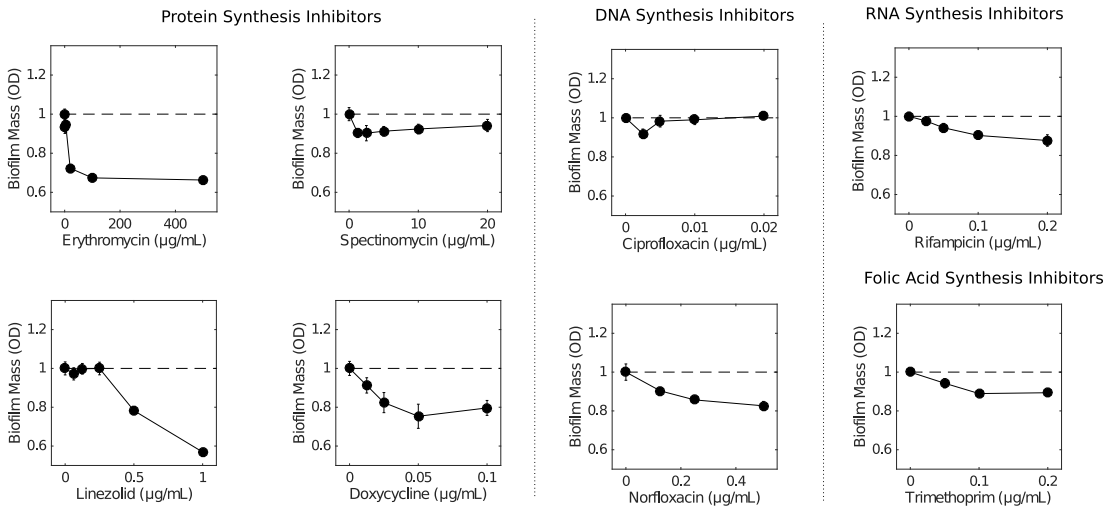

Figure 2.2: **Antibiotics that do not target the cell wall do not enhance biofilm formation at low concentrations.** Biofilm mass (normalized to 1 in the absence of drug) as a function of antibiotic for *E. faecalis* strain V583 in BHI exposed to protein synthesis inhibitors (erythromycin, spectinomcyin, linezolid, doxycycline), DNA synthesis inhibitors (ciprofloxacin, norfloxacin), RNA synthesis inhibitor (rifampicin), and folic acid synthesis inhibitors (trimethoprim). In all panels, biofilm mass is measured by crystal violet assay (see Methods). Error bars are ± standard error of the mean from 6-12 replicates.

2.2.2 Biofilm enhancement associated with increased cell lysis and extracellular DNA

In ampicillin, peak biofilm formation occurs for concentrations of approximately 0.1 μg/mL, which has little effect on growth of planktonic cell cultures (Figure S1). To determine the effect of ampicillin on planktonic cultures over a wider drug range, we measured optical density time series of V583 cultures exposed to ampicillin concentrations up to 1 μg/mL (Figure 2.3A). Ampicillin has little effect ($< 15\%$) on the steady state density of cells up to concentrations of approximately 0.2 μg/mL, and the dose response curve is well-approximated by a Hill-like function (commonly used in pharmacology [16]) with a half-maximal inhibitory concentration of $K_{50} = 0.38 \pm 0.01$ μg/mL. Therefore, increased biofilm formation occurs at concentrations considerably smaller than the half-maximal inhibitory concentration measured for planktonic cultures.

While these drug concentrations do not appreciably impact planktonic cell growth, it's possible that they still produce a measurable increase in cell lysis. To investigate this issue, we measured cell lysis in 24 hour biofilms (Figure 2.3B) and planktonic cultures (Figure S1) using an ATP-based luminescence assay [17]. Indeed, we observed increased cell lysis even for low doses of ampicillin ($\leq 0.2\mu$g/mL), with lysis increasing by nearly 5 fold in biofilms and several thousand fold in planktonic cultures for the highest doses.

Because eDNA has been implicated in *E. faecalis* biofilm formation, we next asked whether subinhibitory doses of ampicillin lead to increased quantities of extracellular nucleic acids in biofilms. To answer this question, we grew 24-hour biofilms in 5 mL cultures at various concentrations of ampicillin, harvested the biofilms and removed cells by centrifugation, and then extracted nucleic acid from remaining supernatant. We then quantified DNA (RNA) following treatment with RNase (DNase) using quantitative imaging of agarose gel electrophoresis (Figure 3C). Both eDNA and eRNA increase with ampicillin treatment, with eDNA (but not eRNA) increasing even at the lowest dose (ampicillin at 0.1 μg/mL).

2.2.3 Non-antibiotic induction of cell lysis promotes biofilm formation

Because cell lysis is observed at subinhibitory doses of ampicillin, and because lysis has been previously implicated in *E. faecalis* biofilm formation [7, 8, 9, 10, 11], we next asked whether non-antibiotic inducers of cell lysis might also increase biofilm mass at small concentrations. To test this hypothesis, we grew biofilms in the presence of Triton X-100, a surfactant and known inducer of cell lysis [18]. Interestingly, we observed enhancement of biofilm formation similar in magnitude ($\approx 20\%$) to that observed for cell wall inhibitors over Triton X-100 concentrations that yield similar

(approximately 1.5-2 fold) increase of cell lysis (Figure 2.3D).

2.2.4 Antibiotic-induced biofilm formation corresponds to an increase in the density of living cells and mean cell area

While our results indicate that biofilm mass is increased at low doses of ampicillin, it is not clear whether this enhancement is due to an increase in the number of living cells or merely an increase in bulk biofilm mass, which may include both viable and non-living components. To answer this question, we grew 16 replicate biofilms at 3 different antibiotic concentrations, treated them with live-dead cell stains, and quantified the number of live and dead cells in two-dimensional sections (i.e. the spatial cell density) at single-cell resolution using laser-scanning confocal microscopy (Methods). We observed an increase of approximately 25% in the number of living cells per slice, an increase similar in magnitude to the effects observed in bulk experiments (Figure 4). Interestingly, we also observed a slight increase in the mean size of a living cell as drug concentration increased. These results indicate that sections of biofilms formed under subinhibitory concentrations contain more living cells and more total living cell area–not merely an increase in non-living mass–than those formed in the absence of drug.

2.2.5 Mathematical model describes biofilm induction as a balance between beneficial cell lysis and costly drug efficacy

To quantify the trade-offs between antibiotic efficacy and "beneficial" cell lysis, we developed a simple mathematical model describing the mass of living cells (N) and the mass of lysed cells and dead cell material (D), including eDNA, in a biofilm. Specifically, we have

$$\begin{aligned} \frac{\partial N}{\partial t} &= g\left(1-\frac{N}{K}\right)N - rN + cLD \\ \frac{\partial D}{\partial t} &= rN - \gamma D \end{aligned} \tag{2.1}$$

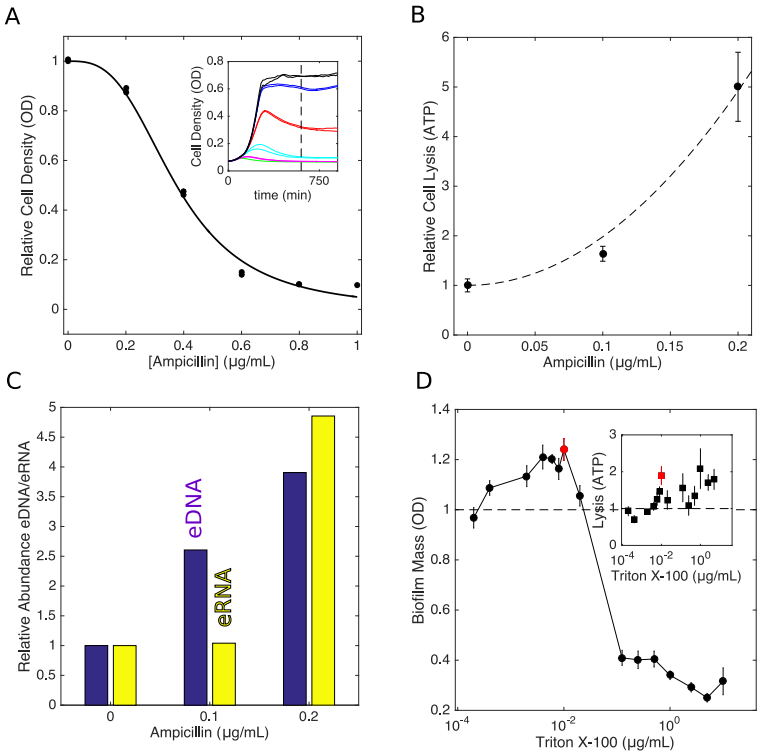

Figure 2.3: **Enhanced biofilm formation occurs at sub-inhibitory concentrations and is associated with increased cell lysis and increased extracellular nucleic acid.** A. Relative cell density (OD) approximately 10 hours after addition of ampicillin. Solid curve, fit to $(1-(A/K_{50})^h)^{-1}$, with A the ampicillin concentration, $K_{50} = 0.38 \pm 0.01$ μg/mL the half maximal inhibitory concentration of the drug, and $h = 3$ a coefficient that describes the steepness of the dose response curve. Inset: time series of optical density following drug exposure at time $t = 0$ for ampicillin concentrations of 0 (black), 0.2 μg/mL (blue), 0.4 μg/mL (red), 0.6 μg/mL (green), 0.8 μg/mL (magenta), and 1.0 μg/mL (cyan). B. Cell lysis (relative to untreated cells) as a function of ampicillin as measured by ATP luminescence assay (see Methods). Error bars are $\pm$ standard error of the mean from eight replicates. Dashed line, fit to $1 + a^2/r_{00}$, with a the ampicillin concentration (measured in units of the drug's half maximal inhibitory concentration (K_{50})) and $r_{00} = 0.010 \pm 0.001$. C. Abundance of extracellular DNA (eDNA, blue) or RNA (eRNA, yellow) as a function of ampicillin concentration. Abundance is normalized relative to the eDNA (or eRNA) measured in the absence of drug. See also Figure S1. D. Triton X-100, a known inducer of cell lysis, enhances biofilm formation at low concentrations. Biofilm mass is measured by crystal violet assay (see Methods), and error bars are $\pm$ standard error of the mean from eight replicates. Inset: cell lysis (relative to untreated cells) as a function of Triton X-100 concentration. Red points correspond to peak in biofilm formation.

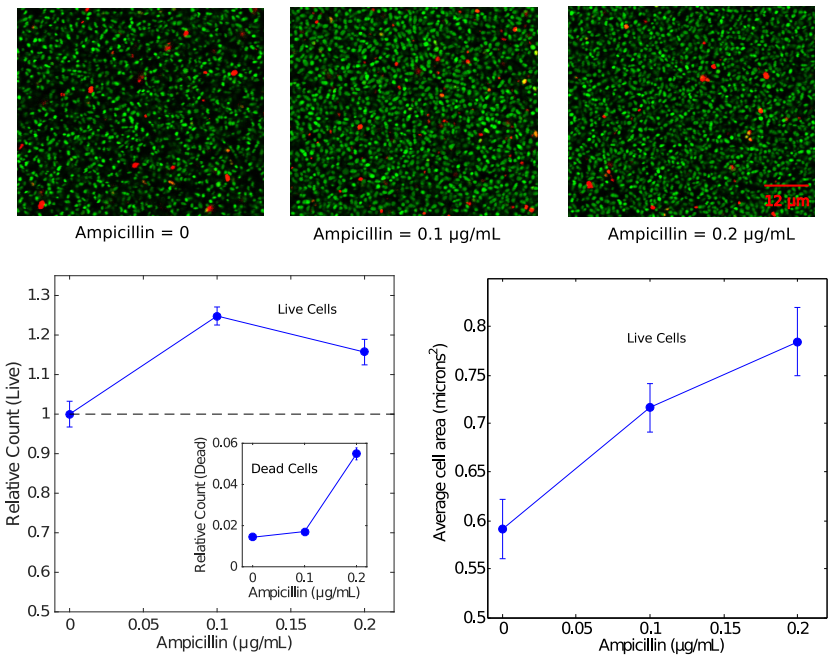

Figure 2.4: **Enhanced biofilm formation corresponds to an increase in the density of living cells.** Top panels: example sections from laser scanning confocal images of biofilms exposed to ampicillin at different concentrations (0, left panel; 0.1 μg/mL, middle panel; 0.2 μg/mL, right panel) and post-treated with live (green) and dead (red) stains. Lower left panel: Relative count of live cells and dead cells (inset) as a function of ampicillin concentration. Counts are normalized relative to the average number of live cells per 160 μm x 160 μm slice in the absence of drug, which is set to 1; note that each slice contains on the order of $10^3 - 10^4$ live cells. Lower right panel: Mean area of living cells. Error bars are $\pm$ standard error of the mean taken over a total of 48 two dimensional slices per condition (three z-slices–taken at identical heights–for each biofilm and 16 independent biofilms per condition). The analysis involves on the order of 10^5 total live cells per condition.

In the first equation, the first term describes logistic growth (with per capita growth g and carrying capacity $K > 0$), the second describes cell death (lysis) with rate $r \geq 0$, and the last term describes the increase in biofilm mass due to surface attachment / adhesion of living cells in the planktonic phase (L), a process which is coupled to the dead cell mass D and controlled by a parameter $c > 0$. Models without this coupling do not exhibit a drug-induced maximum in biofilm mass (see SI). While the molecular mechanism of coupling is not specified in the model, this term could describe eDNA-mediated attachment and adhesion of planktonic cells, which is here assumed to occur at a rate proportional to both the living cells in solution (L) and the lysed cell material in the biofilm (D). In the second equation, the first term accounts for cell lysis and the second term describes a decay of lysed cell material (e.g. eDNA) due to, for example, detachment from the biofilm. The model implicitly assumes that the effect of antibiotic on cells in the planktonic phase occurs on a fast timescale, allowing L to reach a steady state on the timescale of biofilm formation. This assumption is consistent with experimental measurements, where planktonic populations reach a steady state size after approximately 10 hours (Figure 3), while biofilms are formed over a longer 24 hour timescale. The model includes two parameters, $r = r(a)$ and $L = L(a)$, that depend on drug concentration, a.

In the steady state, the living biofilm mass N is given by

$$\frac{N}{K} \equiv n^* = 1 + r_0(a)\left(L_0(a) - 1\right), \tag{2.2}$$

where $r_0(a) = r(a)/g$ and $L_0(a) = cL(a)/\gamma$ are (rescaled) functions describing the rate of cell lysis and the number of living cells in planktonic solution as a function of drug, a. Equation 2.2 illustrates a simple balance between the biofilm-inducing and biofilm-inhibiting effects antibiotics. To understand this tradeoff, we derived a phase diagram

(Figure 5B) showing regions of enhanced biofilm formation–specifically, regions of the $(r(a), L(a))$ plane where n^* is greater in the presence of drug than in its absence (see SI for details). Enhanced biofilm formation is favored in regions of high lysis $r(a)$ and large planktonic populations $L(a)$. However, lysis $r(a)$ is expected to increase with drug, while the number of available cells in planktonic phase $L(a)$ is expected to decrease with a and eventually tend towards zero. The trade-off between these two effects determines the path taken by the system through the $(r(a), L(a))$ plane as drug is added. If increasing drug leads to increased lysis without a dramatic impact on the planktonic cells, the system exhibits enhanced biofilm formation (Figure 5B, path A). On the other hand, if increasing drug leads to a large decrease in planktonic cells and a relatively small increase in lysis, biofilm formation will not be enhanced (Figure 5B, path B).

In principle, the functional forms for $r_0(a)$ and $L_0(a)$ could be derived from microscopic models that describe the molecular level dynamics of antibiotic-induced cell lysis and cell death. Fortunately, however, the functions $r_0(a)$ and $L_0(a)$ can also each be estimated–up to a scaling constant–by independent experimental measurements, even in the absence of a detailed molecular model. Specifically, using the data in Figure 2.3A-B, we take

$$\begin{aligned} L_0(a) &= \frac{\epsilon}{1 + a^h} \\ r_0(a) &= r_{01}\left(r_{00} + a^2\right) \end{aligned} \tag{2.3}$$

where $h = 3$ describes the steepness of the dose response curve (and is analogous to Hill coefficients used in biochemistry to describe cooperative binding between ligands), a is measured in units of the drug's half-maximal inhibitory concentration, estimated to be $K_{50} = 0.38 \pm 0.01$ μg/mL, and $r_{00} = 0.010 \pm 0.001$. It should be noted that we assume a quadratic dependence of lysis on a to match the experimental measurements; this should be viewed as a simple parameterization of the experimental lysis measurements and does not imply any particular mechanism. The quadratic

dependence of lysis on a could depend on complex pharmacological and pharmacodynamics of the antibiotics, and we do not attempt to model those here.

The remaining two parameters, ϵ and r_{01}, are scaling parameters that can be estimated from biofilm induction curves (e.g. Figure 1). Because the measured value of $r_{00} << 1$, we can derive approximate solutions for the location (a_{max}) and height (p_h) of the biofilm peak using simple perturbation theory (SI). Specifically, the peak location is given by

$$a_{max} \approx \left(\frac{2(\epsilon - 1)}{4 + \epsilon}\right)^{1/3} \tag{2.4}$$

and the peak height is given by

$$p_h \approx 1 + \frac{3}{5}\left(\frac{2}{5}\right)^{2/3} r_{01}(\epsilon - 1)^{5/3}. \tag{2.5}$$

These expressions indicate that an optimum in biofilm production occurs at a nonzero concentration a when $\epsilon > 1$, and the effect of further increasing ϵ is to shift the peak to higher a and increase its height. We refer to ϵ as an effective coupling parameter, and given the functional forms in Equation 2.3, the value of ϵ alone determines whether there is a peak in biofilm formation at nonzero drug concentrations. In terms of the original model parameters, ϵ is given by $\epsilon = \frac{cL(0)}{\gamma}$, where $L(0)$ is the size of the planktonic cell population at zero drug concentration, and r_{01} is given by $r_{01} \equiv \frac{r(0)}{gr_{00}}$, where $r(0)$ is the native level of lysis in the absence of drug. Antibiotic-mediated biofilm formation occurs for $\epsilon > 1$ and is therefore favored by large rates of lysis-mediated adhesion (c), high concentrations of planktonic cells ($L(0)$), and slow degradation / decay of eDNA (γ).

2.2.6 Model predicts effects of DNase treatment, a second antibiotic, and lysis inhibitors

While it is straightforward to estimate ϵ and r_{01} from biofilm experiments–for example, $\epsilon = 1.09 \pm 0.02$ and $r_{01} = 18 \pm 6$ based on the bulk experiments in Figure 2.1A–it is more instructive to consider the qualitative predictions of the model as parameters are varied. Our model predicts that perturbations that decrease ϵ will lower the peak height (Figure 2.5B, left panel; Figure S2, bottom left). On the other hand, perturbations that decrease cell lysis would shift $r_0(a) \to r_0(a) - \beta$, with β a positive constant (or equivalently, decreasing lysis would shift $r_{00} \to r_{00} - \beta/r_{01}$). While the latter effects would not be evident at the level of the approximate equations (Equations 2.4, 2.5), we can evaluate the predicted effects numerically (Figure 2.5C, left panel, and Figure S2, bottom right panel) or by looking at higher-order terms in the approximation (SI). Decreasing lysis is predicted to shift the peak location to higher drug concentrations and, somewhat counterintuitively, leads to an increase in biofilm induction (that is, an increase in the height of the peak relative to the drug-free case). In words, a higher concentration of antibiotic is needed to achieve sufficient cell lysis to induce increased biofilm production.

To test these predictions experimentally, we first repeated both bulk and microscopy experiments in the presence of DNase I. Because eDNA has been implicated as the molecular conduit linking cell lysis to biofilm formation, we expect DNase treatment to decrease ϵ by effectively increasing the decay rate γ. Indeed, biofilms treated with DNase exhibit lower peaks (Figure 2.5D). The model also predicts a slight shift in the location of the peak, but the resolution of the experimental data is insufficient to evaluate that prediction quantitatively. A second way of decreasing ϵ would be to decrease the number of living cells in planktonic phase (α). One possibility is to treat the cells with a second (non-lysis-inducing) antibiotic, which is expected to lower

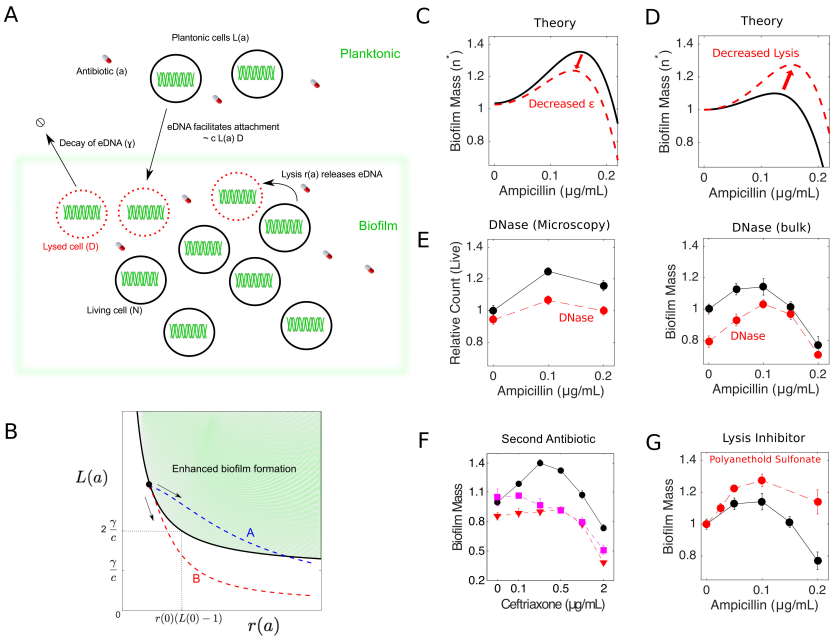

Figure 2.5: **Mathematical model predicts effects of DNase, non lysis-inducing drugs, and cell lysis inhibitors.** A. A simple math model couples cell lysis to biofilm formation, describes qualitative features of antibiotic mediated biofilm enhancement. Lysis of living biofilm cells (N) depends on drug concentration a according to $r(a)$. Lysed cells (D) facilitate attachment of planktonic cells ($L(a)$). Adhesion/attachment is presumably enhanced due to release of eDNA, which itself detaches/decays at a rate γ, and surface attachment is proportional to $L(a)$ and D with a rate constant c. The model contains two free "effective" parameters ($\epsilon \equiv \frac{cL(0)}{\gamma}$ and $r_{01} \equiv \frac{r(0)}{gr_{00}}$), estimated from the peak height and location in biofilm enhancement curves (e.g. Figure 2.1 or Figure 2.4). Intuitively, ϵ describes the effective coupling between cell lysis and biofilm induction; a peak in biofilm mass occurs at nonzero drug concentration when $\epsilon > 1$. B. Phase diagram shows the region of parameter space where enhanced biofilm formation occurs in terms of model parameters. Enhanced biofilm formation is favored in regions of high lysis ($r(a)$) and large planktonic populations ($L(a)$). Blue (red) dashed lines: path taken by system as antibiotic concentration increased; arrows indicate direction of increasing a. The blue curve (path A) exhibits enhanced biofilm formation, while the red curve (path B) does not. C. Model predictions (dashed curve): decreasing ϵ coupling by several percent (left panel) leads to decrease in height and location of the peak in living biofilm mass ($n^* \equiv N/K$, solid line). Parameter values $\epsilon = 1.18 \pm 0.01$ and $r_{01} = 19 \pm 4$ in the absence of perturbation are estimated from confocal microscopy living biofilm cell counts (Figure 2.4). D. Model predictions (dashed curve): decreasing cell lysis leads to increase in height and location of maximum living biofilm mass (n^*, solid line). Parameter values $\epsilon = 1.09 \pm 0.02$ and $r_{01} = 18 \pm 6$ estimated from bulk experiments (Figure 2.1).E. Relative biofilm mass (solid curves) as a function of ampicillin from confocal microscopy (left; see also Figure 2.4) and bulk experiments (right; see also Figure 2.1). Dashed curves: identical experiments but with DNase I added at a concentration of 0.4 mg/mL. F. Relative biofilm mass as a function of ceftriaxone alone (solid curve, circles) or ceftriaxone in combination with a constant concentration of rifampicin at 0.3 μg/mL (squares, dashed) or tetracycline at 0.2 μg/mL (triangles, dashed). G. Solid curve: same as in panel E. Dashed curves: identical experiments but with sodium polyanethole sulfonate (SPS), a known lysis inhibitor, at a concentration of 10 μg/mL. Error bars represent $\pm$ standard error of the mean.

the steady state density of cells in liquid phase. Consistent with this prediction, we observed that treatments with a cell wall synthesis inhibitor (ceftriaxone) along with a second, non-lysis inducing drug (tetracycline or rifampicin) decrease the height of the peak to almost zero (Figure 5E).

Next, to test the prediction that decreasing lysis leads to an increase in relative peak height and location, we repeated the biofilm experiment in the presence of sodium polyanethole sulfonate (SPS). SPS is a common anticoagulant used in clinical blood cultures and is known to have a positive effect on bacterial survival [19]. It has been shown to inhibit of cell lysis in staphylococci by suppressing activity of autolytic wall systems [20, 21, 15]. To verify that SPS inhibits cells lysis in our system, we measured lysis as a function of SPS concentration using an ATP-based luminescence assay [17].; our data suggests that SPS inhibits cell lysis by approximately 40% in the absence of drug at the concentrations used (Figure S3). We found that treatment with the lysis inhibitor appears to shift the peak to slightly higher drug concentrations and increases the magnitude of biofilm enhancement, again consistent with predictions from the model.

2.3 Discussion

Our work demonstrates that biofilm formation in *E. faecalis* is enhanced by subinhibitory concentrations of cell-wall synthesis inhibitors, but not by inhibitors of protein, DNA, folic acid, or RNA synthesis. Enhanced biofilm formation is associated with increased cell lysis and an increase in eDNA and eRNA. We observed similar enhancement effects when cultures were treated with non-antibiotic chemicals that induce similar amounts of cell lysis. To quantify the trade-off between drug toxicity and the beneficial effects of cell lysis, we developed a simple mathematical model that predicts changes to drug-induced biofilm formation due to external perturba-

tions that reduce eDNA, reduce living cells in the planktonic phase, or inhibit cell lysis. Our model suggests that antibiotic-induced biofilm formation occurs when the drug-induced increase in cell lysis is sufficiently large relative to the drug-induced decrease of living cells in the planktonic phase.

Subinhibitory concentrations of antibiotics have been reported to promote biofilm formation in multiple species via a range of different mechanisms [3, 4]. However, relatively little is known about drug-induced biofilm formation in *E. faecalis*. Subinhibitory antibiotic concentrations have previously been shown to impact the physio-electrical [22] and adhesion behavior [23] of *E. faecalis*. In addition, low concentrations of tigecycline have been shown to reduce biofilm formation, even when growth of planktonic cells is not significantly affected [24]. To our knowledge, however, this is the first work to describe enhancement of biofilm formation due to cell wall synthesis inhibitors in *E. faecalis*. On the other hand, our work suggests that inhibitors of protein, DNA, folic acid, and RNA synthesis do not promote biofilm formation over a wide range of subinhibitory concentrations (though we do caution that we cannot definitively rule out biofilm promotion at higher concentrations, perhaps via different mechanisms).

Our results are consistent with the established role of eDNA in biofilm formation and may be applicable to drug-induced biofilm formation in other species, most notably *S. aureus* [15]. However, it is possible that other mechanisms may also contribute–at least in part–to our results. For example, recent work has shown that eDNA is prevalent in biofilms even at the early developmental stages when cell lysis is minimal [17], and it is possible that subinhibitory drug concentrations increase eDNA through similar non-lysis mechanisms. In addition, it is well-known that sub-MIC levels of antibiotic can dramatically alter gene expression profiles in bacteria [25, 26, 27], indi-

cating that biofilm enhancement may arise from a complex combination of multiple factors. Finally, we note that live-dead cell staining results should be interpreted with some caution, because uptake of various stains may be variable [28, 29, 30, 31, 32, 33]. Nevertheless, our results are promising because they suggest that, at least in the experimental regimes measured here, a simple conceptual (and mathematical) model is sufficient to describe and predict the primary effects of drug exposure.

Despite the model's success, it is without question a dramatic oversimplification of the complex biofilm formation process. Computational models of biofilm formation are a powerful tool for understanding dynamics and evolution of complex communities [34, 35, 36], and detailed models may contain dozens or even hundreds of microscopic parameters. Yet even the most elaborate mathematical models neglect biological details at some scale. Our approach was not to develop a detailed microscopic model, but rather to develop a simple, minimal model to help intuitively explain and predict the trade-offs between antibiotic efficacy and beneficial cell lysis at the population level. Linking our model with more detailed agent-based simulations may help us further understand the potential role of spatial structure and heterogeneity in drug-induced biofilm formation. For example, recent work has shown that in the absence of drug, *E. faecalis* biofilm formation depends on a phenotypic bistability in gene expression, giving rise to lysis-susceptible and lysis-inducing subpopulations [7, 8, 9, 10, 11]. It would be interesting to further explore the interplay between this multi-modal population structure and drug-induced lysis observed in this work.

Our work also raises intriguing questions about how genetic resistance determinants might spread in biofilm populations, even in the absence of the strong selection pressure of high drug concentrations. A quantitative understanding of biofilm forma-

tion may also inspire new optimized dosing protocols, similar to those in, for example, [37, 38, 39], and the current model could be easily extended to investigate the effects of clinically realistic antibiotic dosing regimens. In the long run, these results may lay the groundwork for improved, systematic design of biofilm-specific therapies [40, 41].

2.4 Methods

2.4.1 Bacterial strains and media

Experiments were performed with *Enterococcus faecalis* V583, a fully sequenced clinical isolate [42], and strain OG1RF, which was derived from human oral isolate OG1 [43]. For each experiment, starting cultures (3 mL) were inoculated from a single colony on brain heart infusion (BHI) agar plates (1.5% (w/v) bacteriological agar) and grown overnight in BHI or tryptic soy broth (TSB) medium at 37°C without shaking.

2.4.2 Drugs

Antibiotics used in this study are listed in table 2.1. Antibiotic stock solutions were sterilized by passing through 0.22 μm filter, aliquoted into daily-use volumes, and kept at -20 or -80°C for no more than 3-6 months. All chemicals and media were purchased from Sigma-Aldrich or Fisher Scientific unless stated otherwise.

2.4.3 Growth curves of *Enterococcus faecalis*

Overnight cultures were diluted 100X into fresh BHI medium, and then 200 μL of diluted culture were added to each well of a 96-well clear bottom plate. Different concentrations of antibiotics were then added to each well, and time series of optical

Antibiotics	Description	Abbreviation
Ampicillin	Cell wall synthesis inhibitor	AMP
Ceftriaxone	Cell wall synthesis inhibitor	CRO
Fosfomycin	Cell wall synthesis inhibitor	FOF
Oxacillin	Cell wall synthesis inhibitor	OXA
Doxycycline	Inhibit 30s subunit	DOX
Spectinomycin	Inhibit 30s subunit	SPT
Erythromycin	Inhibit 50s subunit	ERM
Linezolid	Inhibit 50s subunit	LZD
Ciprofloxacin	DNA synthesis inhibitor	CIP
Norfloxacin	DNA synthesis inhibitor	NOR
Rifampin	RNA synthesis inhibitor	RIF
Trimethoprim	Folic Acid synthesis inhibitor	TMP

Table 2.1: **Antibiotics used in this study**

density (OD600) were measured at 15 minute intervals for 24 hours at 30°C using an EnSpire Multimode Plate Reader in a temperature controlled warm room.

2.4.4 Microtiter plate biofilm assay

We measured biofilm mass in bulk assays using a well-established crystal violet staining assay [44, 45]. Overnight cultures were diluted 100X into fresh BHI medium, and then 100 μL of diluted culture (along with appropriate concentrations of antibiotics, if relevant) were added to each well of a flat-bottomed polystyrene microtiter 96-well plate (Greiner Bio-One Cellstar). The plate was incubated at 37°C without shaking for 24 hours. After incubation, supernatant from liquid cultures was removed by gently turning over the plate, shaking, and patting on paper towels. Wells were then gently washed with PBS. To fix the biofilm on the plate, 125 μL 96% ethanol was added into each well and allowed to incubate for 20 minutes. Ethanol was then removed and the plate was dried at room temperature for half an hour. Following drying, 125 μL 0.5% crystal violet was then added to stain the biofilm mass. After 30 minutes, plates were washed multiple times with fresh PBS. Plates was then turned upside down and dried for 1 hour. Finally, 125 μL 30% acetic acid was added to each

well in order to dissolve biofilm. Solutions were transferred to a new 96-well plate and absorbance readings at 590 nm were taken using Enspire multimodal plate reader. For each treatment, we performed 6-12 replicates.

2.4.5 ATP detection assay

To measure cell lysis, we used the luminescence assay described in [17] to measure increases in extracellular ATP using a commercial ATP Determination kit (Molecular Probes). Prior to measuring cell lysis, biofilms were grown as previously described with different concentrations of antibiotics in a 96-well plate for 24 hours. We then washed the plate twice with nuclease-free water and removed excess liquid. After washing, 10 μL nuclease-free water was added to each well and biofilms were scraped down by using inoculation loops or pipette tips. Solutions were transferred to a new 96-well white polystyrene plate (Thermo Scientific Nunc F96 MicroWell) and 90 μL ATP standard assay solution from ATP Determination kit (Molecular Probes) was added to each sample. Luminescence was measured by plate reader.

2.4.6 Confocal laser scanning microscopy

Bacterial cultures (200 μL total volume, with appropriate drug treatment) were grown in replicates of 4 in 16-well chambered coverglass vessels. After incubating for 24 hours, liquid was removed and plate was washed twice with filtered millipore water and then stained using LIVE/DEAD BacLight Bacterial Viability kit (Molecular Probes) for 20 minutes. After staining, liquid was removed and coverglass was afixed to the top of the chamber.

The biofilms were imaged using a Zeiss LSM700 confocal laser scanning microscope (40X, 1.4 N.A. objective (Zeiss)) with laser lines 488 nm and 555 nm used for excitation. For each well, four image stacks (160 x 160 microns) spanning 20-30 microns

(vertically) at 1 micron intervals were taken at four separate (x,y) locations on the cover slip, giving a total of 16 biofilm images per condition. To analyze images, we split them into red and green channels, set the threshold for each slice individually using automated thresholding algorithms in ImageJ, and then used a watershed algorithm to segment cells and determine location and size of each cell type (live / dead) in each slice. Cell counts per slice were averaged over three well-separated slices (to avoid double counting cells in adjacent slices) in the middle portion of each biofilm and over all 16 images per condition.

2.4.7 Extracellular DNA/RNA extraction

Biofilms were grown in triplicate with ampicillin 0, 0.1 and 0.2 μg/mL in 6-well polystyrene plates with a total volume of 5 mL for each well. After 24 hours, we dumped out liquid and washed the plate twice with PBS before adding 1 mL 1X Tris-EDTA (TE, 10mM Tris-Cl, 1 mM EDTA, pH=8.0) buffer and scraping biofilms from bottom of plates.

After harvesting biofilms, cells were removed by centrifugation and supernatant was purified by using only the binding and washing steps in QIAprep Spin Miniprep kit according to the manufacturer's instruction. 5 volumes of PB buffer was added to 1 volume of supernatant and mixed. 800 μL of solution was transferred to a spin column and centrifuged at 13000 rpm for 1 minute. A volume of 0.5 mL PB buffer was added to wash the spin column followed by centrifugation for 1 minute. Then 0.75 mL PE buffer was added to spin column, and the column was centrifuged again for 1 minute. The flow-through was discarded and residual was removed by centrifuging spin column for an additional 1 minute. The column was then transferred to a new 1.5 mL microcentrifuge tube and 30 μL EB buffer was added to the center of the spin column. After 1 minute, the column was centrifuged for 1 minute to elute DNA.

DNase I or RNase was added to the same treatment samples as controls.

2.4.8 Agarose gel electrophoresis

Gel tray and all related tools were rinsed with nuclease-free water, and samples were loaded on a 1% agarose gel with 1X Tris-acetate-EDTA (TAE, pH=8.4) buffer containing an appropriate volume of SYBR safe. The gel was run at 120V for 40 mins in 1X TAE buffer. DNA or RNA fragments were virtualized under UV light from UV transilluminator. To analyze images, ImageJ software was used to subtract background and perform intensity analysis for different lanes. Identically sized regions were selected for different lanes and a profile plot of each lane was drawn. A straight line across the base of the peak was drawn to enclose the peak, and the wand tool was used to select each peak and measure percentage of relative densities.

2.5 Appendix: Biofilms at Sub-Inhibitory Concentrations Supplemental Information

This supporting material contains a detailed description of the mathematical model and analysis as well as three supplemental figures, including experimental measurements of growth and cell lysis in planktonic cultures and gel images of eDNA (Figure S1), analysis of approximate solutions to the mathematical model (Figure S2), and experimental measurements of cell lysis in biofilms exposed to a chemical lysis inhibitor (Figure S3). The ordering of the figures follows the order in which they are referenced in the main text.

2.5.1 Mathematical Model

To model lysis-induced biofilm formation, we consider a simple model given by

$$\begin{aligned} \frac{dN}{dt} &= g\left(1-\frac{N}{K}\right)N - rN + cLf(D) \\ \frac{dD}{dt} &= rN - \gamma D \end{aligned} \tag{2.6}$$

where N is the living cell mass in the biofilm, D is the mass of lysed (dead) cells and dead cell material, and L is the number of living cells in the planktonic media. In the first equation, the first term describes logistic growth (with per capita growth g and carrying capacity $K > 0$), the second describes cell death (lysis) with rate $r \geq 0$, and the last term describes the increase in biofilm mass due to surface attachment of living cells in the planktonic phase. When $f(D)$ is a constant, cells attach to the biofilm at a rate proportional to the number of cells in the planktonic phase ($L > 0$) times a rate parameter $c > 0$; more general choices for $f(D)$ couple biofilm induction to cell lysis, which we show below is required to achieve a peak in N as a function of lysis. In the second equation, the first term accounts for cell lysis and the second term describes a decay of dead (lysed) cell material due to, for example, detachment from the biofilm. The model includes two parameters, r and L, that depend on drug concentration, which we call a. In what follows, we begin our analysis under mild assumptions on $r(a)$ and $L(a)$. Then, for a more detailed analysis, we resort to specific functional forms which can be estimated, up to a scaling constant, directly from experimental data.

2.5.1.1 Biofilm formation uncoupled from lysis

We first consider a simple case where biofilm formation is uncoupled from cell lysis, i.e. $f(D) =$ constant (which we subsume into the constant c without loss of generality). In this case, Equation 2.6 can be written in terms of dimensionless variables $n = N/K$,

$d = Dg/(Kr)$, and rescaled time $\tau = tg$ as

$$\begin{aligned} \frac{dn}{d\tau} &= (1-n)\, n - r_0 n + L_0 \\ \frac{dd}{d\tau} &= n - \gamma_0 d \end{aligned} \tag{2.7}$$

where $r_0 = r/g$, $L_0 = cL/(gK)$, and $\gamma_0 = \gamma/g$. In the steady state, we have

$$\begin{aligned} n^* &= \frac{1}{2}\left(1 - r_0 + \sqrt{(1-r_0)^2 + 4L_0}\right) \\ d^* &= \frac{1}{2\gamma_0}\left(1 - r_0 + \sqrt{(1-r_0)^2 + 4L_0}\right) \end{aligned} \tag{2.8}$$

where we have kept only the physically meaningful (positive) root. It is straightforward to show that this steady state is always a stable fixed point ($\mathrm{tr}J < 0$ and $\det J > 0$, where J is the Jacobian of the system in Equation 2.7 evaluated at (n^*, d^*)).

It is intuitively clear that this model does not exhibit a non-zero peak in n^* as a function of antibiotic a. Recall that the dependence on a arises from $r_0(a)$ and $L_0(a)$, which are functions of drug concentration. If we make the physically reasonable assumptions that, for $a > 0$, $r_0'(a) > 0$ (lysis increases with drug) and $L_0'(a) < 0$ (planktonic cells decrease with drug) –both of which are consistent with experimental measurements–the derivative of $n^*(a)$ is always negative. Specifically, we have

$$\frac{dn^*(a)}{da} = \frac{1}{2}\left(r_0'(a)(\lambda - 1) + \frac{2L_0'(a)}{\sqrt{4L_0(a) + (r_0(a)-1)^2}}\right) \tag{2.9}$$

where primes indicate differentiation with respect to a and $\lambda = \frac{r_0(a)-1}{\sqrt{4L_0(a)+(r_0(a)-1)^2}}$. Because $|\lambda| \leq 1$, both terms are negative, indicating that $n^*(a)$ is always decreasing and cannot exhibit a maximum for $a > 0$.

2.5.1.2 Biofilm formation coupled to lysis

To capture experimental observations in a minimal model, we consider Equation 2.6 with $f(D) = D$, so that the mass of dead (lysed) cells is coupled to living biofilm mass. We can write Equation 2.6 in terms of rescaled variables $n = N/K$, $d = Dg/(Kr)$, and $\tau = tg$ as

$$\begin{aligned} \frac{dn}{d\tau} &= (1-n)\, n - r_0 n + \gamma_0 L_0 r_0 d \\ \frac{dd}{d\tau} &= n - \gamma_0 d \end{aligned} \tag{2.10}$$

where $r_0 = r/g$, $L_0 = cL/\gamma$, and $\gamma_0 = \gamma/g$. In the steady state, we have

$$\begin{aligned} n^* &= 1 + r_0\,(L_0 - 1) \\ d^* &= \frac{1}{\gamma_0}\,(1 + r_0\,(L_0 - 1)) \end{aligned} \tag{2.11}$$

We restrict our analysis to the physically-meaningful regime $r_0(1 - L_0) < 1$, where the steady state values n^* and d^* are positive definite. In this regime, the steady state solution Equation 2.11 is always a stable fixed point ($\mathrm{tr}J < 0$ and $\det J > 0$, where J is the Jacobian of the system in Equation 2.10 evaluated at (n^*, d^*)).

To look for enhancement of biofilm (living) mass as a function of a, we derive a simple phase diagram illustrating the region of parameter space where $n^*(a) > n^*(0)$; that is, we look for regions where living biofilm mass is higher in the presence of drug than in its absence. To do so, we plot the curve given by

$$n^*(a) - n^*(0) = 0, \tag{2.12}$$

which after rearrangement becomes

$$L_0(a) = \frac{r_0(0)(L_0(0) - 1)}{r_0(a)} + 1. \tag{2.13}$$

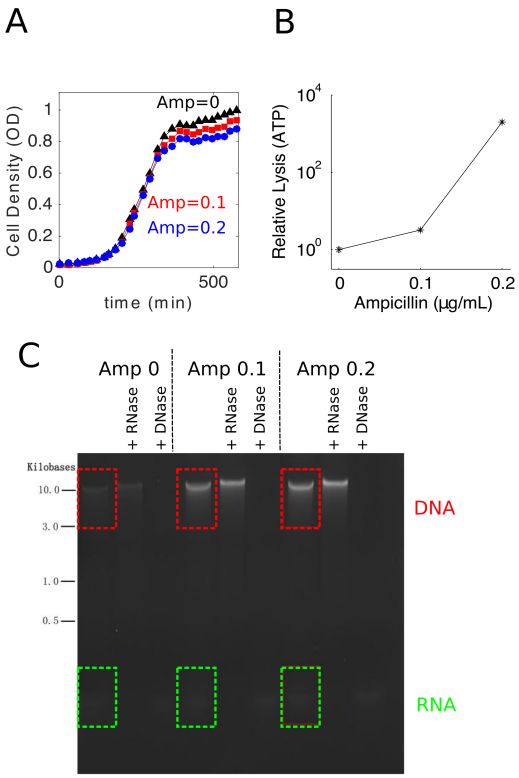

Figure 2.6: **Growth, Cell Lysis, and eDNA measurements** A. Growth curves of planktonic populations (V583, BHI) for ampicillin at 0 (black triangles), 0.1 μg/mL (red squares), and 0.2 μg/mL (blue circles). OD is normalized so that OD=1 at the last time point in the absence of drug. B. Subinhibitory concentrations of ampicillin increase cell lysis in planktonic populations. Error bars are $\pm$ standard error of the mean over replicates. Lysis is measured by ATP-based luminescence assay (Methods). C. Gel image following electrophoresis of nucleic acid isolated from biofilms. eDNA and eRNA are quantified within the red and green dashed boxed regions, respectively. For example, eDNA was considered to be bands larger than 3.0 kilobases. Additional lanes show effects of treatment with RNase or DNase; these treatments were used to determine the approximate regions corresponding to eDNA and eRNA, respectively. This experiment was performed three times on three different days; while the quantitative results (e.g. total eDNA/eRNA intensity) vary from day-to-day, the trends are always similar to those shown in Figure 3C. Note that eRNA bands are considerably lighter than eDNA bands.

In terms of the original model parameters, we have

$$L(a) = \frac{\gamma r(0)(L(0)-1)}{c}\frac{1}{r(a)} + \frac{\gamma}{c}. \tag{2.14}$$

Equation 2.14 shows that $L(a) = \frac{2\gamma}{c}$ for $r(a) = r(0)(L(0)-1)$ and asymptotically approaches $\frac{\gamma}{c}$ as $r(a) \to \infty$. The curve separates regions where drug decreases biofilm formation from those regions with enhanced biofilm formation (Figure 5). Enhanced biofilm formation therefore depends on the path taken through $(r(a), L(a))$ space as a is increased from 0. In words, enhanced biofilm formation is favored by high lysis $r(a)$ and large planktonic populations $L(a)$, and the specific dependence of these functions on drug concentration determines whether drug will increase or decrease biofilm mass. To find the location of the biofilm peak, we differentiate Equation 2.11 with respect to a, leading to

$$\frac{dn^*(a)}{da} = r_0(a)L_0'(a) + (L_0(a)-1)\, r_0'(a) = 0. \tag{2.15}$$

The existence and location of an optimum is determined by properly scaled functions–and the corresponding first derivatives–describing lysis ($r_0(a)$) and the decay of living cells in the planktonic phase ($L_0(a)$) as a function of drug. Both of these functions can be independently measured–up to a scaling constant– in our experiments. In turn, these two scaling constants become free parameters which can be estimated, for example, from the peak height and peak location in our biofilm experiments.

To make further analytical progress, we assume that $r(a)$ and $L(a)$ take the following functional forms

$$\begin{aligned} r_0(a) &= r_{01}(r_{00} + a^2) \\ L_0(a) &= \frac{\epsilon}{(1+a^h)} \end{aligned} \tag{2.16}$$

where r_{00} and r_{01} describe the increase in lysis as a function of a, ϵ is a positive definite parameter that captures the effective coupling between biofilm formation and

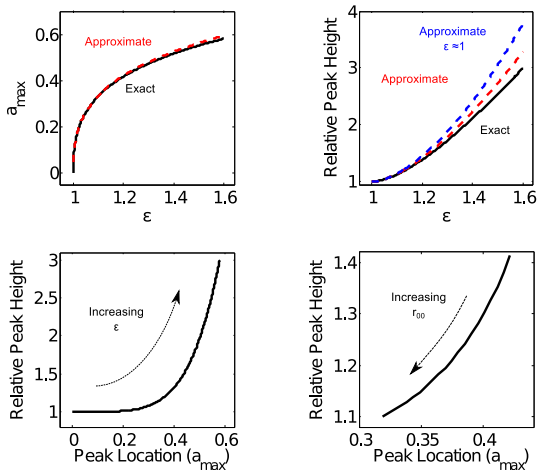

Figure 2.7: **Model predictions showing changes in ϵ and r_{00} shift peak location and peak height.** Top left: Approximate equation for peak location (Equation 2.23, red dashed) and exact value (black). Top right: Approximate equation for peak height (Equation 2.24, red dashed), $\epsilon \approx 1$ expansion (Equation , blue dashed) and exact value (black). Bottom left: Peak height vs. peak location (exact) for $1 \leq \epsilon \leq 1.6$. Bottom right: Peak height vs. peak location (exact) for $0 \leq r_{00} \leq 0.2$. Parameters r_{00}, r_{01} and ϵ were chosen to match the range observed in experiments. $r_{01} = 20$ for all panels. $r_{00} = 0.01$ for top panels and bottom left panel. $\epsilon = 1.2$ for bottom right panel.

cell lysis, h is a hill coefficient, and a is measured in units of the drug's half-maximal inhibitory concentration (IC50). Based on experimental measurements (Figure 3), we estimate $r_{00} = 0.010 \pm 0.001 << 1$, $h = 3.2 \pm 0.2$, and the drug's IC50 is given by 0.38 ± 0.01 μg/mL. For mathematical simplicity, we take $h = 3$ in what follows. As we will see, the remaining two parameters (ϵ and r_{01}) determine the location and the height of the peak in biofilm production as a function of a.

Plugging Equations 2.16 into Equation 2.15 yields a nonlinear equation that can be solved numerically to yield the peak location a_{max}. Specifically, we have $r_0'(a) = 2r_{01}a$ and $L_0'(a) = -\frac{\epsilon 3a^2}{(1+a^3)^2}$, which leads to

$$\begin{aligned} -r_{01}(r_{00} + a_{max}^2)\left(\frac{\epsilon 3 a_{max}^2}{(1+a_{max}^3)^2}\right) + \\ 2a_{max}r_{01}\left(\frac{\epsilon}{1+a_{max}^3} - 1\right) = 0. \end{aligned} \tag{2.17}$$

We simplify the above equation by multiplying both sides by $-(1+a_{max}^3)^2/r_{01}$, leading

to

$$2a_{max}^6 + (4+\epsilon)a_{max}^3 + 3\epsilon r_{00} a_{max} + 2(1-\epsilon) = 0, \tag{2.18}$$

where we have factored out the $a_{max} = 0$ solution. Equation 2.18 has $a_{max} > 0$ solutions only when $\epsilon > 1$. Because we expect this peak to occur in the subinhibitory regime of antibiotic concentration, we assume $a << 1$ and ignore the sixth order term to give

$$a_{max}^3 + \delta a_{max} + \omega = 0 \tag{2.19}$$

with $\delta \equiv \frac{3\epsilon r_{00}}{4+\epsilon}$ and $\omega \equiv \frac{2(1-\epsilon)}{(4+\epsilon)}$. Since r_{00} is estimated to be on the order of 10^{-2}, we assume $\delta << 1$ and expand a_{max} in a power series as

$$a_{max} = a_0 + a_1\delta + ... \tag{2.20}$$

Subbing this expression into Equation 2.19 and equating like powers of δ, we have

$$a_0 = (-\omega)^{1/3} = \left(\frac{2(\epsilon-1)}{4+\epsilon}\right)^{1/3} \tag{2.21}$$

and

$$a_1 = -\frac{1}{3a_0} = -\frac{1}{3\left(\frac{2(\epsilon-1)}{4+\epsilon}\right)^{1/3}}. \tag{2.22}$$

To first order in δ, then, the peak location is given by

$$a_{max} = \left(\frac{2(\epsilon-1)}{4+\epsilon}\right)^{1/3} - \frac{\epsilon r_{00}}{(4+\epsilon)^{2/3}\left(2(\epsilon-1)\right)^{1/3}} \tag{2.23}$$

In this limit, the peak occurs for nonzero a_{max} when $\epsilon > 1$, and increasing ϵ further shifts the peak to higher antibiotic concentrations. Interestingly, Equation 2.23 also shows that increasing the native level of cell lysis (i.e. increasing r_{00}) is expected to shift the peak to lower values of a.

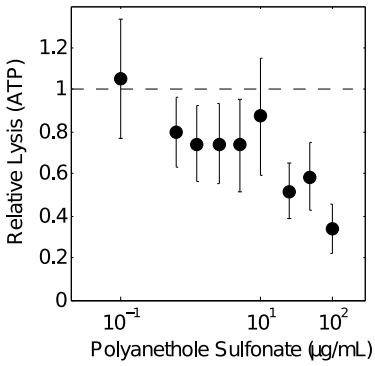

Figure 2.8: **Sodium Polyanethole Sulfonate (SPS) reduces cell lysis in biofilms.** The figure shows cell lysis (relative to untreated cells) as a function of SDS concentration as measured by ATP luminescence assay (see Methods). Error bars are ± standard error of the mean from eight replicates.

We can also plug Equation 2.23 into the expression for n^* (Equation 2.11) to get an expression for the peak height, p_h. The full expression is cumbersome, even to first order in δ, but the 0th order approximation ($\delta = 0$) is given by

$$p_h = 1 + \frac{2^{2/3}(\epsilon^2 + \epsilon - 2)r_{01}}{2 + 3\epsilon}\left(\frac{\epsilon - 1}{4 + \epsilon}\right)^{2/3} \tag{2.24}$$

For ϵ just above 1, the expression can be expanded to yield

$$p_h \approx 1 + \frac{3}{5}\left(\frac{2}{5}\right)^{2/3} r_{01}(\epsilon - 1)^{5/3} \tag{2.25}$$

which makes it clear that increasing ϵ increases the peak height.

Figure 2.7 shows that the approximate solutions derived above capture the ϵ dependence of relative peak height and peak location well (top panels). The model predicts that increasing ϵ leads to an increase in both peak height and peak location (bottom left panel). On the other hand, increasing r_{00} leads to a decrease in both relative peak height and peak location (bottom right panel). It's instructive to consider these trends in terms of the original model parameters. Rewriting the second equation in

Equation 2.16 in terms of the original model parameters, we have

$$\frac{cL(a)}{\gamma} = \frac{\epsilon}{(1+a^h)}. \tag{2.26}$$

Hence $\epsilon = \frac{cL(0)}{\gamma}$. Increasing ϵ therefore corresponds to 1) increasing the coupling between biomass material and lysis (c), 2) decreasing the decay rate of lysed cell material (γ), and/or 3) increasing the number of living cells in solution ($L(0)$). In terms of experimental perturbations, ϵ could be decreased by treating biofilms with DNase, which underlies the hypothesized biological coupling between lysis and biofilm formation. This treatment would therefore be expected to increase γ, the decay rate of lysed cell material (i.e. eDNA). A second way of decreasing ϵ would be to decrease the number of living cells in planktonic phase ($L(0)$). One possibility is to treat the cells with a second (non-lysis-inducing) antibiotic; indeed, treatments with tetracycline and rifampicin decrease the height of the peak to almost zero (Figure 5). Decreasing r_{00} corresponds to decreasing the basal level of cell lysis (for example, by adding a cell lysis inhibitor, Figure 5).

2.6 Bibliography

[1] Sara Mitri, João B Xavier, and Kevin R Foster. Social evolution in multispecies biofilms. *Proceedings of the National Academy of Sciences*, 108(Supplement 2):10839–10846, 2011.

[2] Lucas R Hoffman, David A D'argenio, Michael J MacCoss, Zhaoying Zhang, et al. Aminoglycoside antibiotics induce bacterial biofilm formation. *Nature*, 436(7054):1171, 2005.

[3] Dan I Andersson and Diarmaid Hughes. Microbiological effects of sublethal levels of antibiotics. *Nature reviews. Microbiology*, 12(7):465, 2014.

[4] Jeffrey B Kaplan. Antibiotic-induced biofilm formation. *Int J Artif Organs*, 34(9):737–751, 2011.

[5] Don B Clewell, Michael S Gilmore, Yasuyoshi Ike, and Nathan Shankar. *Enterococci: from commensals to leading causes of drug resistant infection*. Massachusetts Eye and Ear Infirmary, 2014.

[6] Jamal A Mohamed and David B Huang. Biofilm formation by enterococci. *Journal of medical microbiology*, 56(12):1581–1588, 2007.

[7] Lynn E Hancock and Marta Perego. The enterococcus faecalis fsr two-component system controls biofilm development through production of gelatinase. *Journal of bacteriology*, 186(17):5629–5639, 2004.

[8] Vinai Chittezham Thomas, Lance R Thurlow, Dan Boyle, and Lynn E Hancock. Regulation of autolysis-dependent extracellular dna release by enterococcus faecalis extracellular proteases influences biofilm development. *Journal of bacteriology*, 190(16):5690–5698, 2008.

[9] Vinai Chittezham Thomas, Yasuaki Hiromasa, Nathan Harms, Lance Thurlow, John Tomich, and Lynn E Hancock. A fratricidal mechanism is responsible for edna release and contributes to biofilm development of enterococcus faecalis. *Molecular microbiology*, 72(4):1022–1036, 2009.

[10] Pascale S Guiton, Chia S Hung, Kimberly A Kline, Robyn Roth, Andrew L Kau, Ericka Hayes, John Heuser, Karen W Dodson, Michael G Caparon, and Scott J Hultgren. Contribution of autolysin and sortase a during enterococcus faecalis dna-dependent biofilm development. *Infection and immunity*, 77(9):3626–3638, 2009.

[11] Vijayalakshmi S Iyer and Lynn E Hancock. Deletion of σ54 (rpon) alters the rate of autolysis and biofilm formation in enterococcus faecalis. *Journal of bacteriology*, 194(2):368–375, 2012.

[12] NS Jakubovics, RC Shields, Nithyalakshmy Rajarajan, and JG Burgess. Life after death: the critical role of extracellular dna in microbial biofilms. *Letters in applied microbiology*, 57(6):467–475, 2013.

[13] Theerthankar Das, Shama Sehar, and Mike Manefield. The roles of extracellular dna in the structural integrity of extracellular polymeric substance and bacterial biofilm development. *Environmental microbiology reports*, 5(6):778–786, 2013.

[14] Mira Okshevsky and Rikke Louise Meyer. The role of extracellular dna in the establishment, maintenance and perpetuation of bacterial biofilms. *Critical reviews in microbiology*, 41(3):341–352, 2015.

[15] Jeffrey B Kaplan, Era A Izano, Prerna Gopal, Michael T Karwacki, Sangho Kim, Jeffrey L Bose, Kenneth W Bayles, and Alexander R Horswill. Low levels of β-lactam antibiotics induce extracellular dna release and biofilm formation in staphylococcus aureus. *MBio*, 3(4):e00198–12, 2012.

[16] William R Greco, Gregory Bravo, and John C Parsons. The search for synergy: a critical review from a response surface perspective. *Pharmacological reviews*, 47(2):331–385, 1995.

[17] Aaron MT Barnes, Katie S Ballering, Rachel S Leibman, Carol L Wells, and Gary M Dunny. Enterococcus faecalis produces abundant extracellular structures containing dna in the absence of cell lysis during early biofilm formation. *MBio*, 3(4):e00193–12, 2012.

[18] JAMES B Cornett and GERALD D Shockman. Cellular lysis of streptococcus faecalis induced with triton x-100. *Journal of bacteriology*, 135(1):153–160, 1978.

[19] Yaseelan Palarasah, Mikkel-Ole Skjoedt, Lars Vitved, Thomas Emil Andersen, Karsten Skjoedt, and Claus Koch. Sodium polyanethole sulfonate as an inhibitor of activation of complement function in blood culture systems. *Journal of clinical microbiology*, 48(3):908–914, 2010.

[20] J Wecke, M Lahav, I Ginsburg, E Kwa, and P Giesbrecht. Inhibition of wall autolysis of staphylococci by sodium polyanethole sulfonate "liquoid". *Archives of microbiology*, 144(2):110–115, 1986.

[21] Kunihiko Yabu and Shunko Kaneda. Salt-induced cell lysis of staphylococcus aureus. *Current microbiology*, 30(5):299–303, 1995.

[22] Amparo M Gallardo-Moreno, Henny C van der Mei, Henk J Busscher, and Ciro Pérez-Giraldo. The influence of subinhibitory concentrations of ampicillin and vancomycin on physico-chemical surface characteristics of enterococcus faecalis 1131. *Colloids and Surfaces B: Biointerfaces*, 24(3):285–295, 2002.

[23] Amparo M Gallardo-Moreno, Henny C van der Mei, Henk J Busscher, M Luisa González-Martın, José M Bruque, and Ciro Pérez-Giraldo. Adhesion of enterococcus faecalis 1131 grown under subinhibitory concentrations of ampicillin and vancomycin to a hydrophilic and a hydrophobic substratum. *FEMS microbiology letters*, 203(1):75–79, 2001.

[24] Juan Ramón Maestre, Lorenzo Aguilar, María Mateo, María-José Giménez, María-Luisa Méndez, Luis Alou, Juan-José Granizo, and José Prieto. In vitro interference of tigecycline at subinhibitory concentrations on biofilm development by enterococcus faecalis. *Journal of antimicrobial chemotherapy*, 67(5):1155–1158, 2012.

[25] Tiane Martin de Moura, Fabrício Souza Campos, Juliana Caierão, Ana Claudia Franco, Paulo Michel Roehe, Pedro Alves d'Azevedo, Jeverson Frazzon, and Ana Paula Guedes Frazzon. Influence of a subinhibitory concentration of vancomycin on the in vitro expression of virulence-related genes in the vancomycin-resistant enterococcus faecalis. *Revista da Sociedade Brasileira de Medicina Tropical*, 48(5):617–621, 2015.

[26] Julian Davies, George B Spiegelman, and Grace Yim. The world of subinhibitory antibiotic concentrations. *Current opinion in microbiology*, 9(5):445–453, 2006.

[27] Luisa Laureti, Ivan Matic, and Arnaud Gutierrez. Bacterial responses and genome instability induced by subinhibitory concentrations of antibiotics. *Antibiotics*, 2(1):100–114, 2013.

[28] Howard M Shapiro. Multiparameter flow cytometry of bacteria: implications for diagnostics and therapeutics. *Cytometry Part A*, 43(3):223–226, 2001.

[29] Lutz Netuschil, Thorsten M Auschill, Anton Sculean, and Nicole B Arweiler. Confusion over live/dead stainings for the detection of vital microorganisms in oral biofilms-which stain is suitable? *BMC Oral Health*, 14(1):2, 2014.

[30] Fernando Oliveira, Cláudia Afonso Lima, Susana Brás, Ângela França, and Nuno Cerca. Evidence for inter-and intraspecies biofilm formation variability among a small group of coagulase-negative staphylococci. *FEMS microbiology letters*, 362(20), 2015.

[31] Mareike Klinger-Strobel, Herbert Suesse, Dagmar Fischer, Mathias W Pletz, and Oliwia Makarewicz. A novel computerized cell count algorithm for biofilm analysis. *PloS one*, 11(5):e0154937, 2016.

[32] Michael Berney, Frederik Hammes, Franziska Bosshard, Hans-Ulrich Weilenmann, and Thomas Egli. Assessment and interpretation of bacterial viability by using the live/dead baclight kit in combination with flow cytometry. *Applied and environmental microbiology*, 73(10):3283–3290, 2007.

[33] T Zotta, A Guidone, P Tremonte, E Parente, and A Ricciardi. A comparison of fluorescent stains for the assessment of viability and metabolic activity of lactic acid bacteria. *World Journal of Microbiology and Biotechnology*, 28(3):919–927, 2012.

[34] Carey D Nadell, Joao B Xavier, Simon A Levin, and Kevin R Foster. The evolution of quorum sensing in bacterial biofilms. *PLoS biology*, 6(1):e14, 2008.

[35] Harald Horn, Helmut Reiff, and Eberhard Morgenroth. Simulation of growth and detachment in biofilm systems under defined hydrodynamic conditions. *Biotechnology and Bioengineering*, 81(5):607–617, 2003.

[36] Laurent A Lardon, Brian V Merkey, Sónia Martins, Andreas Dötsch, Cristian Picioreanu, Jan-Ulrich Kreft, and Barth F Smets. idynomics: next-generation individual-based modelling of biofilms. *Environmental Microbiology*, 13(9):2416–2434, 2011.

[37] Hannah R Meredith, Allison J Lopatkin, Deverick J Anderson, and Lingchong You. Bacterial temporal dynamics enable optimal design of antibiotic treatment. *PLoS Comput Biol*, 11(4):e1004201, 2015.

[38] Cheemeng Tan, Robert Phillip Smith, Jaydeep K Srimani, Katherine A Riccione, Sameer Prasada, Meta Kuehn, and Lingchong You. The inoculum effect and band-pass bacterial response to periodic antibiotic treatment. *Molecular Systems Biology*, 8(1), 2012.

[39] Jason Karslake, Jeff Maltas, Peter Brumm, and Kevin B Wood. Population density modulates drug inhibition and gives rise to potential bistability of treatment outcomes for bacterial infections. *PLoS Comput Biol*, 12(10):e1005098, 2016.

[40] Fernanda L Paganelli, Rob J Willems, and Helen L Leavis. Optimizing future treatment of enterococcal infections: attacking the biofilm? *Trends in microbiology*, 20(1):40–49, 2012.

[41] Mira Okshevsky, Viduthalai R Regina, and Rikke Louise Meyer. Extracellular dna as a target for biofilm control. *Current opinion in biotechnology*, 33:73–80, 2015.

[42] Daniel F. Sahm, Jessica Kissinger, Michael S. Gilmore, Patrick R. Murray, Ross Mulder, Joanne Solliday, and Barbara Clarke. In vitro susceptibility studies of vancomycin-resistant enterococcus faecalis. *Antimicrobial Agents and Chemotherapy*, 33(9):1588–1591, Sept. 1989.

[43] Olga G. Gold, H.V. Jordan, and J. van Houte. The prevalence of enterococci in the human mouth and their pathogenicity in animal models. *Archs oral Biol.*, 20:473–477, 1975.

[44] Elke Peeters, Hans J. Nelis, and Tom Coenye. Comparison of multiple methods for quantification of microbial biofilms grown in microtiter plates. *Journal of Microbiological Methods*, 72:157–165, 2008.

[45] George A. O'Toole. Microtiter dish biofilm formation assay. *Journal of Visualized Experiments*, 2011.

CHAPTER III

Cooperation and Spatial Architecture of *E. faecalis* Biofilms at Superinhibitory Drug Concentrations

3.1 Introduction

After the previous set of experiments of all drug sensitive *E. faecalis* biofilms having counter intuitive peak behavior at sub-inhibitory cell wall synthesis drug concentrations[1], we wanted to further study biofilms at higher drug concentrations to see what types of collective behaviors arise with the increased drug concentrations. With super-inhibitory drug concentrations we would expect all sensitive populations to die, as our experiments study biofilms grown for the whole experiment time in the presence of drug. Using instead a mixed population of resistant and sensitive cells, new questions to address arise, such as what sort of cooperation might occur in the population and how does this depend on population composition? As cells in biofilms are spatially fixed, is there a specific spatial organization to this cooperation?

To study these questions, we used a mixed population that included resistant cells that produced the enzyme Beta-lactamase, either a clinical outbreak strain, HH22 (preliminary results) [2, 3] or the strain OG1RF, a laboratory strain transformed

with a plasmid which also fluorescently labeled the resistant cells. By producing Beta-lactamse, the resistant cells are able to deactivate drugs of the beta-lactam class, such as ampicillin. While this specific molecular mechanism is ideal for the resistant cells, in the mixed population the sensitive cells can feel the benefits of resistant cells to degrade the drug in the environment as the beta lactamse acts as a public good [4, 5, 6]. Previous work has found public good cooperation occurs both planktonically and in biofilms [7, 8, 9, 10] and we aim to further examine the spatial organization and local neighborhoods of cooperation. Studies looking at different species have indicated some species, such as *Pseudomonas*, releases beta-lactamase into the extracellular environment [11, 12], whereas others, like *E. faecalis*, hold the enzyme within individual cells [13]. Because the public good is now less 'public', this exaggerates the need for spatial organization in the biofilm: the organization of the sensitive cells in relation to the resistant cells- acting as sinks- can alter the survival of a sensitive cell. Beyond the spatial component, the starting population composition can also drastically affect the composition of the final biofilm, another factor we examine using confocal fluorescence microscopy to study each sub population.

With these spatial and composition factors in mind, we wanted to further our understanding of the interplay between cooperation and composition by creating a 2D model to describe the spatial organization. While biofilms are complex communities with many nutrients and growth factors adding to the environment, we aimed to create a simple model with rules for cooperation to explain the organizations we see. These mixed populations biofilms lead to interesting spatial organization both experimentally and computationally, showing the population level effects that can occur from a small molecular enzyme resistance mechanism.

3.2 Results

3.2.1 Biofilm Total Populations: Mixed Populations at High Drug Concentrations

Wanting to study the cooperation between the two populations on a global scale, we first measured the total population with and without drug present. We used confocal microscopy and automated cell segmentation algorithms (see Methods) to image mixed population biofilms at single cell resolution. Resistant and sensitive cells were engineered to contain a plasmid constitutively expressing the fluorescent protein Rudolph RFP (sensitive) or BFP (resistant) (see Chapter 5). The two strains were identical except for 1. the fluorescent marker used and 2. the resistant strain was engineered to constitutively express beta lactamase. We grew the mixed biofilms of resistant and sensitive cells for 24 hours on coverslips (see Methods) in concentrations of Ampicillin 0.0 μg/ml and Ampiclin 1.0 μg/ml, with Ampicillin 1.0 μg/ml chosen as sensitive cells cannot survive at this drug concentration. Following imaging of z-stacks of the biofilms, we counted the number of individual cells of each type (sens/res) from hundreds of individual slices in replicate biofilms grown under identical conditions.

Comparing biofilms of all sensitive cells (Figure 3.1A-C) to mixed sensitive and resistant biofilms (Figure 3.1D-F), we found that not only did the mixed biofilms survive at drug concentrations where the all sensitive biofilm died (Figure 3.1B,E), but confocal images showed a mixed biofilm population of resistant and sensitive cells at high drug. From image analysis and single cell segmentation, the total mass of each biofilm was measured as well and plotted, normalized to the no drug case for each population condition (Figure 3.1C,F). The total mass of the mixed population does decrease in the presence of drug, but the final population is still contains sensitive

cells surviving at clinically relevant antibiotic concentrations.

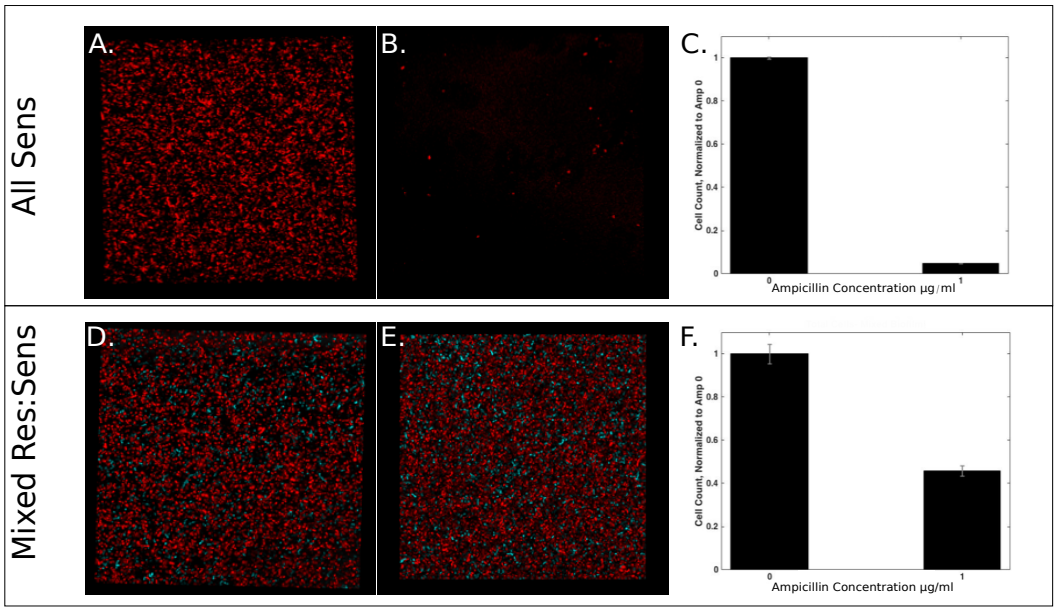

Figure 3.1: **Total Cell Populations, all sensitive and mixed population biofilms** A. Confocal image of an all sensitive biofilm at Ampicillin 0.0 μg/ml. B. Confocal image of an all sensitive biofilm at Ampicillin 1.0 μg/ml. C. Total cell counts of the sensitive biofilms at both antibiotic concentrations. D. Confocal image of a mixed biofilm at Ampicillin 0.0 μg/ml. E. Confocal image of a mixed biofilm at Ampicillin 1.0 μg/ml. F. Total cell counts of the mixed biofilms at both antibiotic concentrations. Counts are normalized to the Ampicillin 0.0 μg/ml case. Sensitive cells are fluorescently labeled with an RFP, resistant cells are fluorescently labeled with a BFP. Biofilms were grown for 24 hours in 6 well plates (see methods) before imaging. 2D slices were merged to create the 3D images shown here.

The total cell measurements from the preliminary biofilms showed sensitive cells surviving at otherwise lethal drug concentrations, raising the question of what sort of cooperation and composition is present in our biofilms. We repeated the total population measurements with experimental biofilms where the mixed resistant and sensitive cells were now the same strain, following successful cloning of a plasmid containing beta lactamase into the *E. faecalis* strain OG1RF. We also performed analysis to determine the final population composition, using cell segmentation and counting to find the population fraction of each resistant and sensitive cells as they are fluorescently labeled different colors. Figure 3.2 shows the total biofilm mass (A,B,C) and sensitive fraction (D,E,F) at Ampicillin 0.0 μg/ml and Ampicillin 1.0 μg/ml of

biofilms starting at 75%, 50% and 25% sensitive. From these experiments, the total biofilm mass generally decreases at the high drug case, but for Figure 3.2C, the biofilm mass is actually larger for the biofilm grown at higher drug, perhaps due to the fact that those populations started as 75% resistant and could easily degrade the drug. From Figure 3.2D-F, there is not a drastic decrease in the final fraction of sensitive cells when compared to their initial compositions, though it is worth noting the final fraction of sensitive cells in Figure 3.2F. As that population is 75% resistant, with no drug present, the sensitive cells have a slight growth advantage and increase their population. With drug, the resistant fraction is large and can likely quickly degrade the drug, leading to a relatively detoxified environment for the sensitive cells to thrive and again allowing the initial sensitive fraction to increase.

3.2.2 Local Interactions Account for Spatial Organization

To establish the different rules responsible for the biofilm spatial organization, a 2D agent based model was developed. As a biofilm develops, planktonic cells either deposit onto the surface or a cell already attached to the biofilm grows. The stochastic model depends on the ratio of cell deposition (from the planktonic population) and cell growth from previously seeded cells: comparing our experimental correlations to the model correlations allowed us to find what ratio to use in our model. To mimic spatially dependent cooperation, sensitive cells were given a death rate that decreased depending on the number of resistant neighbors it had. This decrease was a linear function: with no resistant neighbors, the sensitive cell had the max death rate, with all resistant neighbors, the sensitive cell had the resistant death rate (0). With each additional resistant neighbor added, there was a decrease in the death rate. Our final model has no free parameters, as the growth and deposition rates are set from two-color, all sensitive experimental biofilms and the cooperation is a known function of resistant neighbors. Two different examples of different deposition/growth ratios

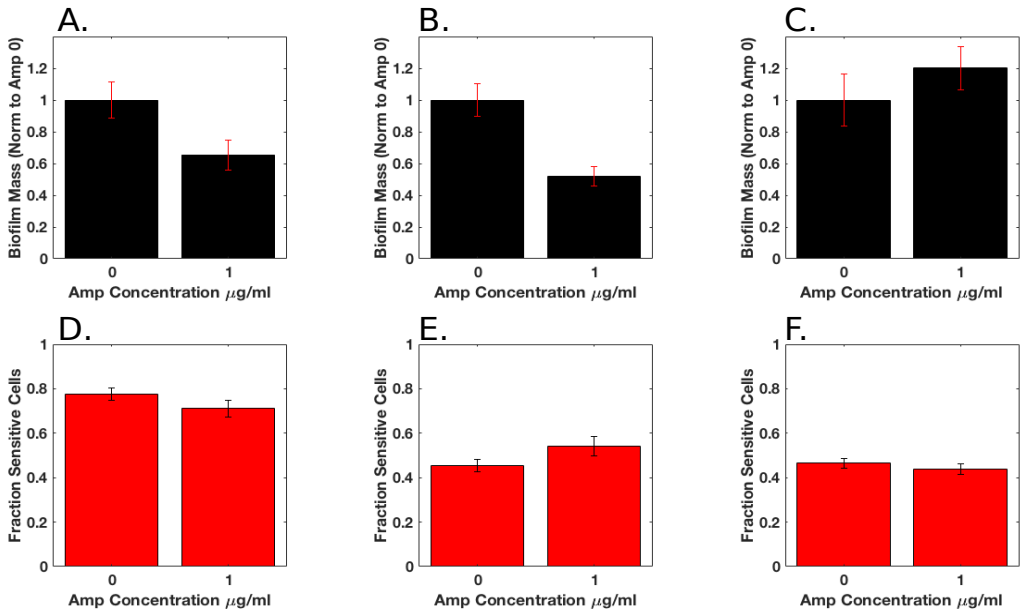

Figure 3.2: **Total Cell Populations and sensitive fractions, mixed population biofilms** A. Total biofilm mass of starting biofilms that initial compositions were 75% sensitive. B. Total biofilm mass of starting biofilms that initial compositions were 50% sensitive. C. Total biofilm mass of starting biofilms that initial compositions were 25% sensitive. For each composition, biofilms were grown at either Ampicillin 0.0 μg/ml or Ampicillin 1.0 μg/ml. Two biofilms were grown per composition and per drug concentration. Five confocal stacks were taken per biofilm, giving a total of ten biofilm stacks averaged together to find the mean and standard error of the mean. For each initial composition, the total biofilm mass was normalized to the biofilm mass of the Ampicillin 0.0 μg/ml biofilms. D. Final Sensitive fractions of starting biofilms that initial compositions were 75% sensitive. E. Final Sensitive fractions of starting biofilms that initial compositions were 50% sensitive. F. Final Sensitive fractions of starting biofilms that initial compositions were 25% sensitive. The mean and standard error were once again found from compiling the data from the 10 different biofilm stacks together.

as well as an example mean field approximation of the model are shown below in Figure 3.3. With the addition of cooperation, the local coupling between resistant and sensitive cells, in the model, our simulations produce similar spatially organized biofilms when compared to our experimental results, suggesting cooperation not only leads to a mixed population, but that population has a specific, set organization. This new prediction, of spatial organization was something we wanted to test experimentally as well.

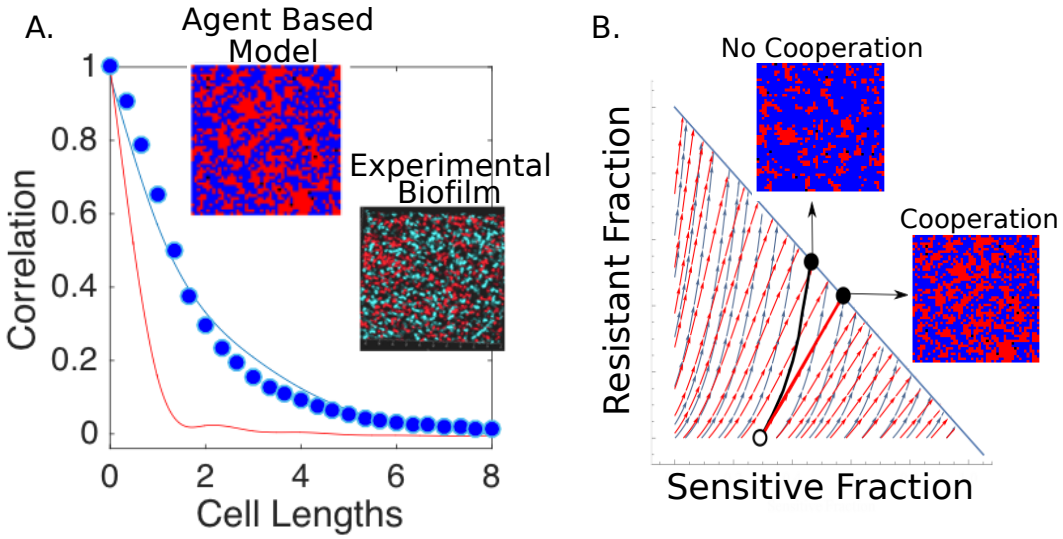

Figure 3.3: **Model fitting and Model cooperation** A. Model fitting of the ratio of cell deposition/growth. Red and blue solid lines show two different ratios from model fitting,blue circles show experimental correlation. Simulations were completed using the fit from the blue line that closely matched the experimental result. B. Comparison of the model, with the addition of a cooperative death rate for sensitive cells (more resistant neighbors, less sensitive death) to a mean field approximation. This allows characterization of the model without just comparing to simulations. For simulations, blue labeled squares ('cells') are resistant and red labeled squares ('cells') are sensitive.

3.2.3 Preliminary Spatial Organization: Local Neighborhoods

Following confirmation that the final biofilm composition is a mixture of resistant and sensitive cells and model predictions of a specific spatial organization, we wanted to investigate how that mixed composition was spatially organized in the presence of antibiotics. Using automated cell segmentation to get the position of single cells in our confocal images and knowing the cell type based on the different fluorescent markers, the local fraction of resistant cells in the neighborhood surrounding each sensitive cell (within some set radius) was determined and averaged together, with the many 2D biofilms stacks then averaged together. We see drastic differences in spatial organization between mixed biofilms grown without any drug and those grown at Ampicllin 1.0 μg/ml, with the sensitive neighborhoods being enriched for resistant cells in biofilms grown in antibiotics.

In Figure 3.4, we see without any drug present (3.4A), the fraction of resistant neighbors at small radii right around the sensitive cells are negative, indicating the local neighborhood is enriched for sensitive cells and the neighborhoods are dominated by small clonal populations. Conversely, for biofilms grown in Ampicillin (3.4B), the local neighborhoods around sensitive cells are dominated by resistant cells, with the average sensitive cell being found within one cell diameter of a resistant cell. Introducing the death rate rule in our model to mimic cooperation in a biofilm grown in the presence of drug, our agent based model shows similar spatial organization (Figure 3.4C).

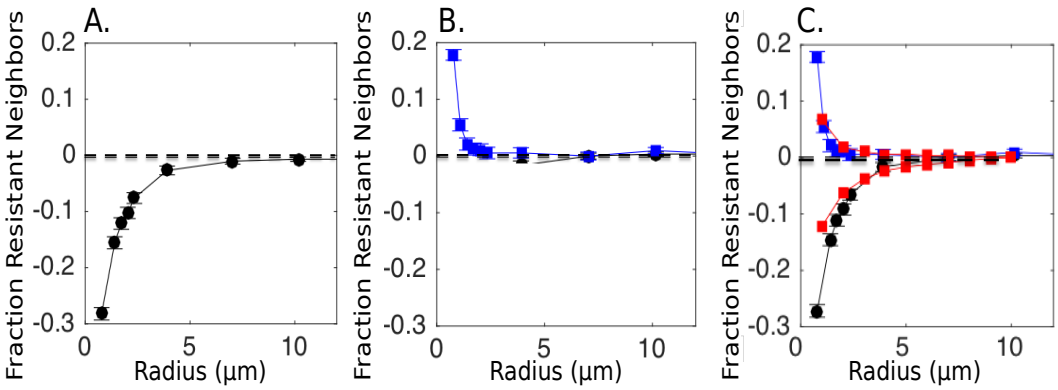

Figure 3.4: **Spatial Organization of Mixed Biofilms with and without drug present** A. Sensitive cell fraction of resistant neighbors in a mixed biofilm at Ampicllin 0.0 μg/ml. B. Sensitive cell fraction of resistant neighbors in a mixed biofilm at Ampicllin 1.0 μg/ml. C. Sensitive cell fractions both with and without drug with the agent based model results overlaid (red). For all graphs, the dashed line represents the global fraction of resistant cells in the whole biofilm. Experimental cell positions were found using imageJ and the fraction of resistant neighbors was calculated from each sensitive cell using these positions.

3.3 Discussion

From the molecular mechanism of an enzyme that breaks down the drug, these experiments demonstrate the collective cooperation that arises between resistant and sensitive populations. At super-inhibitory drug concentrations, where sensitive only

biofilms cannot form, the mixed biofilms show a coexistence of the two different populations, suggesting that not only do the resistant cells benefit from having beta lactamase to break down drug, but the enzyme acts as a public good and leads to cooperation between the resistant and sensitive cells.The benefit from a public good is not a new phenomenon in collective communities, but the presence of beta lactamase in the biofilms introduces a structural, spatial component to the cooperation as well. From our preliminary experiments studying the local neighborhoods around sensitive cells, there was a clear enrichment of the neighborhoods for resistant cells when biofilms are grown in the presence of drug, a trend that does not appear in the mixed biofilms grown without drug. Further experiments and single cell analysis done in the same strain show once again cooperation and a final biofilm that is still a mixed population, and the fraction of sensitive cells in the final population is similar between the drug and no drug case. As the enzyme beta-lactamase breaks down the drug, it detoxifies the environment enough for the sensitive cells to survive and possibly even thrive, as seen in the case where the starting population was 75% resistant. We wanted to understand the rules behind the cooperation and developed a 2D agent based model to determine what sort of cooperation could lead to the spatial organization observed. On a square 2D grid, the 'biofilm' formed either from cell deposition or growth at a specific ratio fit from experimental results and cooperation was implemented as a decrease in the death rate of sensitive cells depending on the number of resistant neighbors the cell had. Studying the spatial organization of these simulated biofilms, the model predicted similar sensitive neighborhoods enriched for sensitive cells (no drug case) or resistant cells (drug case) as seen experimentally.

After seeing the interesting spatial organization, we wanted to study the z-dependence of the composition and spatial organization, but we were limited by our confocal images: in order to avoid double counting cells, our z slices were 5 microns apart and

during automated imaging we often missed the lowest z-position. In future work, smaller z-intervals will be used and composition analysis based on z-position will be completed. We also acknowledge the simplicity of our model and recognize that biofilm communities include many more growth factors and components that we are accounting for. While this model could be expanded to either a 3D model or even a 2D hexagonal grid and more components could be added as agents, the rules to mimic cooperation- a decrease in the sensitive cell death rate depending on the number of neighboring resistant cells- leads to 2D simulated biofilms that closely mimic the experimental spatial organizations.

The spatial organization that arises in the mixed population biofilms grown at high drug concentration indicates the challenges to dosing and treating a biofilm. While biofilms of just one population have been seen to split into heterogeneous, phenotypic areas, having a mixed population extends this heterogeneity and organization, and can lead to challenges in effectively treating a biofilm. With this understanding of the organization, both experimentally and with the ABM, questions regarding how the organization effects further drug dosing and the difference the spatial organization plays in future survival- if a biofilm grown without drug is later dosed, how does it survival and population composition compare to that of a biofilm grown in drug the entire time?- remain to be answered. Our work shows how the population composition and antibiotic environment are crucial to the single cell level spatial organization of the biofilms, and this knowledge could lead to better understanding how a biofilm will behave in a new antibiotic environment.

3.4 Methods

3.4.1 Bacterial Strains, Media, and Growth Conditions

Preliminary experiments were performed with sensitive OG1RF, a fully sequenced *E. faecalis* oral isolate and resistant strain HH22 [2, 3], a clinical outbreak strain of *E. faecalis* that produces beta lactamase from a plasmid. Due to differences in growth rates, gibson assembly and cloning was performed to take the sequence of beta-lactamase and clone it onto a plasmid for use in OG1RF. Colony Polymerase Chain Reaction (PCR) of the sequence of beta lactamse was done with strain CH19 [14], another clinical outbreak strain that has beta lactamase, but it is incorporated onto the chromosome instead of in a plasmid like HH22. Following cloning, experiments were performed with only OG1RF. Cells were fluorescently labeled with the plasmid pBSU101 Rudolph RFP or BFP, and the plasmid for the resistant cells additionally contained the sequence for the enzyme Beta Lactamase. Cultures for experiments were made taking single colonies from BHI agar plates with selection antibiotics and incubated in sterile BHI (Remel) with appropriate selection antibiotic overnight at 37°C.

3.4.2 Antibiotics

Two antibiotics were used in this study: Spectinomycin Sulfate (MP Biomedicals) and Ampicillin Sodium Salt (Fisher). Spectinomyicn 120 μg/ml was necessary for plasmid upkeep and thus was present in all cultures and biofilms. Experiments were interested in studying the effects of Ampicillin.

3.4.3 Biofilms

Biofilms were grown on coverslips (Fisher) in 6 well plates overnight at 37°C. Overnights were diluted 1:100 into fresh BHI and Spectinomycin. For experimental biofilms, mix-

tures of 25%, 50%, and 75% resistant were grown in media at either 0 μg/ml or 1.0 μg/ml Ampicillin. A cartoon schematic of the six well plates and wells, as well as a example plate is shown below in Figure 3.5.

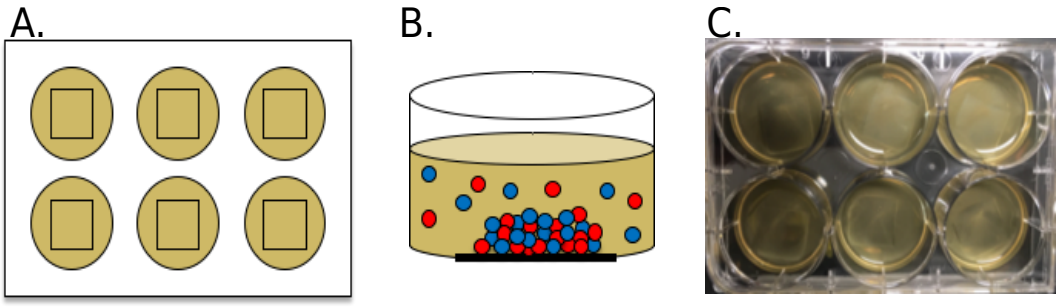

Figure 3.5: **Schematic of Biofilm Wells** A. Cartoon of a six well plate. Biofilms were grown in each well at specific starting compositions and drug concnetrations. B. Cartoon cross section of a well with a coverslip at the bottom. Following 24 hours of growth the coverslip was removed and imaged. C. Picture of a six well plate with coverslips and biofilms after 24 hours of growth.

Control biofilms were also grown of 100% resistant (either blue or red) or sensitive (either blue or red) at each antibiotic concentrations. Mixtures of the same 3 fractions of different colors, but all sensitive or all resistant cells were also grown at each antibiotic concentration. Two biofilms were grown for each fraction/Ampicillin concentration.

Following 24 hours of growth, coverslips were removed from wells and affixed to slides using 25L GeneFrames (Fisher). The adhesive frames allowed the biofilm coverslip to be affixed for imaging without needing to seal the biofilm and possibly disrupt the spatial structure.

3.4.4 Confocal Microscopy

Confocal images were taken using a Zeiss LSM700 confocal laser scanning microscope (40X, 1.4 N.A. objective (Zeiss)) with laser lines 405 nm (BFP) and 555 nm (RFP)

used for excitation. Laser power was a 5.0 for each laser and the pinhole was a 1.4 Airy Units. For each coverslip, image stacks (80x80 microns) spanning 20-30 microns (vertically) at 5 micron intervals were taken at five separate (x,y) locations on the cover slip, giving a total of 5 biofilm stacks per slip. Two coverslips were imaged for each condition, giving a total of 10 biofilm stacks per condition.

3.4.5 Image Analysis

Images were analyzed using imageJ and Matlab. LSM images were split into the blue and red channels and thresholds for each channel were set indiviually using automated thresholding alogrithims in ImageJ. Cells were segmented using a watershed algorithim to both determine the size and position of each cell. As slices were 5μm apart, each 2D slice was analyzed. The segmentation allowed us to get a total cell count for each cell type per slice, and the positions were used for correlation and nearest neighbor analysis in Matlab.

3.4.6 Agent Based Model

A 2D Agent Based Model was created to mimic biofilm formation and growth. The model is initiated on a square grid and based on the ratio of cell deposition to growth, at each time step a random point on the grid is chosen. If the square is empty, a cell has some chance of deposition and the color it will be depends on a preset parameter of starting cell type fractions. If the square already has a cell, the cell will grow with some probability to one of its four nearest neighbors, assuming there is an empty spot in the neighborhood.

To mimic cooperation and drug effects, the sensitive cells have a death rate. For simulations of a no drug case, the death rate is set to 0. For simulations with drug, the sensitive cell death rate depends on the local neighborhood: the death rate decreases

linearly with more resistant neighbors, thus increasing the chances the sensitive cell will survive and possibly grow.

3.5 Bibliography

[1] Wen Yu, Kelsey M. Hallinen, and Kevin B. Wood. Interplay between antibiotic efficacy and drug-induced lysis underlies enhanced biofilm formation at subinhibitory drug concentrations. *Antimicrobial Agents and Chemotherapy*, 62(1), Oct 2017.

[2] K K Zscheck and B E Murray. Nucleotide sequence of the beta-lactamase gene from enterococcus faecalis hh22 and its similarity to staphylococcal beta-lactamase genes. *Antimicrobial Agents and Chemotherapy*, 35(9):1736–1740, Sep 1991.

[3] B E Murray, F Y An, and D B Clewell. Plasmids and pheromone response of the beta-lactamase producer streptococcus (enterococcus) faecalis hh22. *Antimicrobial Agents and Chemotherapy*, 32(4):547–551, Apr 1988.

[4] Stuart A. West, Ashleigh S. Griffin, Andy Gardner, and Stephen P. Diggle. Social evolution theory for microorganisms. *Nature Reviews Microbiology*, 4(8):597–607, Aug 2006.

[5] Sam P. Brown, Stuart A. West, Stephen P. Diggle, and Ashleigh S. Griffin. Social evolution in micro-organisms and a trojan horse approach to medical intervention strategies. *Philosophical Transactions of the Royal Society B: Biological Sciences*, 364(1533):3157–3168, Nov 2009.

[6] Frances Medaney, Tatiana Dimitriu, Richard J Ellis, and Ben Raymond. Live to cheat another day: bacterial dormancy facilitates the social exploitation of -lactamases. *The ISME Journal*, 10(3):778–787, Oct 2015.

[7] Eugene A Yurtsev, Hui Xiao Chao, Manoshi S Datta, Tatiana Artemova, and Jeff Gore. Bacterial cheating drives the population dynamics of cooperative antibiotic resistance plasmids. *Molecular Systems Biology*, 2013.

[8] Nicole M Vega and Jeff Gore. Collective antibiotic resistance: mechanisms and implications. *Current opinion in microbiology*, 21:28–34, 2014.

[9] Robin A. Sorg, Leo Lin, G. Sander van Doorn, Moritz Sorg, Joshua Olson, Victor Nizet, and Jan-Willem Veening. Collective resistance in microbial communities by intracellular antibiotic deactivation. *PLOS Biology*, 14(12):e2000631, Dec 2016.

[10] Isabel Frost, William P.J Smith, Sara Mitri, Alvaro San Millan, Yohan Davit, James M. Osborne, Joe M. Pitt-Francis, R. Craig MacLean, and Kevin R Foster. Cooperation, competition and antibiotic resistance in bacterial colonies. *ISME*, 12:1582–1593, 2018.

[11] I. Brook. -lactamase-producing bacteria in mixed infections. *Clinical Microbiology and Infection*, 10(9):777–784, Sep 2004.

[12] O. Ciofu. Chromosomal beta-lactamase is packaged into membrane vesicles and secreted from pseudomonas aeruginosa. *Journal of Antimicrobial Chemotherapy*, 45(1):9–13, Jan 2000.

[13] B E Murray and B Mederski-Samaroj. Transferable beta-lactamase. a new mechanism for in vitro penicillin resistance in streptococcus faecalis. *Journal of Clinical Investigation*, 72(3):1168–1171, Sep 1983.

[14] L B Rice, G M Eliopoulos, C Wennersten, D Goldmann, G A Jacoby, and R C Moellering. Chromosomally mediated beta-lactamase production and gentamicin resistance in enterococcus faecalis. *Antimicrobial Agents and Chemotherapy*, 35(2):272–276, Feb 1991.

CHAPTER IV

Cooperative Dynamics Via β Lactamase in Planktonic Populations

4.1 Introduction

While *E. faecalis* biofilms show interesting collective, cooperative behaviors, both at sub and super inhibitory concentrations of antibiotics, bacteria also live planktonically, leading to the question of what sort of collective behavior might be seen in a well-stirred, mixed resistant and sensitive planktonic culture and what role does antibiotic dosing, population composition, or population density play? Though population composition still plays a critical role in survival of the community- without enough resistant cells, a mixed population will not be able to degrade the drug- the fraction of resistant cells needed to ensure survival may differ from spatial biofilms. As these cultures no longer have the fixed spatial organization seen in biofilms, cooperation and collective behavior may be influenced by other factors. Planktonic cultures introduce density effects, where the behavior of a population in a specific environment can vary based on the density of that population. A classic density dependent effect is the inoculum effect. With a set dose of antibiotic, a low density starting population can easily be totally killed. However, with that same dose of antibiotic, but a higher density starting population, the bacteria can overcome the antibiotic

and the population can ultimately thrive [1]. This effect can be seen in experiments with all sensitive cells, but our experiments expanded this idea to a mixed population of resistant and sensitive cells.

In our mixed populations of resistant and sensitive cells, there were two different relevant density effects: the resistant and reverse inoculum effect. Following the more classical inoculum effect, the resistant sub population in our culture creates a resistant inoculum effect [2]. With more resistant cells present, the total population feels the benefit from the public good effect of the enzyme, similar to the detoxifying effects of the local neighborhoods in spatially fixed biofilms. When populations of all resistant cells are at two different densities, the resistant inoculum effect leads to a difference in their growth rates; the low density resistant population cannot overcome the drug concentration, whereas the high density resistant population overcomes the drug and lives to stationary phase. (Figure 4.1A)

Conversely, because we are using the ampicillin- the same antibiotic used for the previous biofilm experiments- there is also a reverse inoculum effect. From previous work in our lab, we have seen an increase in efficacy of ampicllin as cell density increases- regardless of population composition- due to a decrease in the pH of the sample [3]. With this reverse inoculum, we now see higher density populations of all sensitive cells experiencing worse growth when compare with lower density populations exposed to the same drug concentration. (Figure 4.1B)

Considering the inoculum effects and starting densities, the cell populations will be feeling the two different effects to differing degrees. Figure 4.1C shows a schematic of the different feedback from the effects.

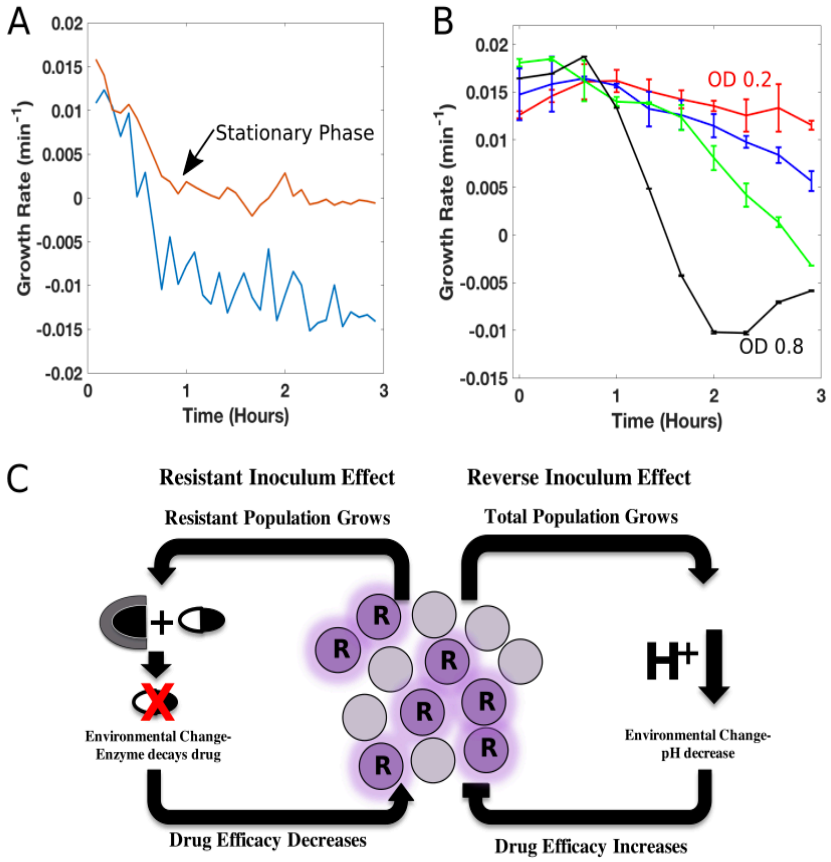

Figure 4.1: **Resistant and Reverse Inoculum effects and feedback.** A. Resistant Inoculum Effect: Resistant population started at a higher density has a higher growth rate (red line) than while the lower density resistant population growth rate (blue line). Experiments were run in a chemostat with the high density population reaching an OD of 0.6 before dosing began and the low density population reaching an OD of 0.1 before dosing began. B. Reverse Inoculum Effect: Growth rate over time of different sensitive populations held at constant densities. The higher the OD, the slower the growth. The curves, from top to bottom, are for populations held at an OD of 0.2 (red), 0.4 (blue), 0.6 (green) and 0.8 (black). C. Density Effects cartoon showing feedback from the two different inoculum effects.

To study how the planktonic community copes with antibiotic dosing, once again mixed populations of resistant and sensitive *E. faecalis* were used (similar to the populations used in chapter 3), still fluorescently labeled to distinguish between the cell types for use with FACS and measuring the population composition. The resistant cells again produce β lactamase to degrade the antibiotic [4, 5] and lead to the resistant inoculum effect, and the entire population causes a pH decrease as the population

grows leading to the reverse inoculum effect and increased drug effectiveness [6, 7]. We ran experiments in a chemostat bioreactor, a device where each culture is hooked up to a pump system [8]. The chemostat monitors the density of the samples as well as periodically dosing the samples, based on some predetermined dosing shceme, with the pump system. Mixing resistant and sensitive cells at known fractions, dosing the samples over the experimental time while monitoring their density, and measuring the final population composition, allowed us to study of the population dynamics and collective behavior of the community. Previous work has shown the ability of planktonic populations both theoretically [9, 10, 11] and experimentally to cooperative and thrive [12, 13, 14, 15, 16], but the temporal dynamics and in depth studies observing density dependence have yet to be addressed. These experiments aim to study the cooperation in planktonic *E.faecalis* populations through these two different mechanisms- enzymatic drug degradation and density pH increase in drug efficacy.

4.2 Results

4.2.1 Chemostat Density Effects

To investigate the two different proposed density effects, we first studied each effect individually. To study the reverse inoculum effect, we ran chemostat experiments at two different staring densities with our set drug dosing scheme (see Methods) using all sensitive cells. Following overnight scans, we found that as we increased the drug concentration in the drug inflow reservoir, the samples went to an intermediate fixed point between stationary phase and dying, suggesting an optimal density between death and carrying capacity that balances the increase in drug effectiveness from the pH change and the cell growth. With enough drug in the reservoir, we could ultimately kill the two samples. Due to the increased drug efficacy as density increases, our final stable samples were at lower density than stationary phase. (Figure 4.2A)

The resistant inoculum effect was studied again in our chemostat set up with the same drug dosing protocol as before, now using an all resistant population growing in buffered media. As we wanted to focus on just the resistant inoculum effect, we used buffered media to stop the environmental pH change seen from populations of cells growing, ultimately stopping the reverse inoculum effect. As our experiment should only be influenced by the resistant inoculum effect, we ran samples at low and high starting optical density with a drug reservoir for flow at an ampicillin concentration of 10 mg/ml. Following an overnight experiment, we are able to see clear bistability between the two samples, suggesting the sample with the larger starting density takes advantage of the resistant inoculum effect and is able to overcome the drug flowed into the vial. The smaller starting density sample does not have a large enough population to effectively detoxify the environment and dies. (Figure 4.2B)

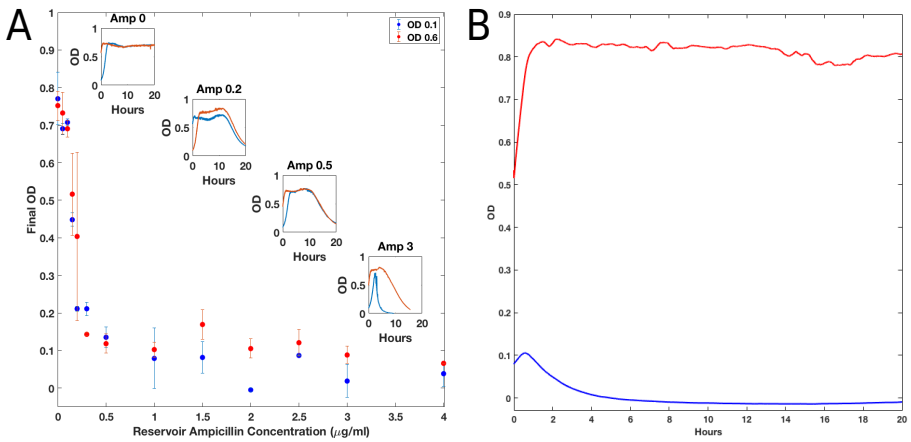

Figure 4.2: **Individual examples of the Reverse Inoculum Effect and the Resistant Inoculum Effect.** A. Final density over low ampicillin concentrations of samples of 100% sensitive cells. Samples were run at both high OD (0.6, red) and low OD (0.1, blue) overnight. Inset figures show the growth curves of the high and low density samples at four different drug resivoir concentrations. Due to the reverse inoculum effect, samples ended at an intermediate fixed point. B. Density of 100% resistant cells over time at high ampicillin concentrations in buffered media. Here again experiments are started at OD 0.6 (red) and OD 0.1 (blue). Due to the resistant inoculum effect, bistability arises as the high OD is able to degrade drug and survive.

4.2.2 Modeling Density Effects

In the interest of studying the two different inoculum effects and their feedback, a simple mathematical model was developed. Modeling the change in the number of sensitive cells (N_S), number of resistant cells (N_R), and effective drug concentration (D) as ODEs, we examined how the different density effects can change the total population outcome. With a very large experimental phase space covering numerous drug concentrations and every fraction of resistant:sensitive cells from 0% to 100%, studying the model predicted areas of interesting dynamics, and we used these predictions to drive experimental studies.

For each the sensitive and resistant cells, their growth was modeled logistically as

$$\frac{dN_i}{dt} = g_i(D)\left(1 - \frac{\Sigma N_i}{C}\right)N_i \tag{4.1}$$

where N_i is the cell type being modeled- either N_S or N_R, $g_i(D)$ is a linear growth term depending on the cell type and drug, and C is the carrying capacity. The effective drug concentration takes into account the different density effects and contains the feedback of the two different inoculum effects and is modeled as

$$\frac{dD}{dt} = -\epsilon_1 D(\Sigma N_i) + \epsilon_2 D(N_R) - D\gamma + F_0 \tag{4.2}$$

where the ϵ_1 term represents the reverse inoculum effect (dependent on the whole population density, N_S+N_R) and ϵ_1 is the strength of that effect, the ϵ_2 term represents the resistant inoculum effect (dependent only on the resistant population density, N_R) and ϵ_2 is the strength of that effect, γ is the rate of drug decay, and F_0 is the periodic drug dosing from the chemostat set up. From stability analysis and studying the fixed points of the model, we were able to develop a phase diagram of the phase space of the

initial resistant cells and the reservoir drug concentration. With the phase diagram to guide the experiments, we aimed to study the phase space experimentally.

4.2.3 Mixed Population Dynamics: Bistability

To understand the interplay between the two density effects, we studied population survival and composition at different starting resistant fractions- to observe the influence of the resistant inoculum effect- and different densities- to observe the influence of the reverse inoculum effect. Our experimental set up also allows us to run our experiments at different drug reservoir concentrations. As this is a very large experimental area- different densities, different initial population compositions, and different drug concentrations- to explore, we used the model to guide which areas would be most interesting. From a theoretical phase diagram (Figure 4.3A) generated from the model (Eqs 4.1 and 4.2), we are able to see four different regions: extinction (black), survival (white), inverse bistable (dark gray), and bistable (light gray). Using our model, we can zoom in on a cross section of the phase diagram and observe simulations of different population fractions (Figure 4.3B, C, D). Wanting to study the bistable region and compare the experimental data to the cross section we can observe in the model, overnight chemostat experiments were run at one drug concentration over a range of starting fractions and the Optical Density (OD) of the samples were measured throughout the experiment time. Representative fractions showing the three different phases (Figure 4.3E, F, G) give examples of extinction, bistability, and survival depending on the starting population composition.

4.2.4 Inverse Bistability

While studying the theoretical phases, we noticed a peculiar phase of inverse bistability, where the starting low density samples survived while the high density samples die. We wanted to study the inverse bistable phase experimentally, using the same

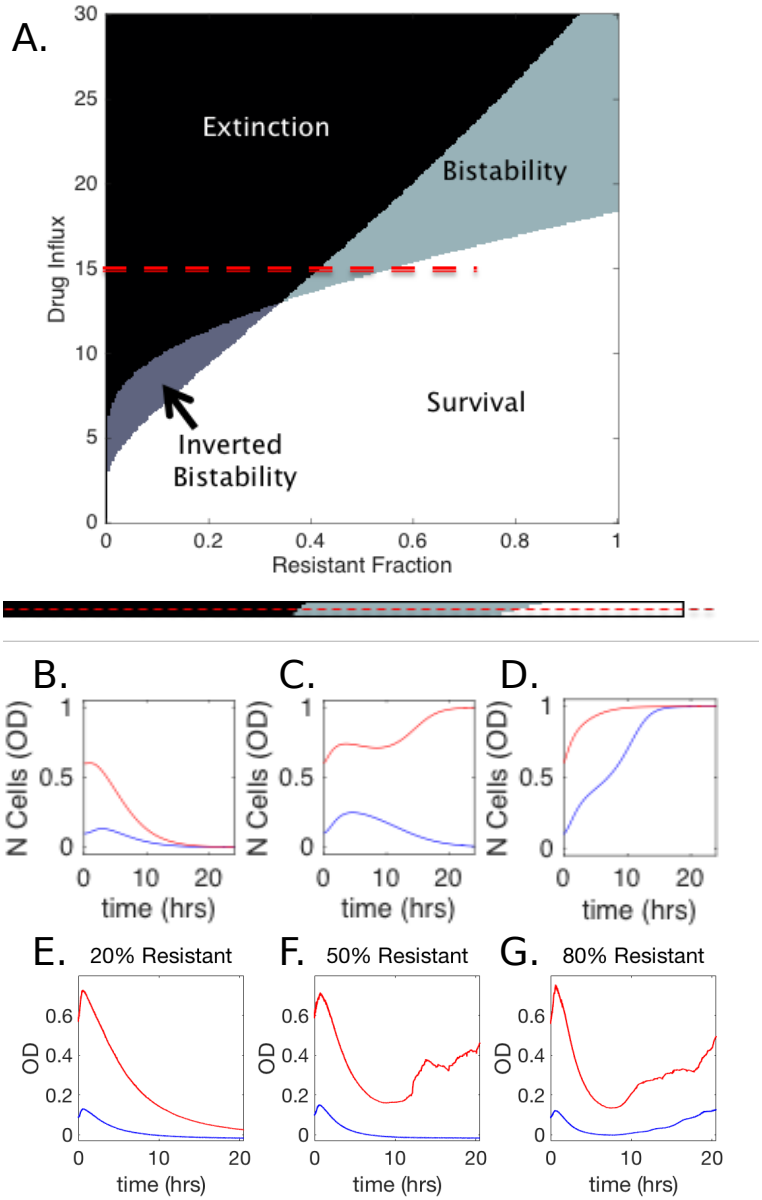

Figure 4.3: **Model and Experimental Bistability.** A. Theoretical Phase Diagram showing the different behaviors labeled by their different colors. Red dashed line shows theoretical cross section in phase space. B. Theoretical OD curves starting at high and low density, showing extinction. C. Theoretical OD curves starting at high and low density, showing bistability. D. Theoretical OD curves starting at high and low density, showing survival. E. Experimental OD curves of a 20% starting resistant fraction at starting OD 0.1 (blue) and OD 0.6 (red). Here both populations die. F. Experimental OD curves of a 50% starting resistant fraction at starting OD 0.1 (blue) and OD 0.6 (red). Here we see normal bistability between the two starting densities. G. Experimental OD curves of a 80% starting resistant fraction at starting OD 0.1 (blue) and OD 0.6 (red). Both populations survive.

mixed populations run in our chemostat at a specific drug concentration. We see below in Figure 4.4A the theoretical phase diagram as above, but now our focus is on the cross section and fractions with inverse bistability. Again we see theoretical representations of the different phases in Figure 4.4B,C,D from a cross section of the phase diagram. In Figure 4.4E,F,G, the different phases are experimentally shown, with extinction, inverse bistabilty, and survival all represented. These experiments were run overnight to determine the long scale dynamics.

4.2.5 Removing Inverse Bistability

After studying the inverse bistability, we wanted to observe the dynamics and collective behavior if the reverse inoculum effect was removed, ultimately removing the inverse bistabilty. As was found in the previous work in our lab, not only do the growing cells change the pH leading to an increase in drug efficacy, but this change can be negated by growing the cells in buffered media [3]. By removing this pH change, the system of two feedback loops should instead just become a single feedback from the resistant cells, leading to the loss of the inverse bistable phase. This was tested both theoretically by setting ϵ_1 in Equation 4.2 to 0 and experimentally by running the same experimental set up as before at the same initial population compositions, but now in buffered media. From simulations removing the inverse inoculum effect term, the phase diagram is altered as seen below in Figure 4.5A. Looking at a cross section in phase space with simulations, at the same drug influx as Figure 4.4, the cross section no longer has inverse bistability (Figure 4.5B,C,D). Experimental comparisons at the same drug concentration and same initial resistant fraction show inverse bistability in unbuffered media (Figure 4.5E) and normal bistability in buffered media (Figure 4.5F), indicating the absence of the reverse inoculum effect in buffered experiments.

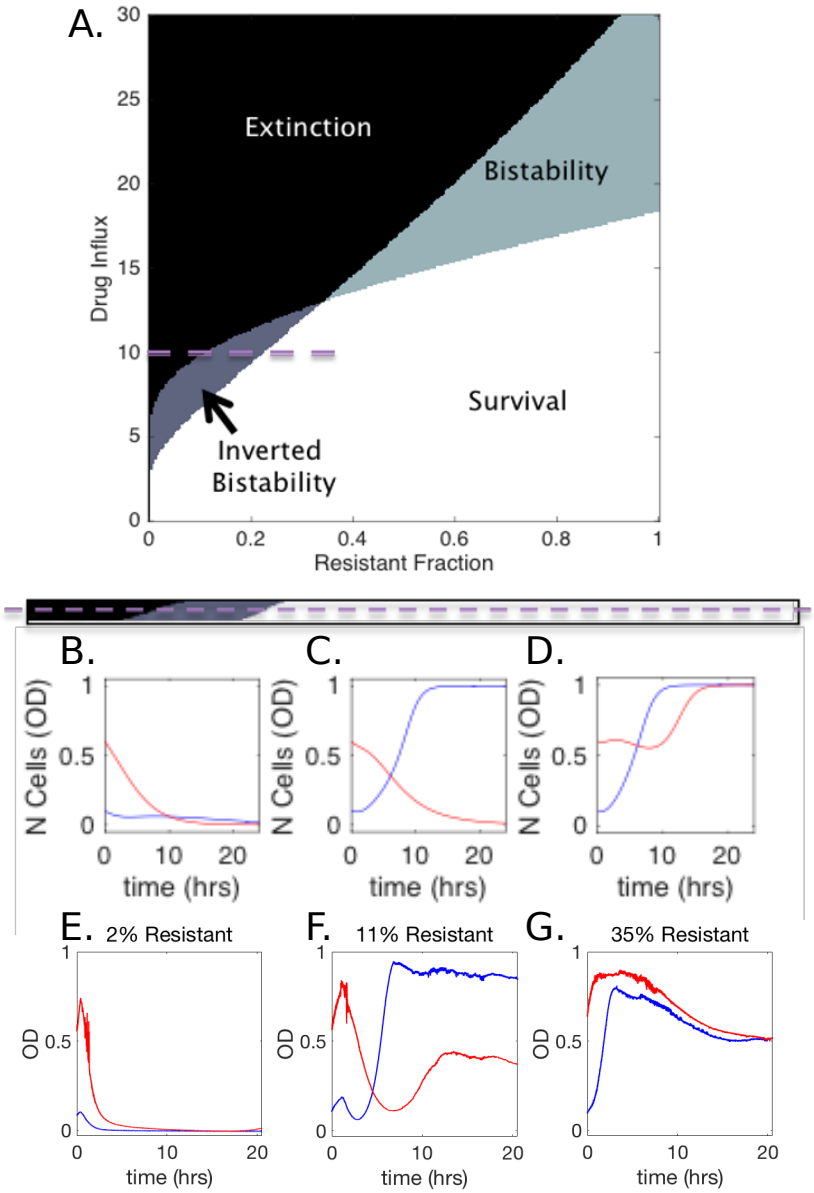

Figure 4.4: **Model and Experimental Inverse Bistability.** A. Theoretical Phase Diagram showing the different behaviors labeled by their different colors. Purple dashed line shows theoretical cross section in phase space. B. Theoretical OD curves starting at high and low density, showing extinction. C. Theoretical OD curves starting at high and low density, showing inverse bistability. D. Theoretical OD curves starting at high and low density, showing survival. E. Experimental OD curves of a 2% starting resistant fraction at starting OD 0.1 (blue) and OD 0.6 (red). Here both populations die. F. Experimental OD curves of a 11% starting resistant fraction at starting OD 0.1 (blue) and OD 0.6 (red). The high density population dies, while the low density survives, indicating inverse bistability. G. Experimental OD curves of a 35% starting resistant fraction at starting OD 0.1 (blue) and OD 0.6 (red). Both populations survive and go to an intermediate fixed point.

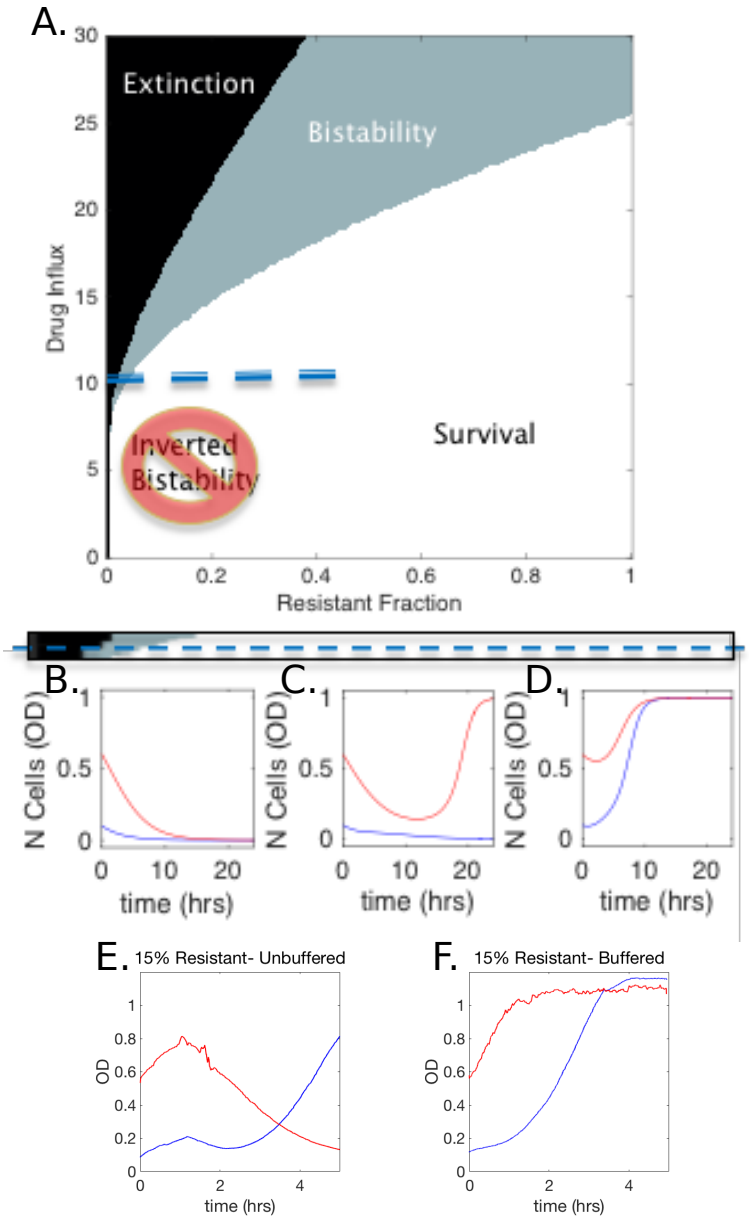

Figure 4.5: **Removing Inverse Bistability Theoretically and Experimentally with Buffered Media** A. Theoretical Phase Diagram showing the different behaviors labeled by their different colors. Blue dashed line shows theoretical cross section in phase space. This phase diagram no longer has inverse bistability due to the removal of the inverse inoculum effect. B. Theoretical OD curves starting at high and low density, showing extinction. C. Theoretical OD curves starting at high and low density, showing normal bistability, at a drug influx that previously showed inverse bistability in the unbuffered case (Figure 4.4C.). D. Theoretical OD curves starting at high and low density, showing survival. E. Experimental OD curves of a 15% starting resistant fraction at starting OD 0.1 (blue) and OD 0.6 (red), in unbuffered media, showing inverse bistability. F. Experimental OD curves of a 15% starting resistant fraction at starting OD 0.1 (blue) and OD 0.6 (red), in buffered media, showing normal bistability.

4.2.6 Selection for Resistant Cells Before Population Collapse

While we observe final populations surviving at high drug, we wanted to confirm these final populations are still a mixed population, see what effect the starting population composition has on the final population composition, and see what changes occur between experiments started at high and low densities. To study the composition, the resistant and sensitive cells were fluorescently labeled, similarly to the biofilms, with a plasmid containing BFP(res) and GFP(sens). Samples from each experimental vial were analyzed both before and after the experiment with FACS to analyze the population composition. Comparing the initial to final population composition allowed us to calculate the selection coefficient for each sample. Here we analyzed what the selection coefficient- a measure of how much faster one sub-population grows compared to the other sub-population- for resistant cells. To find the selection coefficient, we used both the change in the ratios of the population as well as the measurements of their ODs, shown below For each the sensitive and resistant cells, their growth was modeled logistically as

$$SC = \frac{\ln R_F/R_I}{\log(\frac{OD_F}{1+R_F}) - \log(\frac{OD_I}{1+R_I})} \tag{4.3}$$

where SC is the selection coefficient, R_F and R_I are the final and initial population ratios from FACS measurements, and OD_F and OD_I are the final and initial OD measurements from the chemostat. Using this equation, we calculated the selection coefficient for each fraction at each drug concentration as well as at high and low starting densities. A representative graph of selection coefficients is shown below in Figure 4.6 for the different population compositions at one drug concentration. For samples were the final population died, there is no selection coefficient, but in both the high and low OD cases it is clear the highest selection for resistant cells occurs at the interface between survival and extinction, showing a classic frequency dependent selection.

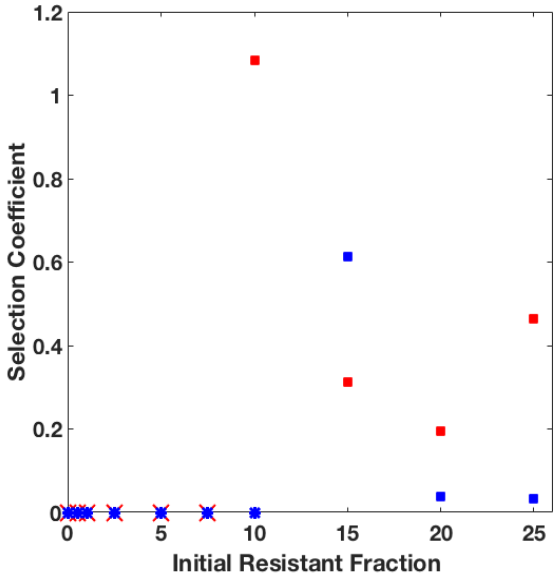

Figure 4.6: **Representative Selection Coefficient** Selection coefficients over the range of initial starting fractions for high density (red) and low density (blue) samples. If the final sample was dead, selection coefficient was set to 0. These samples are a representative graph for experiments run at a drug reservoir concentration of Ampicillin 100μg/ml. Selection coefficients were calculated using data from flow cytometry to determine final population composition as well as density data from the chemostat experiments (see Eq. 4.3) .

Not only do we see the interesting peak in selection coefficient, but the FACS data also allowed us to see the final total population. While we expected cooperation to occur, it was always possible that our resistant cells were able to survive in the drug while the sensitive cells died, leaving us with a final population of just resistant cells. From FACS, there was clear final mixed populations. Though the change in the initial to final fraction did vary widely, particularly increasing the resistant fraction at the lowest initial resistant fraction samples that lived, the final populations were still a mixture suggesting global cooperation between the resistant and sensitive cells.

4.2.7 Front Loaded Drug Dosing and Population Composition Effects

In addition to understanding how starting fraction could effect the phase of the samples, we were also interested in understanding the effects of drug dosing in samples

starting at the low density (high density samples were too close to stationary phase and did not show the drastic differences). Motivated by clinical treatments, where often an antibiotic is administered followed by a recovery time before the next dose, we wanted to mimic this type of front loaded dosing in our experimental set up. We continued to run experiments in our chemostat over a range of initial population compositions with the same drug dosing timing, but the antibiotic concentration of the reservoirs was increased for the front loaded dose for a set amount of time before being switched to reservoirs with no antibiotic. While the total drug administered stays constant over the experiment time, when the drug is administered is changed. In Figure 4.7 below, the final OD of two experiments is shown, one where each sample had a constant drug dose and another where the samples had a front loaded drug dose. In addition to comparing their final ODs (Figure 4.7A), we also show the OD curves over time overlaid for 3 different fractions (Figure 4.7B, C, D).

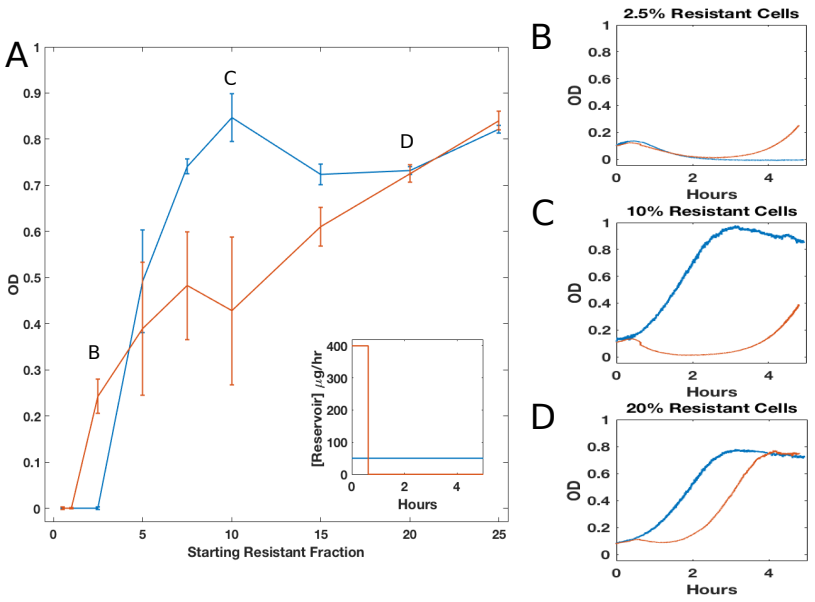

Figure 4.7: **Front loaded drug dosing final densities and growth show the interplay between the two density effects.** A. Final OD curves over a range of starting initial resistant fractions for standard dosing (blue curve) and front loaded drug dosing (red curve). B-D. Optical Density curves over experiment time for individual fractions. Blue curves are for the constant dosing experiments, red curves are for the front loaded dosing experiments. The density curves for the starting resistant fractions that appear in B-D are marked on figure A.

From the comparisons between the front loaded and constant doses we can see the interplay between the two different inoculum effects. For Figure 4.7B, the sample starts with only 2.5% resistant cells and this is a case where a very high front loaded dose ultimately is less effective at killing the population. Considering our two density effects and the population composition, Figure 4.7B shows a case where the reverse inoculum effect dominates as there are so few resistant cells present to contribute to a resistant inoculum effect. The reverse inoculum effect states that drug becomes more effective at higher densities, but here we dosed the samples up front, when they were still at a low density. Thus, the drug was not as effective as it had been in the sample that was constantly dosed at a lower concentration for the whole experiment time: a cartoon representation of this can be seen in Figure 4.8A. Conversely, Figure 4.7C shows a case where the resistant inoculum effect dominates. Here we have

a larger starting resistant population (10%), so the resistant effect dominates. But the resistant cells are more effective at a higher density, leading to a lower drug concentration. With front loaded dosing, the resistant cells are at a low starting density and are not as effective at breaking down drug as the constant drug dosing case: a cartoon of this can be seen in Figure 4.8B. At a high enough resistant fraction, there are enough resistant cells to overcome the drug and the two samples go to the same density regardless of dosing strategy (Figure 4.7D).

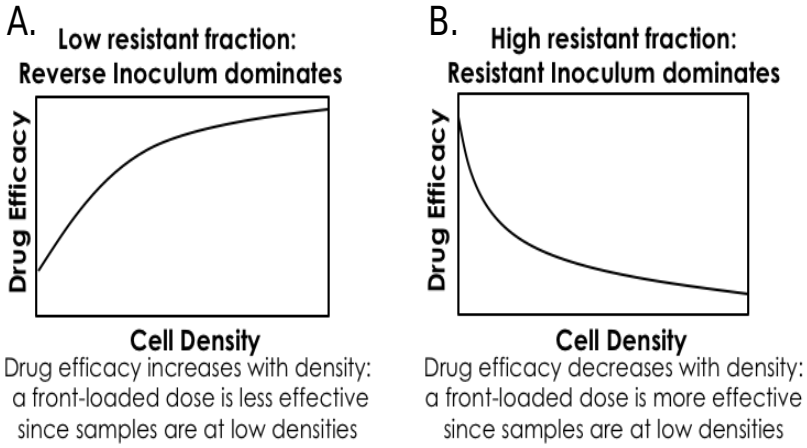

Figure 4.8: **Front Loaded Dosing: Different dominating effects cartoon** A. Explanation of the reverse inoculm effect dominating, the results of which are seen in Figure 4.7B. B. Explanation of the resistant inoculm effect dominating, the results of which are seen in Figure 4.7C

Different dosing strategies led to different final densities and we were further interested in determining the final population composition of the different experiments. Samples from the front loaded dosing experiments were taken to flow cytometry and the selection coefficient was measured and compared to that of the constant dosing experiments. While more of the front loaded dosing samples ultimately lived, Figure 4.9 shows this does not necessarily correspond to a higher selection coefficient for resistant cells. With constant dosing there is a clear peak with the highest selection occurring at the lowest resistant fraction that lives, whereas the front loaded dosing samples all select for more resistant cells but no one initial fraction stands out as

drastically as the constant dosing case.

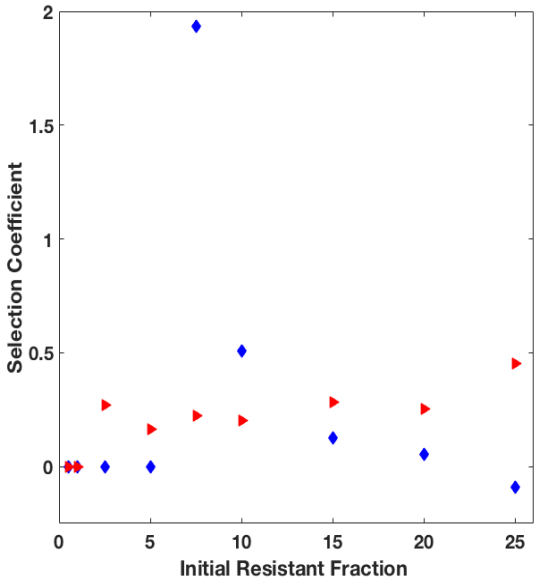

Figure 4.9: **Front Loaded and Constant Density Selection Coefficient** Selection coefficients for front loaded dosing samples (red) and constant dosing samples (blue). If the final sample was dead, selection coefficient was set to 0. While more fractions live in the front loading case, the selection coefficient does not vary widely across the different initial fractions, especially when compared to the constant dosing samples. The selection coefficient was calculated as mentioned above with Eq. 4.3

4.3 Discussion

Using the chemostat and mathematical modeling, we have shown how the different individual molecular mechanisms- drug degradation via β lactamase and pH changes from cell growth- can lead to interesting, sometimes counter intuitive, collective behavior. More than just seeing the different resistant inoculum effect and reverse inoculum effect in populations of either all resistant or all sensitive cells respectively, the experiments showed cooperation between the resistant and sensitive cells as well as interesting dynamics over time. The model phase diagram showing not only bistabilty but the region of inverse bistability indicates the complex interactions happening between the different inoculum effects and how those effects depend on the popula-

tion composition and drug dosing. To study predicted phases, we used chemostat experiments run over a range of starting population compositions and different drug concentrations to see experimental regions of bistability and inverse bistability. Using flow cytometry to measure population composition, we saw evidence for cooperation, as final populations were still mixed resistant and sensitive cells, and further analysis of the population change showed the trend of the selection coefficient and the tie between evolution and ecology. With the highest selection for resistant cells right at the boarder between population extinction and survival, this shows how ecology- the interactions between cells, like bistability and dynamics happening before mutations- has some effect on the selection coefficient which tells us about the evolution of the population composition and how strongly a particular phenotype is selected in a particular environment. Beyond studying the effects in a constant drug dosing regime, the front loaded drug dosing analysis allowed us to observe differences in final populations depending on the population composition and the dosing time. With larger resistant fractions, the populations counter intuitively grew less than populations with low resistant fractions when treated with a front loaded dose, due to the dominating resistant inoculum effect that is less effective at low densities. Similarly, populations with less resistant cells did better with a front loaded dose, due to the dominating reverse inoculum effect. Selection coefficient analysis of the final populations show a different trend of selection as well, as the front loaded doses do select for resistant cells, but there is no peak in the selection coefficient as seen in the constant dosing experiments.

Our experiments and model aim to study the two different density effects: the reverse inoculum effect and the resistant inoculum effect. As with our biofilm work, we acknowledge the complexity of the system and note we are using a simple math model specifically to explain these effects we can observe in our experimental work.

Experiments were also limited to 20-24 hour scans, as the reservoir bottles would need to be changed for continuing experiments, introducing possible contaminants. When observing our front loaded dosing experiments, we note we are motivated by clinical treatments, but we understand that clinical setting often have different dosing regimes and may utilize multiple different antibiotics or have more complex dosing regimes. We aimed to elucidate differences that can arise with different dosing strategies and demonstrate how a specific treatment may take advantage of one strategy of dosing over the other, depending on the initial population composition.

Our experimental studies have shown the dramatic temporal dynamics of mixed populations and the importance of the different density effects. These results suggest not only the importance of the specific molecular mechanisms, but the complex collective behavior that can arise from the interplay of different molecular mechanisms and density effects. With different dosing strategies, we can further elucidate how starting population composition can drastically alter population outcomes. These results have implications for clinical infections: if high doses are given initially instead of a constant, lower dose, the infectious population could actually thrive depending on the population composition. From our findings, further questions regarding other possible dosing strategies- which can be currently studied with our model- remain to be studied. With the rise of antibiotic resistant bacteria and the understanding the resistant and sensitive cells can coexist in planktonic populations, it is critical to understand how these populations may react to different treatments.

4.4 Methods

4.4.1 Bacterial Strains, Media, and Growth Conditions

Experiments were performed with OG1RF, a fully sequenced *E. faecalis* oral isolate. Resistant and sensitive cells were fluorescently labeled with the plasmid pBSU101. Resistant cells were labeled with BFP and additionally the plasmid carried the gene for the enzyme β Lactamase. Sensitive cells were labeled with the fluorescent color Dasher GFP. Cultures for experiments were made taking single colonies from BHI agar plates with selection antibiotics and incubated in sterile BHI (Remel) with appropriate selection antibiotic overnight at 37C. For any experiments requiring buffered media, standard BHI was prepared with the addition of Dibasic Sodium Phosphate (Fisher) to a concentration of 50 μM.

Continuous culture device experiments were run in our warm room at 30 C. Overnight cultures were seeded into experiment vials and once cells reached the desired initial density, experiments were run for 5 hours or overnight (20 hours).

4.4.2 Antibiotics

Antibiotics used in this study included Spectinomycin Sulfate (MP Biomedicals) and Ampicillin Sodium Salt (Fisher). Spectinomyicn was used in all media to ensure plasmid upkeep of the fluorescently labeled cells, while Ampicillin was the drug of interest in our experiments.

4.4.3 Continuous Culture Device

Experiments were performed in a custom built and computer controlled continuous culture device (CCD) as described in [3]. Briefly, bacterial populations are grown and monitored in glass vials. Voltage readings are taken every 1.5 seconds in each

vial using offset pairs of infrared emitter/detector LEDs, which the computer then converts into an optical density of the population in the vial. Additionally, each vial is attached to a system of peristaltic pumps that add drug and/or media and remove excess liquid on a schedule determined by the Drug Dosing Protocol for each specific experiment. Vials always contain 17 mls of sample (pump system holds volume constant).

4.4.4 Drug Dosing Protocols

In order to mimic "constant flow" of drug in our experiments, and based on the speed limitations of our pumping system, we elected to inject drug every 3.75 minutes for 7.5 seconds. Increasing or decreasing the "drug flow" then corresponds to an increase or decrease of the drug concentration that is injected, while holding the 7.5 seconds/3.75 minutes rate steady. Drugs are suspended in BHI media at specific concentrations, and held in reservoirs connected to the vials by the peristaltic pump system and tubing.

For experiments where the drug flow is not constant, we employ the above strategy for when drug is required. After the portion of the experiment when drug is used is over, we then disconnect the pumps from the vials and for 5 minutes flow through the tubing system fresh media without ampicillin (but still with spectinomycin for plasmid retention). This clears the pump system of ampicillin that had not yet reached the vials. We then reconnect the pumps to the vials and continue with the 7.5 seconds per 3.75 minutes flow schedule with the non-ampicillin media.

4.4.5 Experimental Mixtures and Set up

Given that we wanted to study the population dynamics of mixed resistant and sensitive populations, we started each of the vials of the CCD with different resis-

tant:sensitive fractions. Experimental mixtures were started at 0.1%, 0.5%, 1%, 2.5%, 5%, 7.5%, 10%, 15%, 20%, and 25% resistant population fraction. This was done by removing a portion of a Dasher GFP tagged sensitive population, and replacing the same amount from a resistant BFP-β Lacactamase population at the same optical density. For example, for the 25% resistant vials, 4.25 mLs of the population of sensitive cells was removed once the population reached the appropriate optical density. 4.25 mLs was then taken from a resistant population at the same optical density and put in the vial that the had the portion removed. Flow cytometry of populations at the beginning of experiments provides exact percentages for the resistant:sensitive fractions.

We were also interested in the effect of starting density on the survival of the different mixtures; experiments were started when initial populations had grown from inoculation to either an optical density of 0.1 or 0.6.

Once cells were mixed at the appropriate density, flow was started using reservoirs with BHI media at a given ampicillin concentration. For the constant flow dosing, experiments were run at ampicillin concentrations of 10, 25, 50, 100, 150 μg/ml. The front loaded drug dosing experiment used reservoirs at an ampicillin concentration of 400 μg/ml for 38 minutes followed by reservoirs with no ampicillin for 4 hours and 22 minutes.

4.4.6 Flow Cytometry

CCD samples were taken to the University of Michigan Flow Core and analyzed for composition based on fluorescent markers. Samples were taken from the mixed populations in the vials following the initial mixing as well as 5 hours later at the end of the experiment. Samples were run through a LSR Fortessa cell analyzer (BD

Biosciences). Control samples of single colors were also analyzed over time to verify plasmid retention as samples grew over experiment time. (Figure 4.10)

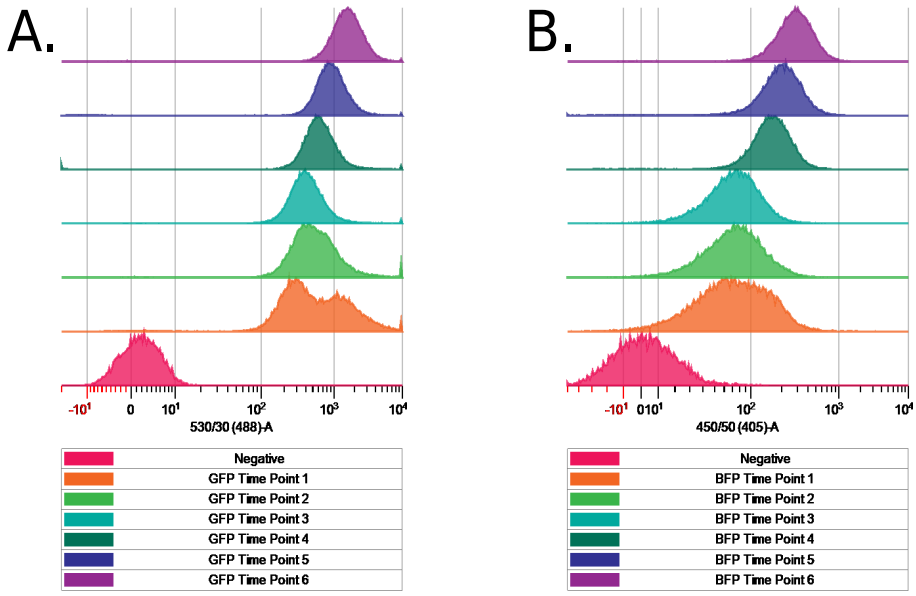

Figure 4.10: **Plasmid Retention from FACS experiments**A. Plasmid retention of Dasher GFP labeled cells. B. Plasmid retention of BFP labeled cells. Both samples were measured once every hour starting at time 0 until the experiment finished 5 hours later. Fluorescence was measured via FACS and compared to the negative control, showing not only the fluorescent labeling, but the retention of each color. The graph shows six fluorescent time points (purple-orange), with the last time point on top. The pink histogram is the negative control for comparison.

4.5 Bibliography

[1] K. I. Udekwu, N. Parrish, P. Ankomah, F. Baquero, and B. R. Levin. Functional relationship between bacterial cell density and the efficacy of antibiotics. *Journal of Antimicrobial Chemotherapy*, 63(4):745–757, Feb 2009.

[2] L. D. Sabath, C. Garner, C. Wilcox, and M. Finland. Effect of inoculum and of beta-lactamase on the anti-staphylococcal activity of thirteen penicillins and cephalosporins. *Antimicrobial Agents and Chemotherapy*, 8(3):344–349, Sep 1975.

[3] Jason Karslake, Jeff Maltas, Peter Brumm, and Kevin B. Wood. Population density modulates drug inhibition and gives rise to potential bistability

of treatment outcomes for bacterial infections. *PLOS Computational Biology*, 12(10):e1005098, Oct 2016.

[4] B E Murray. Beta-lactmase-producing enterococci. *Antimicrobial Agents and Chemotherapy*, 36(11):2355–2359, Nov 1992.

[5] B E Murray and B Mederski-Samaroj. Transferable beta-lactamase. a new mechanism for in vitro penicillin resistance in streptococcus faecalis. *Journal of Clinical Investigation*, 72(3):1168–1171, Sep 1983.

[6] Luo Yang, Kunjie Wang, Hong Li, John D. Denstedt, and Peter A. Cadieux. The influence of urinary ph on antibiotic efficacy against bacterial uropathogens. *Urology*, 84(3):731.e1–731.e7, Sep 2014.

[7] Christoph Ratzke and Jeff Gore. Modifying and reacting to the environmental ph can drive bacterial interactions. *PLOS Biology*, 16(3):e2004248, Mar 2018.

[8] Erdal Toprak, Adrian Veres, Sadik Yildiz, Juan M Pedraza, Remy Chait, Johan Paulsson, and Roy Kishony. Building a morbidostat: an automated continuous-culture device for studying bacterial drug resistance under dynamically sustained drug inhibition. *Nature Protocols*, 8(3):555–567, Feb 2013.

[9] James A. Damore and Jeff Gore. Understanding microbial cooperation. *Journal of Theoretical Biology*, 299:31 – 41, 2012. Evolution of Cooperation.

[10] S.-B. Hsu and Paul Waltman. A survey of mathematical models of competition with an inhibitor. *Mathematical Biosciences*, 187(1):53–91, Jan 2004.

[11] R. Craig MacLean, Ayari Fuentes-Hernandez, Duncan Greig, Laurence D. Hurst, and Ivana Gudelj. A mixture of "cheats" and "co-operators" can enable maximal group benefit. *PLoS Biology*, 8(9):e1000486, Sep 2010.

[12] Nicole M Vega and Jeff Gore. Collective antibiotic resistance: mechanisms and implications. *Current Opinion in Microbiology*, 21:28 – 34, 2014. Antimicrobials.

[13] Jeff Gore, Hyun Youk, and Alexander van Oudenaarden. Snowdrift game dynamics and facultative cheating in yeast. *Nature*, 459(7244):253–256, Apr 2009.

[14] Henry H. Lee, Michael N. Molla, Charles R. Cantor, and James J. Collins. Bacterial charity work leads to population-wide resistance. *Nature*, 467(7311):82–85, Sep 2010.

[15] Eugene A Yurtsev, Hui Xiao Chao, Manoshi S Datta, Tatiana Artemova, and Jeff Gore. Bacterial cheating drives the population dynamics of cooperative antibiotic resistance plasmids. *Molecular Systems Biology*, 9, Aug 2013.

[16] Robin A. Sorg, Leo Lin, G. Sander van Doorn, Moritz Sorg, Joshua Olson, Victor Nizet, and Jan-Willem Veening. Collective resistance in microbial communities by intracellular antibiotic deactivation. *PLOS Biology*, 14(12):e2000631, Dec 2016.

CHAPTER V

Fluorescent Reporter Library for Quantitative Population Dynamics in Enterococci

5.1 Introduction

To study the collective behavior of a mixed population, it is best to be able to distinguish between different sub populations. As such, it became apparent early in my work with *E. faecalis* the necessity of having a fluorescent library to use in labeling my strain. From single cell segmentation and population analysis with confocal microscopy (chapter 3) to cell counting with FACS and calculations of selection coefficients (chapter 4), all of these experiments needed fluorescently labeled cells. As noted in chapter 1, *E. faecalis* is a gram-positive pathogenic bacteria, commonly found in the gut microbiome[1], that has been implicated in a range of infections[2]. With interest in studying these infection bacteria, multiple different plasmids with different fluorescent markers have been developed and used with *E. faecalis*[3, 4, 5], but these all have a different vector backbone and thus a different selection antibiotic. In studies requiring multiple, differently labeled cell populations, selecting for the vector of one color could lead to killing of the population with another vector due to differing selection antibiotics.

With the multitude of different fluorescent proteins and expression vectors that exist for *E. faecalis*, there were many options to develop the fluorescent library. As such, multiple options of each blue, red, green, and yellow fluorescent sequences (at least two) were cloned into the vector backbone pBSU101, replacing the constituent eGFP with the fluorescent sequence of interest. The multiple options were necessary as *E. faecalis* has a low GC content[6, 7]; sequences high in GC, which often work well in common gram-negative bacteria, like *E. coli*, may have low expression in *E. faecalis*. In addition the sequence limitations, factors such as low oxygen levels and low pH [8] levels that may be necessary for the cells to grow can decrease the expression in the bacteria. As *E. faecalis* is a facultative anaerobe, the bacteria can grow in conditions not always conducive to high fluorescence. Furthermore, oligomerization of the proteins may lead to their inability to be transported in the cell and photobleaching from the imaging techniques greatly decrease the intensity of a fluorescent protein[9, 10], especially if the cell does not make many copies of the fluorescent protein. There have been efforts to address some of these problems, like oligimerization, and increase the number of fluorescent protein sequences available [11], but which sequences would produce the best fluorescence for specific experimental studies of *E. faecalis* remains unclear. In order to get the best possible expression both on the microscope and from the plate reader, multiple sequences coding for similar fluorescent colors were utilized.

Following cloning, extensive testing was done to determine which colors expressed the best in our strain. In addition to visualizing each color individually on a confocal microscope, mixtures of two or more colors were grown and imaged to verify the possibility of experiments involving multiple differently labeled strains or mutants. Further analysis observed the emission spectra of each color using a multimodal plate reader and mixtures of 2 colors were unmixed as a proof of concept to show the possibility of quantifying the sub-populations in multi-labeled populations.

5.2 Results

5.2.1 Creating the Fluorescent Library

Wanting to create a multitude of fluorescent plasmids that would express well in *E. faecalis* as well as all need the same selection antibiotic, I created a library conjugating the same plasmid backbone with multiple different fluorescent protein sequences. For the development of the library, 11 different plasmids were synthesized using pBSU101[4] as the plasmid backbone. The plasmid pBSU101 has the fluorescent protein eGFP originally as well as a spectinomycin resistance cassette, originally derived from the plasmid pAT28[12]. eGFP was replaced with 8 other fluorescent proteins, 2 optimized fluorescent proteins, and also recircularized without any color. The no color plasmid was used as a control to determine the intensity of the labeled cells. A schematic of the plasmid is shown below (Figure 5.1).

5.2.2 Color Spectra

To determine the fluorescent spectra of each color, as well as compare protein sequences coding for similar colors (ie Rudolph RFP and Fresno RFP, etc.), each individual color was scanned using a multimodal plate reader to obtain the spectra for that color. Overnight cultures of *E. faecalis*, each labeled with a different fluorescent plasmid, were diluted and plated in 96 well plates. The OD and fluorescence were measured as they grew in the plate reader (for excitation and emission wavelengths, see Methods). The graph for each color shows the spectra for that color, normalized to the cells with the no color plasmid.

During initial creation of the plasmids, it was unclear which fluorescent sequences would work best in *E. faecalis*: as such, multiple plasmids that should fluoresce the same color were created. From these spectra below in Figure 5.2, it is clear to see

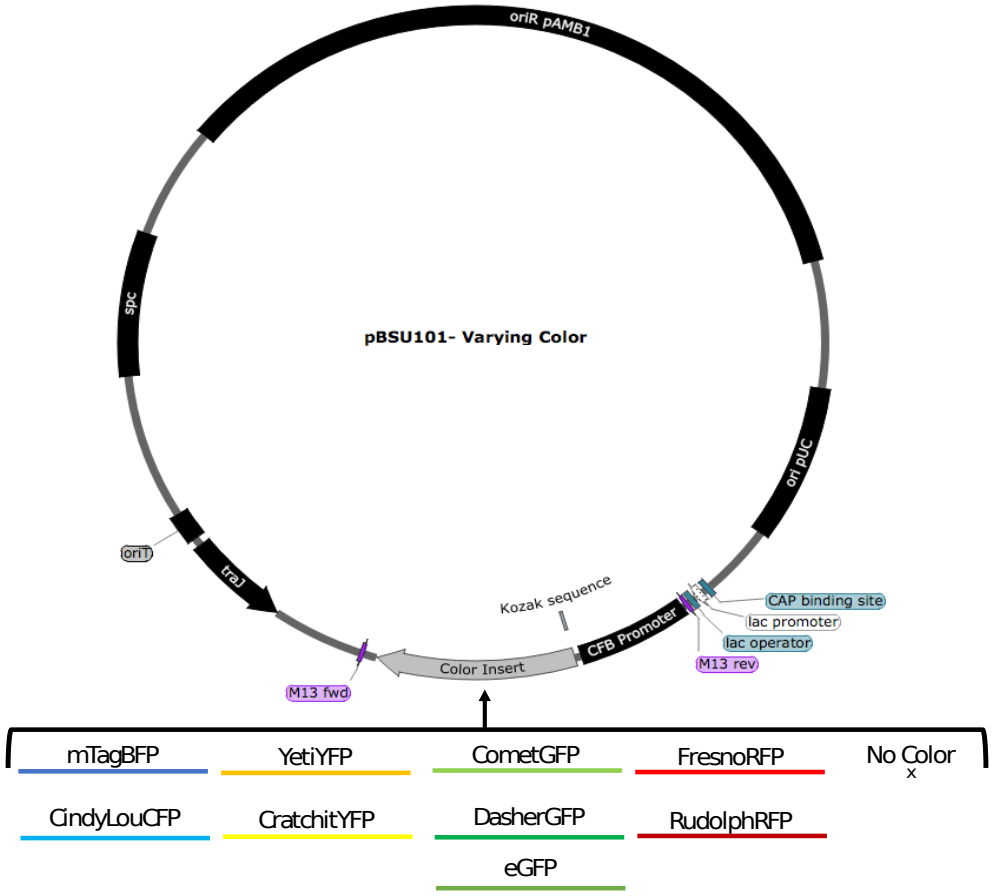

Figure 5.1: **Cartoon representation of the plasmid library created.** The library was created with the vector backbone of pBSU101, a plasmid with spectinomycin resistance and constitutively expressed eGFP behind a CAMP-factor gene (CFB) promoter. Using Gibson Assembly, the fluorescent eGFP sequence was replaced with 10 other color sequences. The plasmid was also recircularized with no color.

that some colors are more intense (ie Dasher GFP when compared to Comet GFP or eGFP) than others. In addition to seeing which colors were brightest and best, we also wanted to see which spectra overlapped, indicating mixtures of those colors would be harder to separate.

5.2.3 Optimized Colors

While having differently labeled fluorescent colors had succeeded, we wanted to optimized some of the colors to see if we could increase the intensity of the fluorescence.

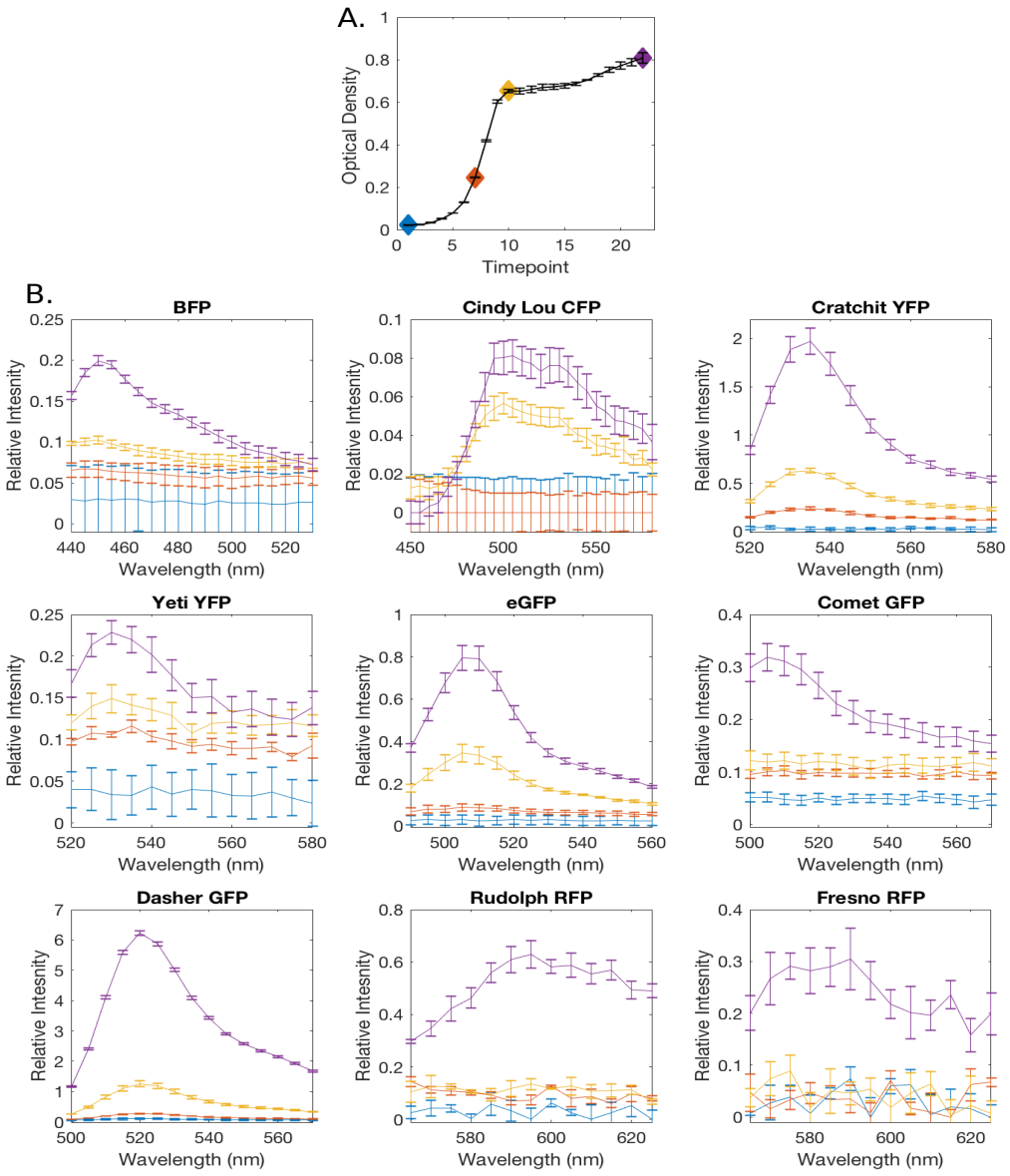

Figure 5.2: **Representative OD curve and the Fluorescent spectra of cells labeled with each color.** A. OD curve with markers showing the OD of each spectra. B. Color spectra. The color represented is shown in the title of the graph. The lines of each spectra show the fluorescence over OD: based on the corresponding time marked by that color on the OD curve as measured by a multimodal plate reader. The excitation and emission wavelengths used can be found in the Methods. The relative intensity is calculated by subtracting the WT intensity measurement at each color from that color intensity measurement, then dividing this subtracted intensity by the WT intensity.

We wanted to study mixtures of multiple colors and wanted the intensity of the different colors to be comparable. Using the spectra from each color (Figure 5.2), Dasher

GFP was found to be a very intense green, while none of the blue or re sequences appeared to give a intense color above background. With that in mind, BFP and Rudolph RFP were selected for optimization, and the sequence of each protein was altered to increase the GC content of the sequence with the goal of better expression after optimization: the sequence still coded for the same amino acids, but the codons used were ones more commonly seen in *E. faecalis*. Following cloning of the optimized sequences onto the pBSU101 backbone, the optimized plasmids transformed into our strain of interest, OG1RF. Using the plate reader, we again diluted overnight samples of the cells and tracked both the OD over time as well as the fluorescence spectra over time. Figure 5.3 below shows a comparison over time of BFP and Optimized BFP, as well as Rudolph RFP and Optimized Rudolph RFP. While the intensity at stationary phase (purple) does not seem largely different between the normal and optimized colors, it is clear, especially with the optimized BFP, that the optimized strain is more intense at lower ODs.

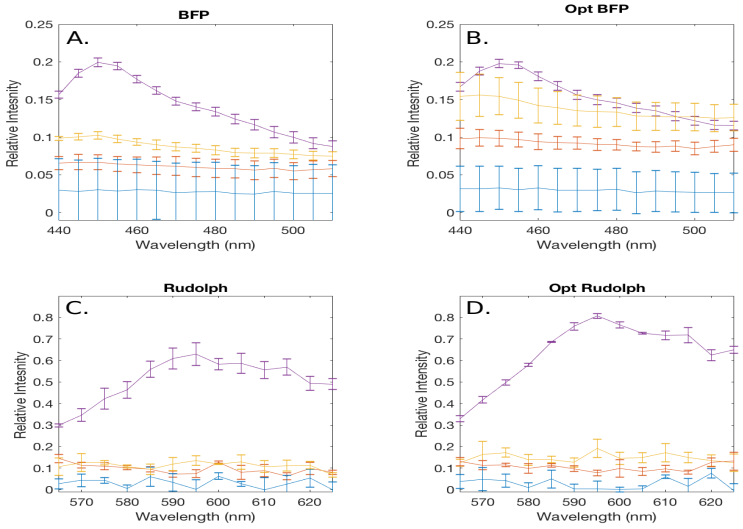

Figure 5.3: **Fluorescence spectra for non-optimized and optimized labeled strains** The fluorescent spectra of BFP (A), Optimized BFP (B), Rudolph RFP (C), and Optimized Rudolph RFP (D) measured on a multimodal platereader (for excitation and emission, see methods). The lines of each spectra show the fluorescence over OD: based on the corresponding time marked by that color on the OD curve as seen in fig 5.2A.

5.2.4 Unmixing Two Color Mixes

Wanting to test if we were able to unmix different 2 color mixes, representative mixtures of 2 colors were chosen by studying their color spectra in Figure 5.2. Looking at the spectra it was clear some colors, like the YFPs and GFPs, had very similar emission wavelengths and would not be easy to unmix, while other spectra were far enough apart to try unmixing. For the mixes chosen, triplicate mixes of 25:75, 50:50 and 75:25 were scanned at stationary phase using the multimodal plate reader (see Methods for excitation and emission). Controls of single colors were used to unmix the population and the triplicate unmixing results were averaged together. The results of a unmixing is shown below. While some mixes are clearly better suited for unmixing than others, most sets are within a reasonable range.

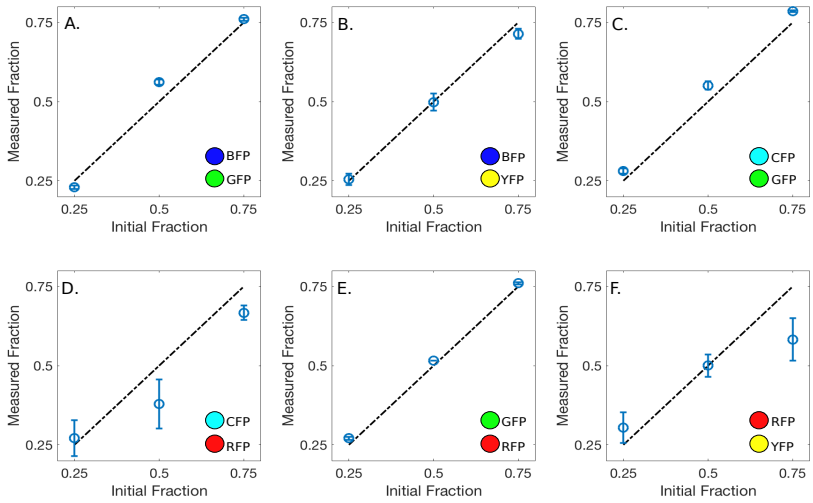

Figure 5.4: **Results from unmixing 2 color mixes at 25:75, 50:50, and 75:25.** The black dashed lines shows 1:1. A. BFP and Dasher GFP, B. BFP and Cratchit YFP, C. Cindy Lou CFP and Dasher GFP, D. Cindy Lou CPF and Rudolph RFP, E. Dasher GFP and Rudolph RFP, F. Rudolph RFP and Cratchit YFP. To create each mix, the appropriate amount of each indiviudal color was added in an eppendorf tube, vortexed, and then alliquoted into the 96 well plate. For each unmixing, three wells were unmixed as noted in the methods and averaged together, along with finding the SEM. Which two colors were unmixed are represented by the colored circles on the bottom right of each graph.

5.2.5 Microscopy

With many of our experiments looking to utilize confocal microscopy, we wanted to visualize the colors using our confocal microscope. Each sample contained cells labeled only one fluorescent color to verify the colors. Cells were grown overnight, diluted, and then plated on glass coverslips to image the fluorescence on a single cell level, Figure 5.5.

With the success of single cell images, we wanted to test the capabilities to image multiple colors at the same time as we are ultimately interested in imaging a mixed population. To test this, biofilms of either 50:50 mixes of two colors, or 33:33:33 mixes of three colors were grown overnight on a coverslip and imaged the next day using the same confocal microscopy protocols that were used to take the individual color images. Representative 2D slices from these biofilms are shown below in Figure 5.6. While these are not every color mixture possible, these were run as a proof of principle that we could distinguish between multiple colors at the same time.

Similarly to our plate reader experiments studying the differences between the optimized and non-optimized colors, we also wanted to observe and compare the optimized strains on the confocal to their non-optimized counterparts. Initial comparisons were made using diluted overnight samples: confocal images of each strain were taken using the exact same protocol and laser power and can be seen in Figure 5.7A-B (BFP) and D-E (Rudolph RFP). To study the intensity of the samples over time, images were also taken as the samples grew from an OD of about 0.05 to > 1.0. Overnight samples were diluted and imaged during growth to see if the intensity changes that can be seen during growth on the plate reader (Figure 5.3) could also be seen on the confocal. The intensity of each of these images were determined and comparisons between the intensity optimized and non-optimized were made at each time point.

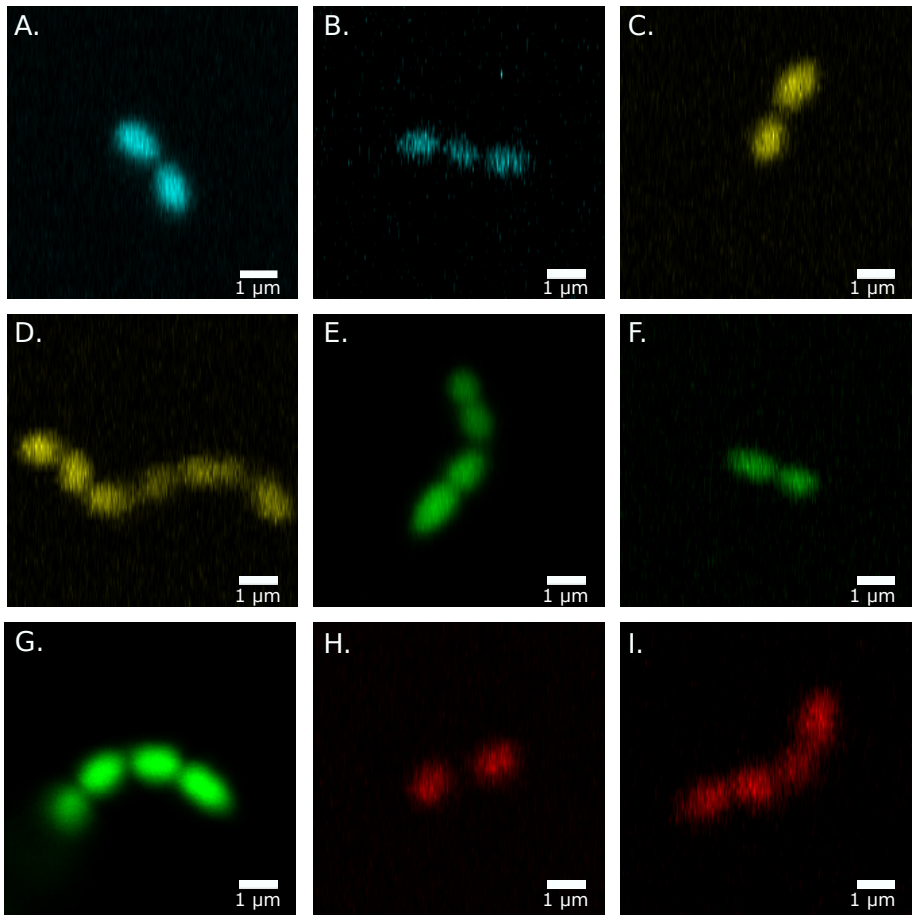

Figure 5.5: **Single cell images of cells labeled with each different fluorescent plasmid.** A. BFP, B. CindyLou CFP, C. Cratchit YFP, D. Yeti YFP, E. eGFP, F. Comet GFP, G. Dasher GFP, H. Rudolph RFP, I. Frenso RFP. Cells were grown overnight and diluted to allow clear imaging of single cells. Images were taken with our Zeiss confocal microscope with the excitation laser and emission spectra noted in the methods.

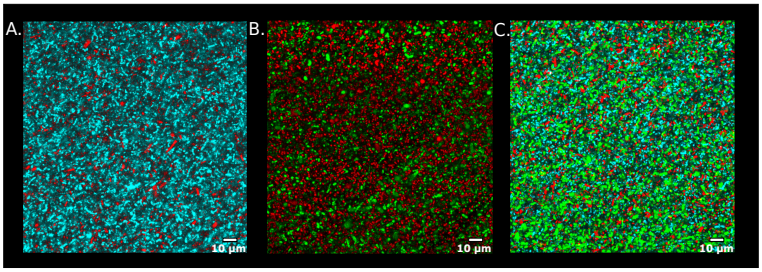

Figure 5.6: **Representative 3D Confocal Images of Mixed Biofilms** A. BFP/Rudolph RFP, B. Dasher GFP/Rudolph RFP, C. BFP/DasherGFP/Rudolph RFP. Mixed Biofilms were grown on coverslips overnight (24 hours) in a 6 well plate and then 2D stacks of images were taken and complied to give 3D final images.

From these intensity measurements, we can see a shift to the right in the peak of the intensity of cells at an intermediate time point in both the BFP to Optimized BFP case and the Rudolph RFP to Optimized Rudolph RFP case. The results are shown below in Figure 5.7.

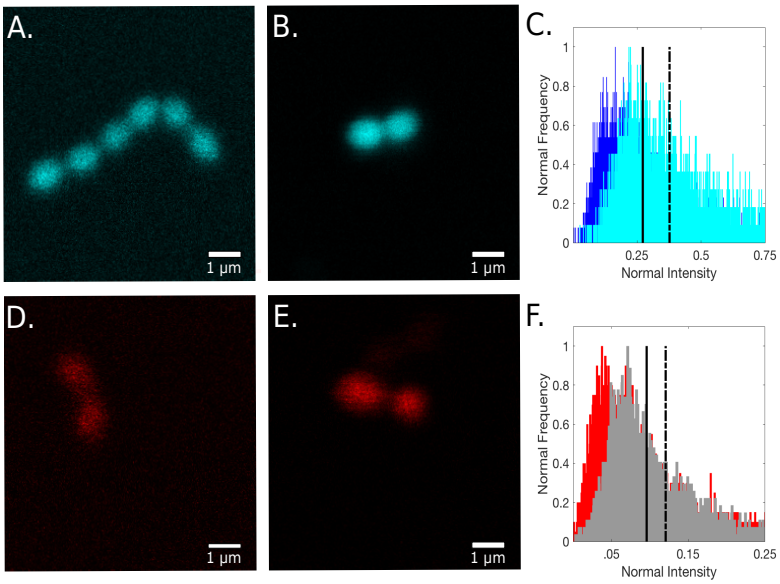

Figure 5.7: **Comparisons of cells labeled with Non-optimized and optimized strains** A. BFP B. Optimized BFP C. Frequency versus normalized intensity measurement of BFP (dark blue) and Optimized BFP (cyan) at an intermediate time point. D. Rudolph E. Optimized Rudolph F. Frequency versus normalized intensity measurement of Rudolph RFP (red) and Optimized Rudolph RFP (gray) at an intermediate time point. For both of the intensity graphs, the solid line shows the mean intensity of all pixels for the non-optimized color and the dashed line is the mean intensity of all pixels for the optimized color. Intensity measurements were calculated from confocal images of the cells during exponential growth.

5.3 Discussion

Fluorescence reporting to visualize cell populations has been a staple in the microbial experimental community for many years. However, some species have much more developed libraries than others, and we set out to create a library specifically for use with the low GC content, gram positive *E. faecalis*. We were not only able to develop a fluorescent reporter library, but were further able to show possible uses for the li-

brary, such as analyzing mixtures of cells with a multimodal plate reader or studying multi-labeled biofilms. With our optimized labeled strains, we were able to not only see the fluorescent spectra sooner during exponential growth in the plate reader but we also saw the intensity peak of the optimized strains shift to the right compared to the non-optimized strains during exponential growth on the confocal microscope. Using the backbone pBSU101 and replacing the eGFP with 8 other fluorescent sequences, 2 optimized fluorescent sequences, or recircularizing the plasmid without any fluorescent sequence, the library expresses well in *E. faecalis* and is intense enough to see both on a plate reader or with a confocal microscope.

Through optimizing two sequences of our library we observed an increase in the intensity of the fluorescence earlier in the growth of each optimized color when compared to the non-optimized one. We were still limited by the maximum intensity at stationary phase though, leading to complications in unmixing multiple colors. We were also limited as many of the colors have similar emissions, particularly the YFPs and GFPs, leading to our inability to unmix samples of just YFP and GFP.

Further experiments need to be done to determine if 3 color mixtures can be analyzed, but if the colors are chosen based on their spectra 3 color unmixing from a plate reader experiment may be possible. Future unmixing of multiple strains may also be possible using FACS, though those experiments were not done in this analysis. Depending on the requirements of the population to analyze or if the analysis needs to be done during stationary or exponential growth, the optimized sequences provide a more intense spectra sooner during growth and future unmixing could focus on exponentially growing samples of either two or three colors using the optimized colors instead of the non-optimized colors. With the development of both the 8 additional fluorescent colors to the library, the two optimized colors, and a recircularized no

color plasmid for controls, we have not only created a fluorescent library for use in *E. faecalis*, but further showed the capabilities and possible uses to study population compositions.

5.4 Methods

5.4.1 Bacterial Strains, Media, and Growth Conditions

Experiments and fluorescent characterization were performed in OG1RF, a fully sequenced *E. faecalis* oral isolate. Cultures for experiments were made taking single colonies from BHI (Remel) agar plates with selection antibiotics and incubated in sterile BHI with appropriate selection antibiotics overnight at 37°C.

5.4.2 Antibiotics

Spectinomycin Sulfate (MP Biomedicals) was the selection antibiotic used during all OG1RF fluorescent characterization and experiments. Kanamycin Sulfate (Fisher) was used to select prior to minipreps for plasmids which were used for their fluorescent sequences.

5.4.3 Cloning and Gibson Assembly

Starting with the plasmid pBSU101, a fluorescent plasmid designed for enterococci that uses the promoter cfb to drive fluorescence[4], Gibson Assembly was done to replace the existing color (eGFP) with eight other fluorescent proteins[13]. Fluorescent proteins were taken from existing plasmids that were miniprepped (Qiagen), linearized with enzymes (NEB), and underwent PCR to amplify the fluorescent sequence. Primers used for PCR and Gibson Assembly for the 8 standard fluorescent plasmids, as well as those for the pBSU101 backbone:these are the same for all optimized and non-optimized colors, are shown below in table 1 and 2. Table 3 shows

the primers used for PCR and GA of the optimized plasmids. Table 3 also has the primers for the recircularized, no color plasmid.

Name	**Sequence**	**Target**
pBSU 101-For	5'-AGC GGC CGC GAC TCT AGA G-3'	pBSU 101 backbone forward
pBSU 101-Rev	5'-GGT GGC GAC CGG TAC CCG-3'	pBSU 101 backbone reverse
BFP-pBSU 101 For	5'-CCC GGG TAC CGG TCG CCA CCA TGG TGT CTA AGG GCG AAG-3'	BFP and pBSU 101 overlap forward
BFP-pBSU 101 Rev	5'-ACT CTA GAG TCG CGG CCG CTA TTA AGC TTG TGC CCC AG-3'	BFP and pBSU 101 overlap reverse
CL CFP-pBSU 101 For	5'-CCC GGG TAC CGG TCG CCA CCA TGT CGT CTG GTG CCA AAT TG-3'	CFP and pBSU 101 overlap forward
CL CFP-pBSU 101 Rev	5'-ACT CTA GAG TCG CGG CCG CTT TAC TGA TAC GTG TCC AGA TCA AC-3'	CFP and pBSU 101 overlap reverse
Cratchit YFP-pBSU 101 For	5'-CCC GGG TAC CGG TCG CCA CCA TGA CGG CAT TGA CGG AAG-3'	YFP and pBSU 101 overlap forward
Cratchit YFP-pBSU 101 Rev	5'-ACT CTA GAG TCG CGG CCG CTT TAG CGA TAC GTC TCC AGG-3'	YFP and pBSU 101 overlap reverse
Yeti YFP-pBSU 101 For	5'-CCC GGG TAC CGG TCG CCA CCA TGA CGG CAT TGA CGG AAG-3'	YFP and pBSU 101 overlap forward
Yeti YFP-pBSU 101 Rev	5'-ACT CTA GAG TCG CGG CCG CTT TAG CGA TAC GTC TCC AGG-3'	YFP and pBSU 101 overlap reverse

Table 5.1: **Primers used for PCR and Gibson Assembly of the 8 different fluorescent library plasmids.** Cindy Lou CFP: CL CFP. Backbone primers for used for all the colors are listed here.

Colors used were Cindy Lou CFP, Yeti YFP, Cratchit YFP, Dasher GFP, Comet GFP,

Name	Sequence	Target
Comet GFP-pBSU 101 For	5'-CCC GGG TAC CGG TCG CCA CCA TGA CGG CAT TGA CGG AAG-3'	GFP and pBSU 101 overlap forward
Comet GFP-pBSU 101 Rev	5'-ACT CTA GAG TCG CGG CCG CTT TAA CGG TAA GTT TCC AGG TC-3'	GFP and pBSU 101 overlap reverse
Dasher GFP-pBSU 101 For	5'-CCC GGG TAC CGG TCG CCA CCA TGA CGG CAT TGA CGG AAG-3'	GFP and pBSU101 overlap forward
Dasher GFP-pBSU 101 Rev	5'-ACT CTA GAG TCG CGG CCG CTT TAC TGA TAC GTG TCC AGA TC-3'	GFP and pBSU 101 overlap reverse
Rud RFP-pBSU 101 For	5'-CCC GGG TAC CGG TCG CCA CCA TGT CCC TGT CGA AAC AAG-3'	RFP and pBSU 101 overlap forward
Rud RFP-pBSU 101 Rev	5'-ACT CTA GAG TCG CGG CCG CTT TAC GTT TCT TTA ACG TCG AC-3'	RFP and pBSU 101 overlap reverse
Fresno RFP-pBSU 101 Rev	5'-CCC GGG TAC CGG TCG CCA CCA TGA ATA GCC TGA TTA AAG AGA ATA TG-3'	RFP and pBSU 101 overlap forward
Fresno RFP-pBSU 101 Rev	5'-ACT CTA GAG TCG CGG CCG CTT TTG TAC AGT TCG TCC ATA C-3'	RFP and pBSU 101 overlap reverse

Table 5.2: **Primers used for PCR and Gibson Assembly of the 8 different fluorescent library plasmids, continued.** Rudolph RFP: Rud RFP.

Rudolph RFP, and Fresno RFP taken from the Protein Paintbox plasmids (ATUM, [14, 15]). BFP was taken from the plasmid mTag-BFP2 (Addgene, [16]). BFP and Rudolph RFP were codon optimized for expression in *E. faecalis*. Optimization of BFP was done with Geneart (Fisher) and optimization of Rudolph RFP was done with AUTM. In addition to replacing the color, pBSU101 was also recircularized without any color but the same spectinomycin resistance marker.

Following Gibson Assembly of the different plasmids, the plasmids were originally transformed into the high efficiency *E. coli* cloning strain C2987 (NEB) via heat shock transformations[17]. Following successful transformations, plasmids were miniprepped from the C2987, sequence verified, and transformed into the *E. faecalis* strain OG1RF, with electorporation before characterization[18].

5.4.4 Plate Reader Experiments

Color spectra were measured using an Enspire multimodal plate reader. Overnights of cells with each color, as well as cells with the no color plasmid, were diluted to an optical density (OD) of 0.01. Each color was run in triplicate with the emission spectrum and OD measured every 45 minutes until the cells reached stationary state. The excitation and emission used for each color are shown below in the table. Following the scan, results were normalized to the no-color cells and the spectra were plotted.

5.4.5 Mixture Analysis and Unmixing

Mixtures of 2 color stationary state fluorescently labeled cells were scanned on the plate reader using the same excitation as table 1. For emission, 6 wavelengths capturing the peak of each color (found using the entire spectra data) were used to unmix. The exact wavelengths used are shown in table 4. The samples were created after

Name	Sequence	Target
Opt BFP-pBSU 101 For	5'-CCC GGG TAC CGG TCG CCA CCA TGG TTT CAA AAG GTG AAG-3'	Opt BFP and pBSU 101 overlap forward
Opt BFP-pBSU 101 Rev	5'-ACT CTA GAG TCG CGG CCG CTG TTT AAT TTG TGA CCT AAT TTT G-3'	Opt BFP and pBSU 101 overlap reverse
Opt Rudolph RFP-pBSU 101 For	5'-CCC GGG TAC CGG TCG CCA CCA TGT CAT TAT CAA AAC AAG TTT TAC-3'	RFP and pBSU 101 overlap forward
Opt Rudolph RFP-pBSU 101 Rev	5'-ACT CTA GAG TCG CGG CCG CTT TAT GTT TCT TTA ACA TCA ACT G-3'	RFP and pBSU 101 overlap reverse
pBSU 101-Section1 For	5'-CGG AGC CTA TGG AAA AAC GCC AGC AAC GCG GCC TTT TTA CG-3'	Overlap: section 1 and section 2 forward
pBSU 101-Section1 Rev	5'-ACT CTA GAG TCG CGG CCG CTG GTG GCG ACC GGT GGT ACC CG-3'	Overlap: section 1 and section 2 reverse
pBSU 101-Section2 For	5'-AGC GGC CGC GAC TCT AGA-3'	pBSU 101 section 2 forward
pBSU 101-Section2 Rev	5'-GCG TTT TTC CAT AGG CTC-3'	pBSU 101 section 2 reverse

Table 5.3: **Primers used for PCR and Gibson Assembly of the optimized and no color plasmids.** For the no color plasmid, the backbone was PCR in two separate pieces and Gibson Assembled back together.

Color	Excitation (nm)	Emission (nm)
BFP	401	440-530
CindyLou CFP	400	450-580
Yeti YFP	500	520-580
Cratchit YFP	500	520-580
Comet GFP	480	500-570
Dasher GFP	480	500-570
eGFP	470	490-560
Rudolph RFP	545	565-625
Fresno RFP	545	565-625

Table 5.4: **Excitation and Emissions used for the plate reader full spectra.** Due to limitations of the plate reader, excitation and emission wavelengths must be at least 20 nm apart. We found these protocols to capture the peak of most spectra.

diluting the stationary state cells to the same OD and mixed at known ratios.

Using Matlab, intensity of each fluorescent channel was used to fit the equation, using a least-squares fitting approach[19]:

$$M = \sum_{i=1}^{N} c_i * m_i \tag{5.1}$$

where M is the measured intensity matrix from the mixtures, there are N total colors in the mixture, m_i is the intensity matrix for color i and c_i is the constant representing how much of color i is in the total mixture. The c_i's add to 1.

Color	Excitation (nm)	Emission (nm)
BFP	401	440-595
CindyLou CFP	400	495-520
Cratchit YFP	500	525-550
Dasher GFP	480	510-535
Rudolph RFP	545	585-610

Table 5.5: **Excitation and Emissions used for the plate reader unmixing experiments.** Due to limitations of the plate reader, excitation and emission wavelengths must be at least 20 nm apart. Emissions wavelengths were scanned every 5 nm, giving us a total of 6 wavelengths around the peak of each color.

5.4.6 Confocal Microscopy

Samples for confocal imaging were grown overnight, diluted 1:5 in fresh BHI media with spectinomycin, and grown for 30 minutes before imaging with a LSM 700 confocal microscope (Zeiss), 40x oil objective. The confocal setup has four different excitation lasers. Table 2 below shows the different excitation laser used as well as the color spectra protocol used for emission.

Color	Excitation Laser	Laser Power	Emission Spectra
BFP	405 nm	5.0	mBFP
CindyLou CFP	405 nm	5.0	mBFP
Yeti YFP	488 nm	1.0	Lucifer Yellow
Cratchit YFP	488 nm	1.0	Lucifer Yellow
Comet GFP	405 nm	5.0	eGFP
Dasher GFP	488 nm	0.5	eGFP
eGFP	488 nm	0.5	eGFP
Rudolph RFP	555 nm	5.0	mStrawberry
Fresno RFP	555 nm	5.0	mStrawberry

Table 5.6: **Excitation laser and emission spectra used for the confocal experiments.** The Zeiss software comes loaded with preset emission spectra and the closest ones to the estimated emission spectra for each fluorescent plasmid were used.

Mixed biofilms of 2 or 3 colors were also grown to show the possibility of imaging multiple colors at the same time. Overnights of each color were diluted 1:100 then mixed in ratios of 50:50 (for 2 color biofilms) or 33:33:33 (for 3 color biofilms). The mixtures were grown in 6 well plates overnight, removed after 24 hours, and the biofilm imaged using z-stack protocol of the confocal microscope.

To compare optimized color fluorescent intensity to the standard color fluorescent intensity, we measured fluorescence throughout the growth process. Overnight cultures were diluted 1:100 in fresh BHI with spectinomycin, grown for 1.5 hours, and then samples imaged every hour for 15 hours. Boundaries of each cell were selected from each image using imageJ. The pixel intensity within each cell boundary was

measured in Matlab to determine intensity per cell at the different growth stages. Pixel intensities are represented as 16-bit integers. We normalize their intensities to a maximum value of 50,000. Frequencies are normalized to the highest frequency of pixel intensity values within the range of 0 to 50,000. Normalization of the frequencies was done for optimized and non-optimized distributions independently. In addition to generating histograms for the range of intensities, we also averaged each set of pixel intensities to obtain the mean intensity for each optimized and non-optimized distributions.

5.5 Bibliography

[1] Gerald W. Tannock and Greg Cook. Enterococci as members of the intestinal microflora of humans. *The Enterococci*, pages 101–132.

[2] Preeti . Malani, Carol A. Kauffman, and Marcus J. Zervos. Enterococcal disease, epidemiology, and treatment. *The Enterococci*, pages 385–408.

[3] Concepción Nieto and Manuel Espinosa. Construction of the mobilizable plasmid pmv158gfp, a derivative of pmv158 that carries the gene encoding the green fluorescent protein. *Plasmid*, 49(3):281 – 285, 2003.

[4] Simone Aymanns, Stefanie Mauerer, Ger van Zandbergen, Christiane Wolz, and Barbara Spellerberg. High-level fluorescence labeling of gram-positive pathogens. *PLoS ONE*, 6(6):e19822, Jun 2011.

[5] Tomás García-Cayuela, Luz P. Gómez de Cadiñanos, M. Luz Mohedano, Pilar Fernández de Palencia, Daniel Boden, Jerry Wells, Carmen Peláez, Paloma López, and Teresa Requena. Fluorescent protein vectors for promoter analysis in lactic acid bacteria and escherichia coli. *Applied Microbiology and Biotechnology*, 96(1):171–181, Apr 2012.

[6] A. Aakra, O. L. Nyquist, L. Snipen, T. S. Reiersen, and I. F. Nes. Survey of genomic diversity among enterococcus faecalis strains by microarray-based comparative genomic hybridization. *Applied and Environmental Microbiology*, 73(7):2207–2217, Jan 2007.

[7] Roy H. Stevens, Mahmoud R. Ektefaie, and Derrick E. Fouts. The annotated complete dna sequence of enterococcus faecalis bacteriophage ef11 and its comparison with all available phage and predicted prophage genomes. *FEMS Microbiology Letters*, 317(1):9–26, Jan 2011.

[8] Andrew B. Cubitt, Roger Heim, Stephen R. Adams, Aileen E. Boyd, Larry A. Gross, and Roger Y. Tsien. Understanding, improving and using green fluorescent proteins. *Trends in Biochemical Sciences*, 20(11):448 – 455, 1995.

[9] Jorg Wiedenmann, Franz Oswald, and Gerd Ulrich Nienhaus. Fluorescent proteins for live cell imaging: Opportunities, limitations, and challenges. *IUMBM life*, 61(11):10–29–1042, 2009.

[10] George H Patterson. A new harvest of fluorescent proteins. *Nature Biotechnology*, 22(12):1524–1525, Dec 2004.

[11] Nathan C Shaner, Robert E Campbell, Paul A Steinbach, Ben N G Giepmans, Amy E Palmer, and Roger Y Tsien. Improved monomeric red, orange and yellow fluorescent proteins derived from discosoma sp. red fluorescent protein. *Nature Biotechnology*, 22(12):1567–1572, Nov 2004.

[12] Patrick Trieu-Cuot, Cécile Carlier, Claire Poyart-Salmeron, and Patrice Courvalin. A pair of mobilizable shuttle vectors conferring resistance to spectinomycin for molecular cloning inescherichia coliand in gram-positive bacteria. *Nucleic Acids Research*, 18(14):4296–4296, 1990.

[13] Daniel G Gibson, Lei Young, Ray-Yuan Chuang, J Craig Venter, Clyde A Hutchison, and Hamilton O Smith. Enzymatic assembly of dna molecules up to several hundred kilobases. *Nature Methods*, 6(5):343–345, Apr 2009.

[14] Monika González, Itziar Martín-Ruíz, Silvia Jiménez, Lucia Pirone, Rosa Barrio, and James D. Sutherland. Generation of stable drosophila cell lines using multicistronic vectors. *Scientific Reports*, 1(1), Aug 2011.

[15] Dmitry A. Shagin, Ekaterina V. Barsova, Yurii G. Yanushevich, Arkady F. Fradkov, Konstantin A. Lukyanov, Yulii A. Labas, Tatiana N. Semenova, Juan A. Ugalde, Ann Meyers, Jose M. Nunez, and et al. Gfp-like proteins as ubiquitous metazoan superfamily: Evolution of functional features and structural complexity. *Molecular Biology and Evolution*, 21(5):841–850, May 2004.

[16] Oksana M. Subach, Paula J. Cranfill, Michael W. Davidson, and Vladislav V. Verkhusha. An enhanced monomeric blue fluorescent protein with the high chemical stability of the chromophore. *PLoS ONE*, 6(12):e28674, Dec 2011.

[17] Hiroaki Inoue, Hiroshi Nojima, and Hiroto Okayama. High efficiency transformation of escherichia coli with plasmids. *Gene*, 96(1):23 – 28, 1990.

[18] Bruce M. Chassy, Annick Mercenier, and Jeannette Flickinger. Transformation of bacteria by electroporation. *Trends in Biotechnology*, 6(12):303 – 309, 1988.

[19] Derek York. Least-squares fitting of a straight line. *Canadian Journal of Physics*, 44(5):1079–1086, May 1966.

CHAPTER VI

Conclusions

My research has shown the interesting, emergent properties that can arise in bacterial communities. Drawing on understanding of the specific molecular mechanisms that are important to an individual cell's response to an environment- like an antibiotic present- my work has focused on studying the effects of these small mechanisms on a larger length scale, in communities of cells either in surface attached biofilms or planktonic cultures. I have worked to bring together models and simulations with experimental wet lab studies to not only observe the interesting behaviors, but also try to develop a set of rules and parameters that describe the behavior.

To begin studying these types of emergent behaviors, all sensitive biofilms at sub-inhibitory concentrations of antibiotics were studied. While biofilms could be more complex- like many species biofilms or biofilms dosed with many drugs- studying these simple biofilms at low antibiotic concentrations led to interesting peak behavior in biofilm mass, but this behavior only occurred when cell wall synthesis inhibitors were used. Further study tied this peak behavior to an increase in cell lysis and extracellular DNA (eDNA). From previous work studying *E. faecalis* biofilms grown without any antibiotic present, eDNA was noted to be a critical component of biofilm formation and growth. Using antibiotics that were known to disrupt the cell wall,

the eDNA present in the biofilm increased and planktonic cells were able to take advantage of this eDNA and attach to the biofilm, driving up the total cell mass of the biofilms. However, this behavior was seen as a peak, indicating the trade off between cells lysis and releasing eDNA while also killing the planktonic cells that need to be present to take advantage of the eDNA. These molecular effects were not only seen experimentally but modeled as well. The model created testable predictions that experiments were able to verify, studying the effect of different lysis inhibitors to shift the peak to higher drug concentrations or DNAse to break down the beneficial eDNA and decrease the peak. The trade offs between beneficial lysis and cell death lead to interesting counter intuitive behaviors that I wanted to continue studying in biofilm systems.

Moving beyond the sub-inhibitory antibiotic regime, the biofilm composition becomes more important to the final outcome. Using mixed populations of fluorescently labeled sensitive and resistant cells, where resistant cells produce an enzyme that breaks down the antibiotic, I grew biofilms of varying compositions both with and without antibiotic present. Using confocal microscopy, I analyzed both the total biofilm mass as well as the final compositions of the biofilms and the spatial arrangement of the cells. The presence of the molecular resistance mechanism leads to cooperation on a single cell level. Not only does the final composition still contain sensitive cells, but spatial analysis shows the organization of sensitive cells close to resistant cells in the presence of drug. Similar to the previous biofilm work, I also developed a stochastic agent based model to mimic biofilm growth and spatial organization. The sensitive cells in the model experienced a cooperative effect when their local neighborhoods were enriched for sensitive cells, and introducing this coupling into the model led to very similar organizations between the model and experimental results.

Using the same bacterial mixtures but studying the population planktonically instead of in biofilms, the spatial component is no longer relevant, now replaced by density effects. In this mixed population, there were two different density effects of interest, the reverse and resistant inoculum effect. The reverse inoculum effect is caused by the pH change cell populations undergo as they grow. This decrease in the pH ultimately increases the effectiveness of the drug ampicillin, the antibiotic of interest in this study. For the resistant inoculum effect, the presence of resistant cells in the population introduce the enzyme beta lactamase into the system, an enzyme that can degrade ampicillin and decrease the drug effectiveness. With these two mechanisms at play, our system is defined by the feedback between the two effects; feedback that is dependent on the composition and density of the system. Again, I created a model accounting for these two different effects and studied the different phases in the simulation to help guide the experimental studies. Using a chemostat bioreactor to monitor the population growth as well as specifically administer antibiotics to the populations, we measured regions of both bistability and inverse bistability and showed them to be dependent not only on the initial population composition and density but also the antibiotic concentration. Flow cytometry analysis showed the cooperation in the population, as the final compositions still contained sensitive cells, though often changed from their initial compositions- and the change was quantified by a selection coefficient. Front-loaded dosing experiments further explore this complex phase space, showing the effects of both population density and composition. The two different density effects caused by the molecular mechanisms leads to complex, collective behavior.

To study these different collective behaviors, I also developed and optimized a fluorescent reporter library for *E. faecalis*. As a necessity to distinguish between the resistant and sensitive cells in analysis of biofilms and planktonic cultures, I used

Gibson Assembly to develop the different fluorescent plasmids on the same vector, ensuring that the selection antibiotic for the fluorescence was constant between the different colors and allowing the growth of multi-color cultures. Further analysis led to optimizing two of the colors as well as testing mixtures of multiple colors to unmix the population composition. The creation of the library provided the ability to analyze mixed biofilms and planktonic cultures and evaluate their collective behaviors.

While our experimental work allows us to quantify the different behaviors we observe, there are limitations due to being in a controlled lab environment. *E. faecalis* may appear in complex communities in nature that have other outstanding factors that effect their final outcome. In clinical settings, the treatments often must be done quickly and finding the optimal dosing strategy may not be practical on the time scale. But future work extending on the findings here can begin to address those concerns. Complex communities of multiple species can be studied in the lab environment, and in vivo model systems such as mice or rats could be used to gain more clinical focused insight. By taking the same quantitative approach we currently use in the lab and expanding the systems we use, we can begin to answer some of the big questions facing antibiotic resistance and bacterial populations.

Collective behavior emerges from smaller scale interactions and often leads to interesting, unexpected population level outcomes. Looking into evolution, we find many cases where a microscopic effect can have macroscopic consequences, and this trend continues in the previous studies. In the work presented, not only is a community, collective behavior seen- a peak in biofilm mass at low drug, spatially organized mixed biofilms at high drug, or inverse and normal bistability in planktonic cultures- but all of the behaviors can be tied to specific molecular mechanisms- presence of eDNA, spatial cooperation from enzymatic drug degradation, or competing inoculum effects.

Motivated by previous works suggesting cooperation occurs in bacterial systems, my work has extended the understanding of cooperation and how it appears- either in the eDNA present due to other cells dying and local neighborhoods on a single cell level in spatially fixed biofilms or globally as part of density effects in well-stirred planktonic cultures. Collective behavior can drastically alter bacteria population outcomes and learning and understanding these effects, as well as the smaller scale mechanisms that cause them, is an important next step in advancing our understanding of bacterial community dynamics.